AD-A110 098   AIR FORCE INST OF TECH WRIGHT-PATTERSON AFB OH   F/G 3/1
                NUMERICAL STUDIES OF GRAVITATIONAL ACCRETION FROM X-RAY HEATED --ETC(U)
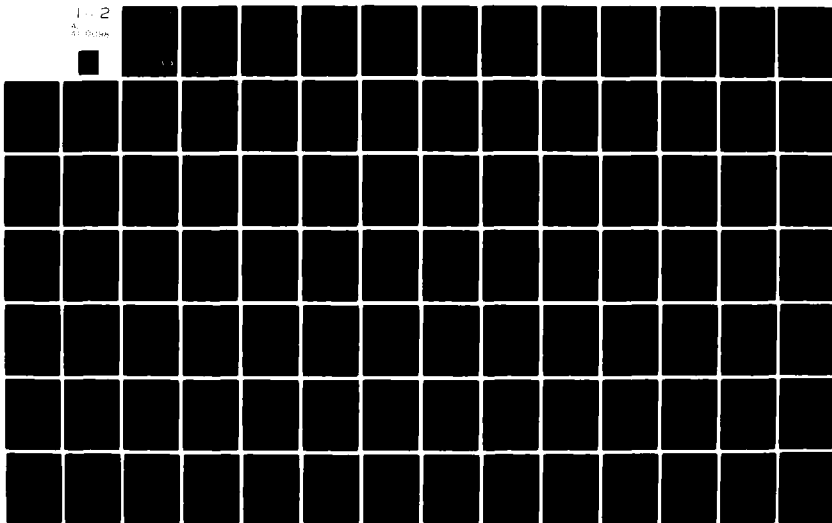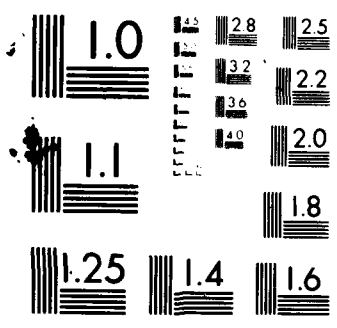   DEC 81 J A LUPO
UNCLASSIFIED   AFIT/CI-81-67D   NL

1.0	2.8	2.5
1.1	3.2	2.2
	3.6	
	4.0	2.0
		1.8
1.25	1.4	1.6

MICROCOPY RESOLUTION TEST CHART
NATIONAL BUREAU OF STANDARDS 1963 A

81-67D

①

NUMERICAL STUDIES OF GRAVITATIONAL ACCRETION

FROM X-RAY HEATED STELLAR WINDS

AD A110098

BY

JAMES ANTHONY LUPO

B.A., College of St. Thomas, 1970

M.S., New Mexico Institute of Mining and Technology, 1972

DISSERTATION

Submitted in Partial Fulfillment of the
Requirements for the Degree of

Doctor of Philosophy in Physics

The University of New Mexico
Albuquerque, New Mexico
December, 1981

DTIC
ELECTE
S FEB 3 1982 D
D

REPORT DOCUMENTATION PAGE

READ INSTRUCTIONS
BEFORE COMPLETING FORM

1. REPORT NUMBER	2. GOVT ACCESSION NO	3. RECIPIENT'S CATALOG NUMBER
81-67D	AD-A110098	

4. TITLE (and Subtitle)

Numerical Studies of Gravitational Accretion from X-Ray Heated Stellar Winds

5. TYPE OF REPORT & PERIOD COVERED

THESIS/DISSERTATION

6. PERFORMING ORG. REPORT NUMBER

7. AUTHOR(s)

James Anthony Lupo

8. CONTRACT OR GRANT NUMBER(s)

9. PERFORMING ORGANIZATION NAME AND ADDRESS

AFIT STUDENT AT: University of Nex Mexico

10. PROGRAM ELEMENT, PROJECT, TASK AREA & WORK UNIT NUMBERS

11. CONTROLLING OFFICE NAME AND ADDRESS
AFIT/NR
WPAFB OH 45433

12. REPORT DATE

Dec 1981

13. NUMBER OF PAGES

139

14. MONITORING AGENCY NAME & ADDRESS(If different from Controlling Office)

15. SECURITY CLASS. (of this report)

UNCLASS

15a. DECLASSIFICATION/DOWNGRADING SCHEDULE

16. DISTRIBUTION STATEMENT (of this Report)

APPROVED FOR PUBLIC RELEASE; DISTRIBUTION UNLIMITED

17. DISTRIBUTION STATEMENT (of the abstract entered in Block 20, If different from Report)

APPROVED FOR PUBLIC RELEASE AFR 190-17.

22 JAN 1982

FREDRIC C. LYNCH, Major, USAF
Director of Public Affairs
Air Force Institute of Technology (ATC)
Wright-Patterson AFB, OH 45433

18. SUPPLEMENTARY NOTES

APPROVED FOR PUBLIC RELEASE: IAW AFR 190-17

19. KEY WORDS (Continue on reverse side if necessary and identify by block number)

20. ABSTRACT (Continue on reverse side if necessary and identify by block number)

ATTACHED

Accession For
NTIS GRA&I ☒
DTIC TAB ☐
Unannounced ☐
Justification_____
By_____
Distribution/
Availability Codes
Dist | Avail and/or Special
A

DTIC COPY INSPECTED

DD FORM 1473 1 JAN 73 EDITION OF 1 NOV 65 IS OBSOLETE

82 02 01 082

UNCLASS

James Anthony Lupo
_____
Candidate

Physics and Astronomy
_____
Department

This dissertation is approved, and it is acceptable in quality
and form for publication on microfilm:

Approved by the Dissertation Committee:

David S. King , Chairperson
_____

_____

H. S. Ahluwal
_____

Byron D. Dieterle
_____

J. Woodall
_____

_____

_____

_____

Accepted:

_____
Dean, Graduate School

_____
Date

iii

ACKNOWLEDGEMENTS

NUMERICAL STUDIES OF GRAVITATIONAL ACCRETION
FROM X-RAY HEATED STELLAR WINDS

James Anthony Lupo

B.S., Physics, College of St. Thomas, 1970
M.S., Physics, New Mexico Institute of Mining and Technology, 1972
Ph.D., Physics, University of New Mexico, 1981

We present three numerical models of accretion from radiation driven stellar winds onto compact objects in massive X-ray binary systems. The wind is given a velocity profile consistent with a radiatively driven wind, and a "negative mass" gravitational potential is derived from this profile to represent the wind driving force in the hydrodynamic equations. An X-ray heating model is used which determines the X-ray heating time from the Compton heating time and the known steady state energies for optically thin gas illuminated by X-rays. This allows X-ray heating to be included in the hydrodynamic equations. The X-ray luminosity is held proportional to the accretion rate, assuming that the gravitational potential energy released is equivalent to 10% of the infalling rest-mass energy. A two-dimensional Eulerian computer code is used to solve the equations of motion. Model estimates of the ionization structure, accretion rates and flow characteristics, and the effects of thermal instabilities are discussed. The impact of the X-ray radiation on the wind driving force is demonstrated. Results indicate a possible mechanism for slow X-ray flares, such as observed in 4U1700-37.

X-rays : binaries -- stars : winds -- stars : accretion

TABLE OF CONTENTS

LIST OF FIGURES

LIST OF TABLES

NUMERICAL STUDIES OF GRAVITATIONAL ACCRETION FROM

X-RAY HEATED STELLAR WINDS

I. INTRODUCTION

One category of well studied cosmic X-ray sources are those found in binary star systems. The most luminous of these objects are the massive X-ray binary stars. These massive X-ray binaries typically contain an O or B class supergiant primary with a mass of 20 M_θ or greater. The secondary is a compact object, such as a white dwarf, neutron star, or, possibly, a black hole, with a mass of 10 M_θ or less. The secondary is the source of the X-ray emission with luminosities ranging from 10^{36} to 10^{38} erg sec^{-1} (see the recent source compilation by Amnuel, Guseinov, and Rakhamimov 1979, and references cited therein). Observations of O and B supergiants have shown that these stars often have strong stellar winds with mass loss rates of up to 10^{-4} M_θ yr^{-1} and terminal wind velocities on the order of 10^3 km sec^{-1} (see, for example, Weymann 1963; Morton 1967a,b, 1976; Hutchings 1976, 1980; Conti 1978a,b). Such observations have lent credence to the generally accepted model that the X-ray emission from these binary systems is powered by gravitational accretion of material from the stellar wind onto the secondary. This model was first proposed by Davidson and Ostriker (1973) (see also Lamb, Pethick and Pines 1973).

Development of our current understanding of gravitational accretion began with the work of Hoyle and Lyttleton (1939). They examined the gravitational capture of material by a body moving

supersonically through an intergalactic medium. This study led to the crude, but useful, analytic line accretion model (see also Bondi and Hoyle 1944) in which the accretion rate was estimated using the velocity and density of the flow and the mass of the gravitating body. Bondi (1952) considered spherically symmetric accretion in some detail under the assumption that the gas was polytropic. Hunt (1971, 1979) generated numerical models which examined gravitational accretion near the transition region between subsonic and supersonic flows of an adiabatic gas. Hoffman (1979) created a non-radiative hydrodynamical model of accretion flow in an isothermal gas. Isothermal flow is much closer to the problem of an X-ray source accreting material. The X-rays produce signifcant Compton heating and cooling effects near the secondary. Heating of the gas occurs faster than the material flow times, negating the assumptions of an adiabatic gas. Hoffman found a dense, fluctuating wake downstream from the body. Fluctuations also appeared in the accreting column of matter falling back to the secondary. This resulted in corresponding fluctuations in the expected X-ray luminosity.

Numerous authors (Mestel 1954; Shvartsman 1971; Buff and McCray 1974a) have examined cases of ideal spherical accretion under the influence of radiation. They found that the X-ray radiation could seriously affect the accretion flow under the combined effects of radiation pressure and the increases in gas pressure due to heating of the gas. These increased pressures led to severe reductions in the amount of material accreted. Carlberg (1978), testing radiation

effects analytically in the line accretion model, found that a turbulent wake was probable, and that strong perturbations of the accretion flow were possible depending on the physical parameters of the flow. He concluded that hydrodynamic calculations would be necessary to determine the actual physical states of the accretion flow. Cowie, Ostriker, and Stark (1978) performed a time dependent calculation of spherically symmetric accretion onto compact X-ray objects. They demonstrated strong modulation of the accretion flow due to X-ray heating which led to flaring of the X-ray luminosity. They concluded that their model was of limited application to X-ray binaries because of the strong asymmetries introduced by the high wind and orbital velocities.

The effects of X-ray heating and ionization of diffuse gases were investigated by Tarter, Tucker and Salpeter (1969). More recently, Buff and McCray (1974a) and Hatchett, Buff, and McCray (1976) investigated the heating and ionization of diffuse gas by X-rays including the effects of Compton heating. They pointed out possible multi-valuedness of the temperature function and the possible formation of thermal instabilities (Field 1965). In particular, McCray and Hatchett (1975) considered the effects of X-ray heating on a wind and deduced that such flows could have multiple pressure-density states. Alme and Wilson (1975, 1976) have demonstrated that instabilities will occur in X-ray driven flows. Hatchett and McCray (1977) examined the ionization structure in the stellar wind of an X-ray binary assuming an unperturbed wind and

3

constant luminosity.

The concept of stellar winds driven by radiation pressure was first formulated by Holzer and Axford (1970) and Lucy and Solomon (1970). In 1975, Castor, Abbott and Klein produced a detailed model for a stellar wind which included contributions to the driving force by line absorption in trace elements (for a review, see Casinelli 1979). They found that the principle contributions to the force were due to L-shell absorption lines in the CNO series of elements. They also found a velocity law for the wind which agreed with the earlier studies. But most significantly, they were able to account for the wind velocities and huge mass loss rates inferred from the observations of OB supergiants. The success of this concept raises the possibility that severe interference may exist between the wind and the X-ray radiation through the ionization of the elements responsible for the wind driving force.

Since the accretion model of powering binary X-ray sources is so widely accepted, we have attempted to develop a model which simultaneously treats the hydrodynamic and radiation effects. The model is intended to be self-consistent to the extent that the X-ray luminosity depends directly on the accretion rate. The powering mechanism assumes gravitational accretion from the stellar wind.

In this study, we present three self-consistent models. By adopting the stellar wind model presented by Castor, Abbott, and Klein (1975) we are able to include the force driving the wind as a "negative mass" gravitational potential added to the gravitational

4

potential of the system. This wind model enables us to account for the impact of the X-ray ionization on the wind. Hatchett, Buff, and McCray (1976) were able to determine the ionization equilibrium for various elements in a gas exposed to X-rays as a function of a single parameter. We make use of the parameter in our model to determine the ionization state of the elements primarily responsible for the wind force. The ionization state in turn determines the effectiveness of the driving force included in the hydrodynamic equations. The X-ray luminosity is held proportional to the accretion rate, thus allowing the luminosity to vary with any disturbances set up in the flow by the X-rays. X-ray heating rates are explicitly calculated from the hydrodynamic variables. The resulting calculations provide an insight into the flow characteristics and the overall ionization structures of the wind.

In Chapter II, we summarize the observed characteristics of several well known X-ray binaries, and describe the two broad classes of such objects. The generally accepted powering mechanism converts the gravitational potential energy of infalling matter into thermal energy. We discuss the two most likely means of providing the necessary matter, namely potential overflow and gravitational accretion from a stellar wind, with emphasis on the latter method. The limiting effects of radiation pressure are presented in a discussion of the Eddington luminosity. We then present a physical argument due to van den Heuval (1975) which provides a basis for the existence of the two classes of X-ray binaries.

The methods used to model the physical processes in X-ray binary systems are presented in Chapter III. Here we present the equations of motion with two terms added for the X-ray heating and the stellar wind driving force, along with their derivations. The X-ray heating effects are handled in terms of an X-ray heating time computed from the Compton heating time and from the known steady state energies of a gas exposed to X-ray radiation. The wind force term is derived from the stellar wind model present by Castor, Abbott, and Klein (1975). We show that their wind velocity law can be used to give an effective potential for the force acting on the wind. Finally, we discuss the Lax-Wendroff two-step finite differencing method which is used to numerically solve the equations of motion.

In Chapter IV, we present the tools required to develop the physical parameters for our models. Since we require the luminosity to be proportional to the accretion rate, we derive relationships which give the needed accretion rates and primary mass loss rates in terms of the other binary parameters. We then present the physical arguments used to determine the acceptability of the derived parameters.

Three different models were considered in this study, using two different binary systems as guides for parameter selection. These two systems were 4U0900-40 (Vela X-1) and 4U1700-37. The parameters for these systems are given in Table 2.1. The first two models were designed to provide reasonable continuity between previous hydrodynamic studies involving constant material flow past an

accreting body and models which allow both variations in wind ionization and variable material velocities. The X-rays are allowed to heat the wind material, but no attempt is made to alter the wind ionization structure and thereby modify the wind driving force.

We present Model 1 in Chapter V. This model is based on the 4U0900-40 system and model parameters are very close to those observed in the actual system. We find that the accretion rates obtained are a factor of 2 below those predicted by the line accretion model. The wind driving force is found to dominate the secondary's gravitational force beyond a certain distance from the secondary. We also demonstrate that the flow is dominated by hydrodynamics rather than X-ray heating effects. The X-ray heating is shown to introduce a thermal instability into the flow. It also supresses the formation of an accretion column, causing most of the accreted material to flow in from the side regions of the wake.

Model 2 is presented in Chapter VI. While this model is also based on the 4U0900-40 system, the model parameters were adjusted to place it in a state such that the flow is dominated by the X-ray heating rather than the hydrodynamics. The resulting model shows a large deviation from the behavior suggested by the line accretion model. The accretion rate is severely impaired, and the model developes a very hot, rarified region in the central core of the wake. The model also has a thermal instability present in the flow which is similiar to that found in Model 1.

Prior to generating a model which would allow the wind force to

vary, we produce a simplified ballistic model of the wind flow under the impact of extreme X-ray ionization. The study, presented in Chapter VII, indicates that even severe modification of the wind force should not significantly reduce the amount of material available for accretion by the secondary. It does demonstrate that severe three-dimensional effects are present in the flow for high X-ray luminosities. We utilize the study of ionization states in a wind exposed to X-rays presented by Hatchett, Buff, and McCray (1976) to estimate a value for our heating parameter at which the wind is considered turned off. The results of these two studies provide additional constraints for our Model 3.

In Chapter VIII we develop the parameters for Model 3 and present the results of our calculation. Due to the restrictions we develop in Chapter VII, we select 4U1700-37 as our base system. The model parameters are constrained to be in close agreement with the observed parameters of the system. Model 3 differs from the previous two in that we allow the wind force to be affected by the X-ray radiation. The ability to turn off the wind force sets up a feed back mechanism in the wind flow. This mechanism leads to large variations in the wind density. As these density fluctuations pass by the secondary, they cause peaks in the accretion rate which result in slow X-ray flares. The flares show a variation of 3 orders of magnitude over a time scale of about 2 hours. This flaring can be compared with the slow flares observed in 4U1700-37.

Finally, in Chapter IX, we discuss the results of our model

8

calculations. The scaling of our model parameters to match other systems is discussed. We perform calculations of the optical depths in the models and find that the models become optically thick in regions far from the secondary, particularily in the case of Model 3. We then discuss the weaknesses of Model 3, and compare our results to some of the most recent work in the field. In particular, we compare our models to those produced by Livio, et al (1979) and Hoffman (1979). We also compare our results to Carlberg's (1978) analytic study of radiation effects in the line accretion model.

II. THE X-RAY BINARY STARS

A. Observational Summary

Following Blumenthal and Tucker (1974) we define a compact X-ray source as one identified with a stellar object, or one which exhibits variability in its X-ray luminosity by a factor of 2 or more on a time scale of days or less. One important sub-group is composed of the X-ray binary stars. In these systems, one of the stars is a normal star (hereafter referred to as the primary) and the other (the secondary) is a compact object such as a white dwarf, a neutron star, or a black hole. They typically have luminosities of 10^{36} to 10^{38} ergs sec^{-1} in the 2-10 keV portion of the X-ray spectrum. The characteristics of some of the better studied of these stars are given in Table 2.1. Except for the X-ray pulsars which have sharply defined periodic variations in their luminosities, we see that the luminosities of these objects are erratic in nature showing both slow and rapid flaring behavior over a large range of luminosities.

By examining the masses of the objects listed in Table 2.1, we find that they can be put into one of two broad classes. One class has low mass primaries of around 2 M_θ or less. The second class contains O and B class supergiant primaries with masses of 20 M_θ or more. This second class is referred to as the massive X-ray binaries. In both classes, the secondary masses are typically 1 or 2 M_θ. With the recent improvement in X-ray observations, there is growing evidence for a third class of X-ray binary (Amnuel, Guseinov, and Rakhamimov 1979). This class has luminosities of 10^{33} erg sec^{-1}

Characteristics of Selected X-Ray Binary Stars

TABLE 2.1

X-RAY SOURCE NO. (other names)	SYSTEM Period (days) Seperation (R_0)	PRIMARY Spectral Type Name Mass ($M_\odot$) Luminosity (ergs sec^{-1}) Radius ($R_\odot$)		SECONDARY Mass ($M_\odot$) Peak Luminosity (ergs sec^{-1})
	Remarks: additional comments on X-ray observations			
01157-737 (4U0115-73) (SMC X-1)	3.9 29	B0 Ia SK 160 28 8×10^{38} 18		2.5 7.5×10^{38}
	Remarks: Variability: on order of minutes in time and factor of 100 in magnitude. X-ray eclipses. Extended low luminosity periods. 1.5-3.0 keV spectral cutoff.			
03522+308 (X Per)	580. ...	Be X Per		... 5×10^{38}
05130+459	104.2 21.4	F8-G0 III ... 2.9		3.0 1×10^{31} (G5 III)

TABLE 2.1. Continued

09002-403 (4U0900-40) (VELA X-1)	8.96 52	B0.5Iab HD77581 22 1.5×10^{39} 33	2 1×10^{37}	

Remarks: Variability: on order of 0.1 secs in time and factor of 100 in magnitude. Slow flares on scale of 1 hr. X-ray eclipses. 2.5-4.4 keV spectral cut-off. Occasionally turns off for periods of ½ day (Alme 1974). Primary mass loss rate of $3.5-14.0 \times 10^{-6}$ $M_{\odot}$ yr^{-1} (Hutchings 1976). Primary at or near potential lobe (Hutchings 1976, Conti 1978a).

11190-603 (4U1118-60) (CEN X-3)	2.09 19	06.5eq V-III V779 Cen (Kreminski's) 20 1×10^{39} 12	1.5 8×10^{37}	

Remarks: X-ray Pulsar, 4.84 sec period. Magnitude varies by factor of 10. X-ray eclipses. 1.5-4.2 keV spectral cut-off. Slow eclipse transitions showing absorption rather than cut-off, and extended lows observed in pulsed component (Alme 1974).

16170-155 (SCO X-1)	.79 ...	Emission V818 Sco	... 1×10^{37}	

Remarks: Variability: on order of minutes and factor of 2 in magnitude. approx. 0.5 keV spectral cut-off. Slow flares on times of 0.1 to 1 hr.

TABLE 2.1. Continued

16560+354 (4U1656+35) (HER X-1)	1.7 8	A7-B0 HZ Her 2.1	1.3 1x10^{37}

Remarks: X-ray Pulsar, 1.24 sec period. X-ray eclipses. 35 day and suspected 70 periods of high/low luminosity. Magnitude varies by factor of 10. 1.5-3.2 keV spectral cut-off.

17005-377 (4U1700-37)	3.41 30	O6f HD153919 30 4x10^{39} 21	1.5 8x10^{36}

Remarks: Variability: on order of 1 sec in time and factor of 100 in magnitude. X-ray eclipses. 2.1-5.5 keV spectral cut-off. Slow flares on scale of 2-3 hours (Pietsch, et al 1980). Primary mass loss rate of 7.5-30.0x10^{-6} $M_\odot$ yr^{-1} (Hutching 1976). Primary at or near potential lobe (Hutchings 1976, Conti 1978a).

17401-391	5.6 ...	B1 V λ Sco	... 2x10^{33}

TABLE 2.1. Continued

18149+498 (4U1813+50)	0.129 1.2	Emission Am Her 0.4 ... 0.36	1.0 2×10^{33}
19564+350 (4U1956+35) (CYG X-1)	5.6 43	09.7Iab HDE226868 25 1.4×10^{39} 21	10 $2\text{-}8\times10^{37}$

<u>Remarks</u>: Variability: on order of 50 msec in time and factor of 10 in magnitude. Secondary considered a likely candidate for a black hole. Primary mass loss rate of $1.2\text{-}5.0\times10^{-6}$ M_θ yr^{-1} (Hutchings 1976). Primary at or near potential lobe (Hutchings 1976, Conti 1978a).

20305+407 (4U2030+40) (CYG X-3)	0.2 (16.9?) ...	Ifra-red and strong radio flare source tentatively identified with 4.8 hr period.	... 2×10^{38}

<u>Remarks</u>: Variability: on order of minutes in time and factor of 3 in magnitude. 2.9-4.0 keV spectral cut-off. Slow variations (flares?) on order of 1 day.

TABLE 2.1. Continued

21426+380   .86 (13.6?)   G   ...
(CYG X-2)   ...   V1341 Cyg   4x10^{36}
             ...   .

Remarks: Variability: on order of
minutes and factor of 2 in magnitude.
0.5 keV spectral cut-off.

Table 2.1. This table has been compiled from catalogs given by: Forman, Jones, Cominsky, Julien, Murray, Peters, Tanabaum, and Giacconi (1978) (The 4'th UHURU Catalog of X-ray Sources), and Amnuel, Guseinov, and Rakhamimov (1979) (A Catalog of X-ray Sources). The X-ray Source Numbers are from the latter listing. Remarks have been extracted from Blumenthal and Tucker (1974), unless noted otherwise. Entries are the best determined values. Strong alternate determinations are shown with a "?". Undetermined data is entered as "...".

15

or less and have indistinct, extended, infra-red sources as their primaries.

Since the compact objects are the sources of the X-rays in these systems, the most likely method of powering them is through the release of gravitational potential energy from material falling onto the object (for reviews see Blumenthal and Tucker 1974; Giacconi 1976; Gurskey 1976). The amount of energy released in the form of radiation by the infalling matter was shown classically by Zel'dovich and Shakura (1969) and relativistically by Alme and Wilson (1973) to be on the order of 10 to 20 percent of the matter's total rest-energy. At this rate of energy release, we need only provide an accretion rate of 10^{-10} to 10^{-8} M_θ yr^{-1} to achieve the 10^{36} to 10^{38} ergs sec^{-1} luminosities observed. Such mass capture rates can easily be provided by one of two different mass exchange mechanisms present in binary systems.

B. Mass Exchange Mechanisms

In 1973, Davidson and Ostriker proposed two models for X-ray binaries based on the two mass exchange mechanisms. Figure 2.1 shows schematically the processes involved. Figure 2.1(a) depicts the first of these mechanisms, that of potential overflow. The figure-8 shape represents the critical gravitational potential lobe, which is actually a surface of constant gravitational potential. Gravitational potentials at greater distances than the critical potential have surfaces which surround both stars. Potentials closer than the critical potential have surfaces which surround each star
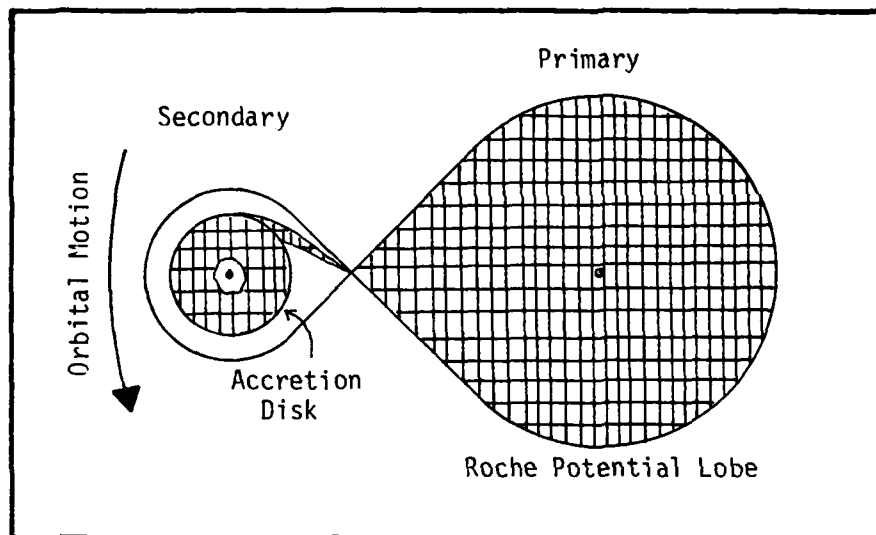
Figure 2.1(a). Roche Lobe Overflow. The primary's atmosphere (cross-hatching) has filled the critical potential lobe and is overflowing onto the secondary. (Not shown to scale.)
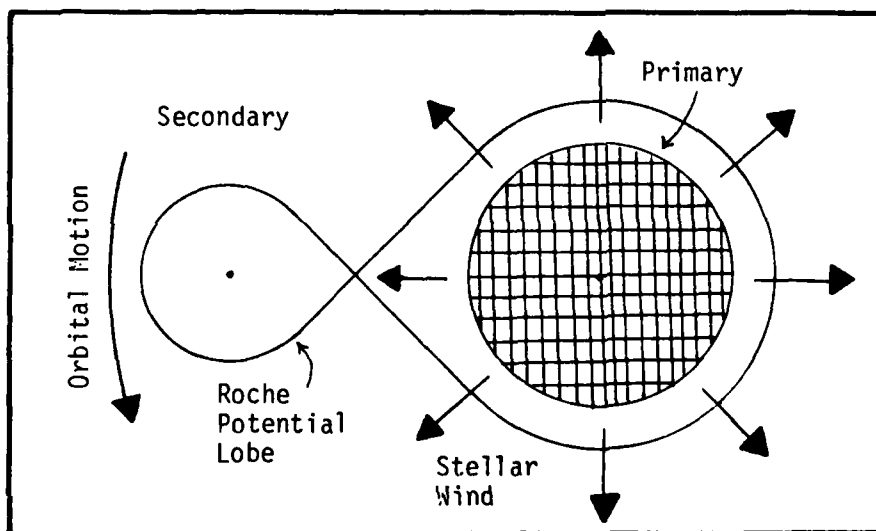
Figure 2.1(b). Accretion from a Stellar Wind. The primary does not fill the critical potential lobe. The secondary sweeps up stellar wind material from its orbit. (Not shown to scale.)

individually. To express these surfaces analytically, let us take coordinates x, y, and z such that the z-axis passes through the center of mass of the system, normal to the orbital plane, and the x-axis lies on the line-of-centers with the neutron star on the negative x-axis. The gravitational potential at any point is then given approximately by (Davidson and Ostriker 1973)

$$\Phi = -G \ (M_x/r_x + M_0/r_0 - X(x,y)). \tag{2.1}$$

M_x and r_x are the mass of the secondary and the distance from it. Likewise, M_0 and r_0 are the mass of the primary and the distance from it. $X(x,y)$ is a centrifugal term which accounts for the rotational characteristics of the binary system. Let us consider the form of $X(x,y)$ for two limiting situations. If the rotational period of the primary is synchronized to the secondary's orbital period, we are in the Roche limit and $X(x,y)$ is given by

$$X(x,y) = \tfrac{1}{2} \ (M_0 + M_x)(x^2 + y^2) \ a^{-3} \ , \tag{2.2}$$

where a is the binary seperation. The second limit is if the primary is not rotating at all. This case is called the tidal limit, and $X(x,y)$ is given by

$$X(x,y) = x \ M_x/a^2. \tag{2.3}$$

An actual binary system most likely lies somewhere between these two limits.

In Fig. 2.1(a), the cross-hatching represents material in the atmosphere of the primary. The atmosphere has expanded to completely fill the critical potential lobe. Under these conditions, material can now flow onto the secondary, since it is at the same potential as

the primary. Angular momentum causes the material to spiral in around the secondary, creating an accretion disk. Material transferring from the inner edge of the disk to the surface of the secondary releases gravitational potential energy, thus powering the X-ray luminosity. A shocked region may also contribute to the radiation at the point where the inflowing stream joins the outer edge of the accretion disk.

Evolutionary senarios developed to explain the formation of massive binary stars (not necessarily X-ray binaries) have shown that the necessary mass-exchange rates are quite easily obtained (Kopal 1959; Paczynski 1971). Potential overflow, however, presents us with the major problem of too rapid an exchange of the material. The exchange rate tends to speed up as the primary loses mass and the secondary gains it. In a very short period of time, the material flow can completely smother the secondary in a X-ray opaque cloud.

The second mechanism is gravitational capture of material from the primary's stellar wind. Hoyle and Lyttleton (1939) developed the analytical line accretion model to explain how a galaxy moving through the intergalactic medium could gain matter. They argued that the mass accretion rate is dependent only on the density of the passing material, its velocity, and the mass of the gravitating body. An accretion radius is defined by

$$R_a = 2\,G\,M\,v^{-2} , \tag{2.4}$$

where G is the gravitational constant, M is the mass of the gravitating body, and v is the velocity the material would have if

the gravitating body were not present. The unperturbed kinetic energy of material within this radius is less than the gravitational potential energy. Under such conditions, we have a simple criterion for determining whether or not the material can be gravitationally captured. Since material within this radius is energetically favored to be captured, the capture rate is dependent only on the mass flux through the cross section defined by R_a and some efficiency factor. So, we find the accretion rate to be given by

$$dM/dt = \pi R_a^2 \rho v \alpha , \qquad (2.5)$$

where ρ is the unperturbed density of the wind near the body, and α is an efficiency parameter lying between 0.5 and 1. Hunt (1971, 1979) performed numerical calculations of gravitating bodies moving through an interstellar gas at various Mach flow numbers. He demonstrated that α tends to increase with increasing Mach number. This increase is attributable to the fact that proportionately more energy is dissipated in the shock at high Mach numbers than at lower ones. Thus material which has passed through a highly supersonic shock is easier to capture gravitationally. Davidson and Ostriker combined this theory with the observations that O and B class stars have high mass-loss rates on the order of 10^{-7} to 10^{-4} M_θ yr^{-1} (Weymann 1963; Morton 1967a,b, 1976; Conti and Cowley 1975; Hutchings 1976; Conti 1978a, Conti and Germany 1980). They then noted that these mass loss rates can provide winds of suitable density and velocity near the secondary so as to allow the line-accretion model to support the observed luminosity. They therefore concluded that

gravitational accretion from a stellar wind could be one workable method of powering the binary X-ray stars. This mechanism is depicted in Fig. 2.1(b).

Gravitational accretion is also the most likely method for powering the possible third class of X-ray binary. In these systems, the secondary is pictured as orbiting within the extended tenuous atmosphere of the primary (Amnuel, Guseinov, and Rakhamimov 1979 and sources therein). At the present time there is insufficient observational data on these systems to determine the actual powering mechanism. Binary system parameters are needed to determine the velocities of the secondaries and the density of the atmospheres in their orbits.

In either of the two methods discussed above, there is a limit to the maximum attainable X-ray luminosity. This is the so called Eddington luminosity, or Eddington limit, at which the radiation pressure due to the emergent X-rays balances the force of gravity. In the case of spherically symmetric accretion in which Thompson scattering is the dominant opacity, this limiting luminosity for material of cosmic abundances is given by (Eddington 1926)

$$L_{edd} = 4 \pi G M c \kappa_e^{-1} \tag{2.6}$$

or,

$$L_{edd} = 1.3 \times 10^{38} M/M_\odot \text{ ergs sec}^{-1}, \tag{2.7}$$

where κ_e is the electron scattering opacity. Any excess material in the accretion flow is blown off by the radiation pressure. Detailed one-dimensional models of spherical accretion near the Eddington

21

limit have been presented by Vitello (1978). He verified that sharp cut-offs near the Eddington limit existed for several types of flow. He also speculated that any instabilities introduced into the flow may result in luminosities higher than the Eddington limit. Two dimensional instabilities, such as the Rayleigh-Taylor instability, or the creation of photon bubbles as suggested by Prendergast and Spiegel (1973), may provide the necessary instabilities in the flow.

C. System Life Time Considerations

We are now faced with the problem that both of these mechanisms are restricted in their applicability. The potential overflow mechanism appears to be too effective at providing material, while accretion from a stellar wind does not work well for primaries with masses less than 19 M_θ. Van den Heuval (1975) demonstrated the limits of applicability for each of these mechanisms by considering the lifetimes of various binary systems as a function of their masses. His argument proceeds as follows.

The time scale over which the primary will lose 80% of its mass is given by

$$\tau = 3 \times 10^7 \ (M_o/M_\theta)^2 \ R_\theta/R_o \ L_\theta/L_o \ , \qquad (2.8)$$

with τ given in years. From this mass loss rate, Van den Heuval arrived at an average accretion rate given by

$$dM_x/dt = 2.66 \times 10^{-8} \ R_o/R_\theta \ L_o/L_\theta \ M_o/M_\theta \ , \qquad (2.9)$$

with the accretion rate given in $M_\theta \ yr^{-1}$. If the accretion rate onto the secondary exceeds about $10^{-6} \ M_\theta \ yr^{-1}$, then the secondary will become engulfed in an optically thick cloud, allowing no X-rays to

22

escape. However, there is a period at the onset of the overflow during which the mass loss rate and the consequent accretion rate of Eq. 2.9 is much lower. This period exists for approximately 1% of the total exchange time given by Eq. 2.8.

From Eq. 2.8 and 2.9, Van den Hueval argued that systems with a primary more massive than 2.1 M_Θ would produce an overflow rate sufficient to smoother the X-ray source. In addition, the brief start-up period from Eq. 2.8 would be on the order of 1000 years or less. This brief period would make it highly unlikely that such a source could be observed (see also Savonije 1979; Thomas 1977).

The case for systems with primaries less massive than 2.1 M_Θ is different. The peak accretion rates given by Eq. 2.9 are less than 10^{-6} M_Θ yr^{-1}. Thus the X-ray radiation is not likely to be smoothered, and the mass-exchange period is very long. Hence, it's much more probable that such a system could be observed.

As for accretion from a stellar wind, van den Heuvel argued that primaries less massive than 20 M_Θ would have wind densities too low to supply the needed accretion material. However, those more massive than 20 M_Θ would have sufficient wind density. In addition, such stars could be expected to sustain these winds well in excess of 10^6 years. This "life time" criterion for X-ray binaries appears to agree well with the binaries for which we have sufficient system data. So far, all X-ray binaries meet one of these two criterea. Thus, one of the constraints on designing a model driven by accretion from a stellar wind is to require the primary to have a mass of 20 M_Θ

or greater. This is in addition to the goal of attempting to model the X-ray production so as to be in reasonable agreement with the observations.

There are recent optical observations of the massive X-ray binaries (Hutchings 1976, Conti 1978b) which appear to indicate that the primaries fill or nearly fill their potential lobes. This fact could be troublesome if the primaries do indeed fill the lobes, for as noted, there is no way to prevent the onset of run-away overflow. If the primaries only approach filling their lobes, there may be a much more complicated accretion process going on. Alme and Wilson (1976) have shown that X-ray heating of the atmosphere of a primary which is within 80% of filling its lobe can cause an outflow of material sufficient to power the X-ray source. The massive binaries may therefore be utilizing both accretion from the primaries' massive winds and X-ray induced overflow. If the wind in a given system is sufficient for powering the X-ray source, there may then be a new problem of limiting the total accretion rates obtained from several exchange processes operating simultaneously. Such circumstances are not examined in this study.

III. THE MODELING METHOD

One of the major difficulties encountered in modeling hydrodynamic and radiation effects is the large difference in the time scales over which the two processes occur. The hydrodynamic time scale is governed by the typical scale lengths of the problem and the flow velocities (or the sound velocities if the flow is subsonic). In the region of the model near the secondary, a typical cell dimension is on the order of 10^9 cm. Here the flow reaches its highest velocities of about 10^8 cm sec^{-1}. This requires that the model be able to resolve events in the fluid flow which occur on a time scale of about 10 seconds. Conversely, the X-ray heating times are dominated by the Compton heating time for the high temperatures expected near the secondary. Since the Compton heating time will be discussed more fully in Section C of this Chapter, we will simply note that from Eq. 3.26, we have a typical Compton heating time on the order of 10^{-3} sec. To explicitly follow the X-ray heating, we would require time resolution of less than 10^{-3} seconds. Since material requires about 25000 seconds to move through the problem mesh, such a small time resolution would be prohibitively expensive in terms of computational resources. In the developments which follow, we describe a method by which the model can utilize a time resolution suitable for the fluid flow and still approximate the X-ray heating effects.

A. The Equations of Motion

We begin our discussion of the development of our model systems

with a presentation of the fluid equations. These were taken in conservative form (Potter 1973) with two additional terms incorporated to account for X-ray heating and the stellar wind driving force. For the conservation of mass, we have

$$\partial \rho / \partial t + \nabla \cdot \rho \underline{v} = 0 , \qquad (3.1)$$

and for the conservation of energy

$$\partial E / \partial t + \nabla \cdot E \underline{v} = -P(\nabla \cdot \underline{v}) + Q(\nabla \cdot \underline{v}) + (E_{ss} - E)t_x^{-1} , \qquad (3.2)$$

while the conservation of momentum is given by

$$\partial \underline{p} / \partial t + \nabla \cdot \underline{p} v = \rho \nabla \Phi_g + \rho \nabla \Phi_w - \nabla P - \nabla Q . \qquad (3.3)$$

where

ρ = mass density,

$\underline{p}$ = momentum density,

E = energy density,

P = pressure,

$\underline{v}$ = velocity,

Q = Richtmyer-von Neumann artifical viscosity,

Φ_g = gravitational potential,

Φ_w = effective wind potential,

t_x = effective X-ray heating time,

E_{ss} = steady-state energy of the gas.

The Richtmyer-von Neumann artifical viscosity is a numerical aid required by the finite difference equations used in the computer simulation (see Richtmyer and Morton 1967, or Potter 1973). It serves to smooth out shocks which form in the flow over several zones of the model mesh, thus allowing the code to approximate the

26

discontinuity presented by the shock. This will be discussed in greater detail, along with the differencing method, in Section D.

B. The Wind Force Term

Models aimed at explaining the huge mass losses observed in O and B class supergiants have been presented by Lucy and Solomon (1970) and Castor, Abbott, and Klein (1975). Castor, Abbott and Klein demonstrated that the source of the forces driving the mass loss was line-absorption in CNO series elements, primarily the UV lines produced by the L-shell electrons. The photons absorbed by the atoms are primarily traveling radially outward from the star. The excited atoms then re-emit photons isotropically as they return to their unexcited state. This results in a net outward momentum gain for the atoms.

Castor, Abbott and Klein took the force to be expressed by

$$f = M(t) F \sigma_e c^{-1}, \qquad (3.4)$$

where σ_e is the electron scattering coefficient, F is the total radiant flux, and M(t) is a force multiplier dependent on atomic populations, oscillator strengths, and optical depth. They then set up the fluid equations, assuming spherically symmetric outflow, and specifically accounted for gravity, gas pressure, continuum radiation pressure, and line radiation pressure. They found a solution which yields a nearly constant ratio of wind acceleration to gravitational acceleration. The forces were also found to be sufficient to support both the high mass loss rates and the terminal wind velocities observed in supergiants. In particular, they were able to determine

an approximate relationship for the velocity of the wind as a function of its distance from the primary. This velocity law is given by

$$v = v_\infty (1 - R_0/r)^{\frac{1}{2}} , \qquad (3.5)$$

where v_∞ is the wind velocity at an infinite distance from the primary, R_0 is the wind initiation radius on the order of the primary radius, and r is the radius of interest. The success of their model indicates that the gravitational accretion driven binary X-ray source model contains a serious complication. McCray (1974) and McCray and Hatchett (1975) speculated that if the X-ray luminosity was high enough, the atoms responsible for the wind force would be fully stripped of their L-shell electrons, suppressing the wind in those regions so illuminated. They believed that if the velocity was reduced, accretion may be facilitated, but also indicated that the exact effect was uncertain.

We note here that they also claimed that the orbital periods were comparable with the time it takes the wind to move from the primary surface to the secondary's orbit, indicating that there would be strong azimuthal asymmetry in the wind with respect to the secondary's position. A simplified ballistic analysis presented in Chapter VII found that the time it takes the wind to move from the surface of the primary to the orbit of the secondary is actually on the order of 10% of the orbital period. Our Model 3, which is presented in Chapter VIII, directly addresses the question of what impact the X-rays have on the structure of the wind.

28

To account for the stellar wind and its driving force, we use Eq. 3.5 to derive a potential for the driving force. We first apply the chain rule to Eq. 3.5, yielding

$$\partial v/\partial t = \partial v/\partial r \; \partial r/\partial t \; . \qquad (3.6)$$

Since $\partial r/\partial t$ is just v, we can differentiate Eq. 3.5 with respect to r and substitute the result into Eq. 3.6, giving us

$$\partial v/\partial t = \tfrac{1}{2} \, v_\infty^2 \, R_0 \, / \, r^2 \; . \qquad (3.7)$$

To get the potential, we now set Eq. 3.7 equal to the negative gradient of the potential so that integrating with respect to r gives the desired

$$\Phi_W = \tfrac{1}{2} \, v_\infty^2 \, R_0/r \; . \qquad (3.8)$$

This is in effect a "negative mass" gravitational potential and can thus be directly incorporated into the conservation of momentum equation (Eq. 3.3).

C. The X-ray Heating Term

Of more importance is the last term of Eq. 3.2, representing the X-ray heating effect. Several previous works (Tarter, Tucker, and Salpeter 1969; Hatchett, Buff, and McCray 1976) have shown that the ionization and temperature structure of an optically thin gas with cosmic abundances can be completely described in terms of a single parameter, ξ, for a given spectral shape, where

$$\xi = L_x \, / \, n \, r_x^2 \; . \qquad (3.9)$$

Here, L_x is the X-ray luminosity, n the number density and r_x the distance from the X-ray source.

Using ξ as the independent parameter, Tarter (see reference in

Alme and Wilson (1974)) and Alme and Wilson (1974) calculated the resultant equilibrium temperatures for an optically thin gas exposed to X-rays. Since the results are dependent on the spectrum of the X-rays, they both used a 22-keV exponential spectrum representative of cosmic X-ray sources. The results of their calculations are displayed as curves 1 and 2 in Fig. 3.1. Figure 3.1 thus allows the equilibrium temperature of a gas to be specified for any given ξ. Curves 3 and 4 serve as analytical fits for just this purpose and will be utilized later in the determination of the X-ray heating contribution to the hydrodynamic equations.

For compatibility with the computer code adapted for the models, we have defined ξ to be

$$\xi = \rho \, r_x^2 \, / \, L_x \, . \tag{3.10}$$

We can relate Eqs. 3.9 and 3.10 through ρ and n by first noting that (Clayton 1968)

$$\rho = n\mu/N_0 \, , \tag{3.11}$$

where N_0 is Avogadro's number and μ is the mean atomic weight. Now, μ is given by

$$\mu = \sum f_z n_z / A_z \, , \tag{3.12}$$

where f_z is the fraction by weight of atomic element Z, n_z is the number of particals contributed by element Z, and A_z is the atomic weight of element Z. For an un-ionized gas of cosmic abundances, we have

$$\mu = \sum f_z / A_z = 1.16198 \, . \tag{3.13}$$

Thus, we find that ρ and n are related through Eq. 3.12 by
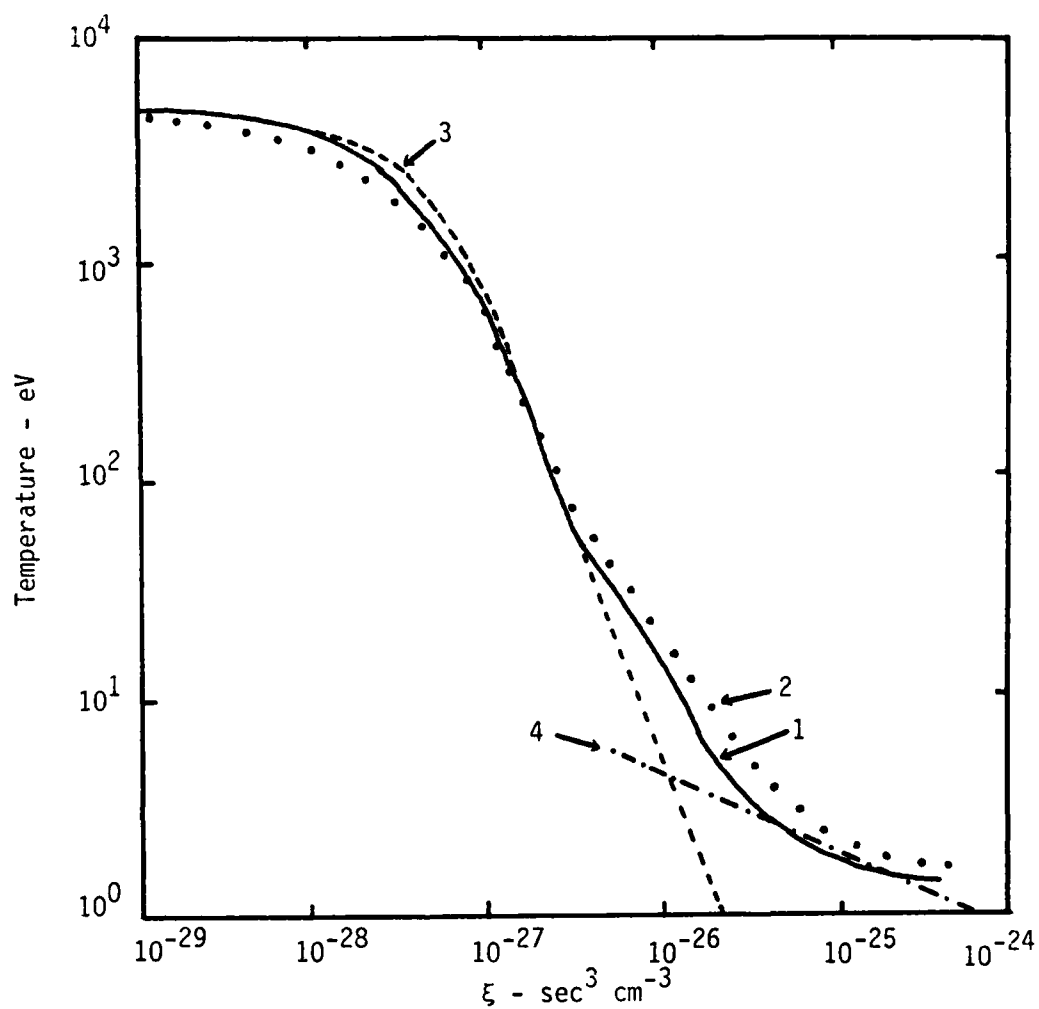
Figure 3.1. Steady State Temperature vs ξ. Steady state temperature as a function of ξ is displayed here for an optically thin gas exposed to a 22 keV exponential X-ray source. Curve 1 was produced by Tarter (see Alme and Wilson 1974), while Curve 2 was produced by Alme and Wilson (1974). Curve 3 is an analytical fit to the upper portion and is given by Eq. 19. Curve 4 is a fit to the tail and is given by Eq. 20. ξ is not a dimensionless constant, but rather has units of sec ^{3} cm^{-3}.

$$\rho = 1.9294 \times 10^{-24} \, n. \tag{3.14}$$

The X-ray heating rate, including photoionization and Compton scattering, is given by:

$$(\partial E / \partial t)_r = (E_{ss} - E) \, t_x^{-1} . \tag{3.15}$$

Here, t_x is the X-ray heating time, and E_{ss} is the steady state (equilibrium) energy of the gas. E_{ss} is computed using

$$E_{ss} = \rho \, C_v \, T_{ss} , \tag{3.16}$$

with T_{ss} taken from Fig. 3.1 for a given ξ.

Two analytical fits were developed to give the steady state temperature as a function of ξ. The upper portion of the curve is fitted with the dashed line (curve 3) specified by (T in ev)

$$T = \frac{5000}{1 + 7.716 \times 10^{54} \, \xi^2} . \tag{3.17}$$

The roll-off region of the tail is fitted with the straight line (curve 4) specified by (T in ev)

$$T = 1.5689 \times 10^{-9} \, \xi^{-0.362704} . \tag{3.18}$$

From Eq. 3.15, we see that if the gas is below its steady state temperature, heating will occur, while if it is above its steady state temperature, then cooling will occur. The time over which this can occur is called the X-ray heating time. We can estimate the X-ray heating time by first calculating the Compton heating time. This time can be given by

$$t_c = E \, (dE/dt)_c^{-1} , \tag{3.19}$$

where $(dE/dt)_c$ is the Compton heating rate.

The Compton heating rate in an optically thin gas can be derived from one term of the radiation diffusion equation in the form (Alme

32

and Wilson 1974)

$$(\partial E/\partial t)_c = \rho/m_e c \int_0^\infty \kappa_e \{kT \ (\nu \ \partial E_\nu/\partial \nu - 3E_\nu) + h\nu E_\nu\} \ d\nu \ , \quad (3.20)$$

where induced scattering has been neglected. We have assumed an exponential spectrum for our models, so we have

$$E_\nu = A \ e^{-\nu/\nu_0} \ , \quad (3.21)$$

where A is chosen so as to give the magnitude of the spectrum and ν_0 is the characteristic frequency of the spectrum. In this case, $h\nu_0$ is 22 keV.

Substituting Eq. 3.21 into 3.20 and integrating yields

$$(\partial E/\partial t)_c = (h\nu_0 - 4kT) \ \rho \ \kappa_e \ \nu_0 \ A \ / \ m_e \ c \ . \quad (3.22)$$

Since the integral of Eq. 3.21 over all ν gives the total energy in the spectrum, we must have $\nu_0 A$ equal to the radiation energy density, E_r. Equation 3.22 specifies the conditions under which the material will come into equilibrium with the radiation. We are now able to define a characteristic Compton heating time by

$$(\partial E/\partial t)_c = E_r \ \rho \ \kappa_e \ <h\nu> \ / \ c \ m_e \ , \quad (3.23)$$

where $<h\nu>$ is now the characteristic equilibrium energy due to the X-ray spectrum.

The internal energy of the gas can be given by

$$E = \rho \ C_v \ T \ . \quad (3.24)$$

We also have the radiation energy density due to the X-ray luminosity given by

$$E_r = L_x \ / \ 4 \ \pi \ r^2 \ c \ . \quad (3.25)$$

Dividing Eq. 3.24 by Eq. 3.23 and substituting Eq. 3.25 for E_r, we arrive at a characteristic Compton heating time given by

33

$$t_c = \frac{4\pi r^2 m_e C_v T}{L_x \kappa_e \langle h\nu \rangle} . \tag{3.26}$$

For gas of low temperature, the photoelectric effect dominates the X-ray's interaction with the gas. The ionization of atoms in the gas effectively absorbs energy from the incident radiation. Above some transition energy E_t, Compton scattering becomes the dominate energy transfer process between the radiation and the gas. The gas has become highly ionized and the atoms are no longer able to absorb energy by the photoelectric effect. The X-ray heating time is therefore approximated by

$$t_x = \frac{t_c}{1 + (E_t/E)^2} . \tag{3.27}$$

Equation 3.27 allows the X-ray heating time to approach the Compton time whenever E is greater that E_t, and strongly magnifies the X-ray heating effects for E less than E_t.

The material in the stellar wind is assumed to be optically thin. This is based on the fact that the wind density in the region of the secondary is found to be on the order of 10^{-12} g cm^{-3} for mass loss rates required to support the observed X-ray luminosities. Further, with the aid of Fig. 3.1 and Eq. 3.10, we note that strong X-ray heating will occur only close to the secondary. Thus our X-ray heating model will retain its validity even if the material becomes optically thick far from the region of strong heating. Optical depths were calculated through various regions of the models after they were run to determine the validity of this assumption. The

34

resultant optical depths, to be discussed in Chapter IX, show that the models are in fact optically thin near the secondary, but became progressively thicker in the outer regions.

D. The Numerical Method

The equations of motion (Eqs. 3.1-3) are solved utilizing the Lax-Wendroff two-step method for finite-difference equations (Richtmyer and Morton 1967; Potter 1973). This method defines the dependent variables on alternate mesh points from the corresponding fluxes. With respect to Fig. 3.2, this can be visualized by defining the dependent variables at the center of each cell and the fluxes at the center of each face of the cell. The two-step method first computes the new fluxes from the old dependent variables:

$$u_{j+\frac{1}{2}}^{n+\frac{1}{2}} = \frac{1}{2} (u_j^n + u_{j+1}^n) - (F_{j+1}^n - F_j^n) \, \Delta t \, / \, 2 \, \Delta x \ . \qquad (3.28)$$

This is then used to give the fluxes from

$$F_{j+\frac{1}{2}}^{n+\frac{1}{2}} = F(u_{j+\frac{1}{2}}^{n+\frac{1}{2}}) \ . \qquad (3.29)$$

Here, n refers to the n-th time step while j refers to the j-th spacial increment. The new dependent variables are then given by these fluxes as

$$u_j^{n+1} = u_j^n - (F_{j+\frac{1}{2}}^{n+\frac{1}{2}} - F_{j-\frac{1}{2}}^{n-\frac{1}{2}}) \, \Delta t / \Delta x \ . \qquad (3.30)$$

We are now in a better position to discuss the requirement for the Richtmyer-von Neumann artificial viscosity, Q, introduced in Eqs. 3.2 and 3.3. From the finite dimensions utilized by the differencing scheme described above, it is apparent that only phenomena with wavelengths greater than the dimensions of the cells will be accurately described. In a compressible fluid, large amplitude

Figure 3.2. The Lax-Wendroff Mesh. Shown here is the mesh used for the Lax-Wendroff two-step finite differencing scheme. The dependent variables ρ and E are defined on the "main" mesh (dashed lines), while the momenta and other fluxes are defined on the auxiliary mesh (solid lines). The two meshes are most easily pictured as one set of cells with variables defined as zone-centered or face-centered.

disturbances tend to gain energy and steepen into discontinuities or shocks in the flow. In an actual physical shock, the thickness is a function of the viscosity, which acts to transform the kinetic energy of the short wavelength phenomena into thermal energy. If the shock thickness becomes less than the cell dimensions, spurious oscillations are produced by finite differencing methods (Potter 1973). To avoid this problem, Q is introduced to artificially dissipate the kinetic energy of the shock into thermal energy. Q is adjusted so as to spread the shock over several mesh cells. This eliminates the spurious oscillations for the mesh is again able to resolve the features of the shock. The over-all effect is to gain a more physically accurate description of the flow at the expense of losing spatial resolution on the location of the shock. Q is clearly not needed if the natural viscosity of the fluid being modeled is great enough to provide shocks resolvable by the differencing method. If such is the case, the normal viscosity term is used in place of Q in Eqs. 3.2-3.

Cylindrical coordinates are used for the spatial mesh with the axis lying along the line of centers of the primary and secondary (Fig. 3.3). The wind from the primary is approximated as planar flow past the secondary. This is considered acceptable since in the region where the wind is most strongly affected by the secondary's gravity, a radial flow diverges from a planar flow on the order of 10 degrees. The mesh is dimensioned 120 cells along the z-axis by 60 cells radially. Variable zoning is used to give both a fine

37

This end faces Primary.
Wind enters here.

60 R cells

120 Z cells

Secondary's Accretion Region

Axis on line of centers

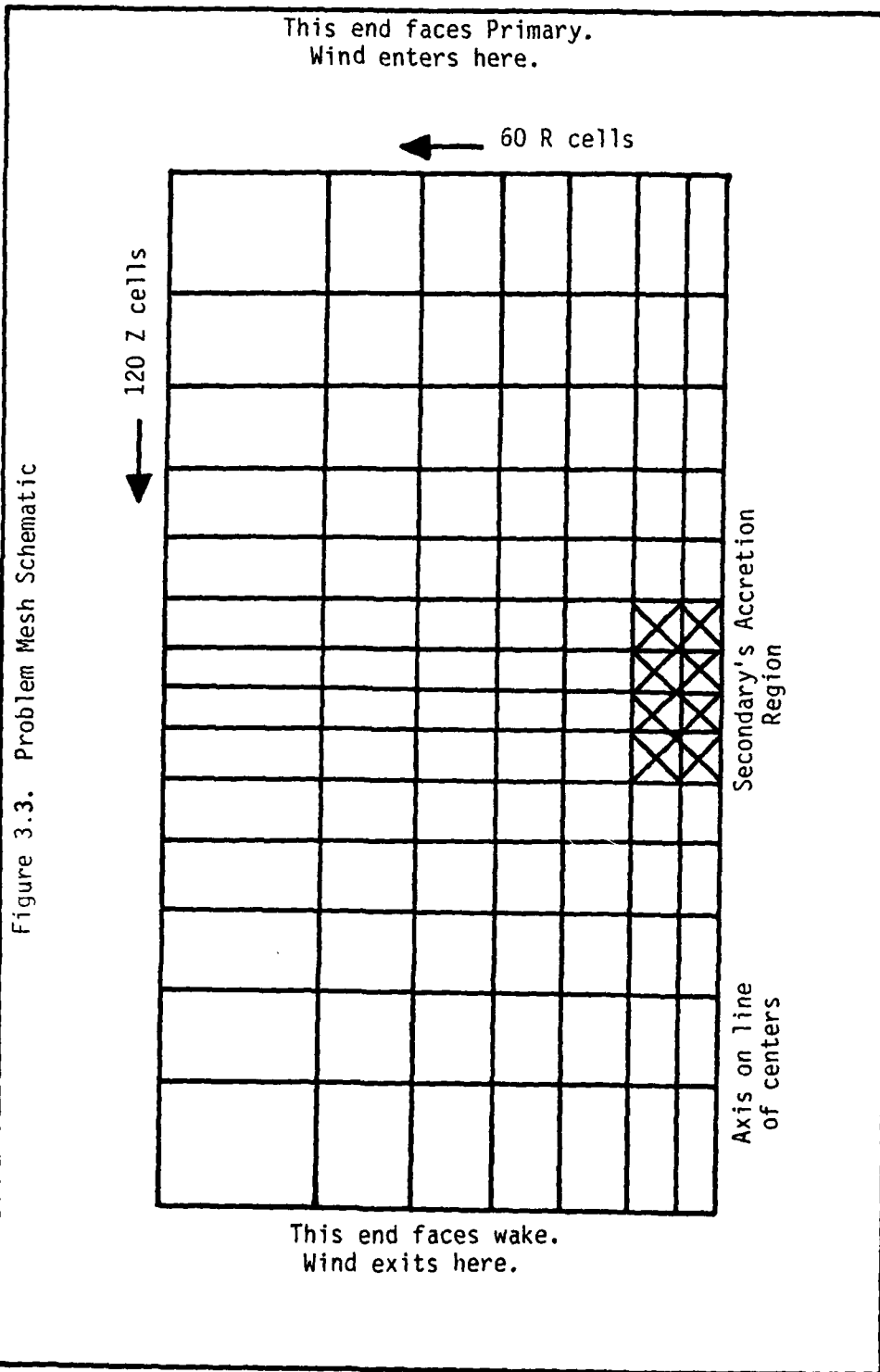This end faces wake.
Wind exits here.

Figure 3.3. Problem Mesh Schematic

resolution near the secondary and a large mesh size with a limited number of zones. A minimum cell dimension of 2.5×10^9 cm represents a compromise between resolution needed near the accretion region of the secondary and computational time available. Since the primary thrust of this study is to examine the flow characteristics and not just the details of accretion we do not feel that this lack of detail close to the secondary is significant.

While the wind flow is more correctly described as a plasma rather than as a gas, magnetic effects have been omitted in these models. One reason is that the minimum dimension of our models is well outside the 10^7 to 10^8 cm magnetospheric radii of neutron stars (Lamb, Fabian and Pringle 1973). Another is that there is little information as to the effects of OB supergiant magnetic fields on their massive winds. In addition, Parker (1972) has presented a mechanism by which such fields, if entrained in the wind, could be dissipated. The final reason is that treatment of the magnetic fields would increase the difficulty of the problem to the point where it could not be handled with the computational resources available.

We have limited the models to two dimensions for several reason. The first is a practical one, namely the lack of the computational resources necessary for a full three dimensional model of this type. We also feel, however, that it is desirable to maintain a link between previous two-dimensional models that did not include radiation effects and the present one. A second consideration is

39

that the time-scales for the flows near the accretion region are an order of magnitude faster than the orbital motion time scales, so that the exclusion of the orbital motion does not significantly impact on the accretion flow. The lack of orbital motion does prevent any possible formation of an accretion disk around the secondary since the angular momentum of the wind is ignored. In Chapter VII, we discuss some of the consequences brought on by the three-dimensional nature of the actual flows.

IV. GENERATING MODEL PARAMETERS

In the previous chapter, we outlined the modeling method to be used. The next step is to establish the parameters for our model binary systems. The parameters are selected to enforce self-consistency between the accretion rate and the desired model luminosity. To achieve this goal, we need to determine how the wind density and velocity vary at the orbit of the secondary with changes in the other system parameters.

We begin our analysis by deriving a relationship for the luminosity as a function of the stellar wind density and velocity. Let us again take the wind velocity to be given by Eq. 3.5 as

$$v = v_\infty (1 - R_0/r)^{\frac{1}{2}} . \qquad (4.1)$$

We also adopt the results of Zel'dovich and Shakura (1969), Shakura and Sunyaev (1973), and Alme and Wilson (1973) and assume that the gravitational potential energy released by the infalling matter is equivalent to 10% of the matter's rest mass energy. The luminosity in terms of the accretion rate is then given by

$$L_x = 0.1 \, dM_x/dt \, c^2 . \qquad (4.2)$$

Since the secondary's accretion rate is given from Eq. 2.5 as

$$dM_x/dt = \pi \, R_a^2 \, \rho_x \, v_x \, \alpha , \qquad (4.3)$$

we find the luminosity to be

$$L_x = 0.1 \, \pi \, R_a^2 \, \rho_x \, v_x \, \alpha \, c^2 , \qquad (4.4)$$

where ρ_x and v_x are, respectively, the unperturbed wind density and velocity at the orbit of the secondary. We can now use Eq. 2.4 to specify the accretion radius of the secondary:

$$R_a = 2 \, G \, M_x \, v_x^{-2} \; . \tag{4.5}$$

Substituting Eq. 4.5 into Eq. 4.4 we arrive at the desired equation giving the luminosity as a function of the wind density, wind velocity, accretion efficiency, and the mass of the secondary:

$$L_x = 0.4 \, \pi \, \alpha \, \rho_x \, (cGM_x)^2 \, v_x^{-3} \; . \tag{4.6}$$

Equation 4.6 points out the strong dependence of the X-ray luminosity on the mass of the secondary and the velocity of the wind.

The accretion rates found in the models are compared to those predicted by Eq. 4.3. This defines a ratio between the predicted accretion rate and the resulting rate. The accretion efficiency in Eq. 4.3 is initially estimated from Hunt's (1971) work.

We can estimate the variation in the wind density and velocity with the binary system parameters. To do this, we assume that the wind is unperturbed as it passes the secondary and that the X-ray luminosity is held constant. We also assume that the primary's mass loss rate is constant. This gives the density in the wind as a function of the distance from the primary as

$$\rho = \frac{dM_0/dt}{4 \, \pi \, r^2 \, v} \; . \tag{4.7}$$

We now substitute Eq. 4.1 into Eq. 4.7 and take r to be the binary separation. This gives us the wind density at the orbit of the secondary as a function of the primary's mass loss rate and the terminal wind velocity:

$$\rho_x = \frac{dM_0/dt}{4\pi a^2 v_\infty (1 - R_0/a)^{\frac{1}{2}}} \; . \tag{4.8}$$

In our later discussions, it will prove useful to have an expression for ξ as a function of distance from the primary and secondary. From Eq. 3.10 we have

$$\xi = \rho \, r_x^2 \, / \, L_x \, .\tag{4.9}$$

We can now incorporate Eqs. 4.1 and 4.7 into Eq. 4.9 to obtain

$$\xi = \frac{dM_0/dt \; r_x^2}{4 \, \pi \, r_0^2 \, L_x \, v_\infty \, (1-R_0/r_0)^{1/2}} \, ,\tag{4.10}$$

where r_0 is the distance from the primary.

One of the more critical determinations to be made is the primary mass loss rate needed to support the secondary's required accretion rate. We derive this from Eq. 4.8 using Eqs. 4.3 and 4.5. This yields

$$dM_0/dt = \frac{dM_x/dt \; v_\infty^4 \; (a-R_0)^2}{\alpha \; (GM_x)^2} \, .\tag{4.11}$$

And lastly the wind initiation radius as a function of the terminal wind velocity, the primary's mass loss rate, and the secondary's accretion rate are found from Eq. 4.11 as

$$R_0 = a - (GM_x/v_\infty^2) \; (\alpha \; dM_0/dt \; / \; dM_x/dt))^{1/2} \, .\tag{4.12}$$

Equations 4.11 and 4.12 determine our model parameters for they include the major variables describing a binary system.

In establishing our model parameters, we desire reasonably close agreement with the observed systems. However, our self-consistency constraint may require some adjustment of the model parameters away from their observed values. The three system parameters with the highest observational uncertainty are the most reasonable choices.

They are dM_0/dt (or equivalently, L_0), R_0, and v_∞. To a lesser extent, M_x could be varied, but observations place tighter constraints on it. R_0 and v_∞ both affect the wind velocity through Eq. 4.1, and the sensitivity of the X-ray luminosity to the wind velocity is plainly evident from Eq. 4.6.

In addition to observational constrains, there are theoretical limitations to be considered in parameter selection. R_0 has limits imposed on it by the theory of Castor, Abbott and Klein (1975). The initiation radius is essentially the photospheric radius of the primary, although it may be as much as 25% greater.

Constraints are also set on acceptable values of the primary's mass loss rate from energy and momentum arguments (for review, see Cassinelli 1979). First, assume that a photon is emitted in the photosphere of the primary with a frequency larger than some strong line. If the atmosphere is expanding radially outward and accelerating, then it may eventually reach a velocity at which the photon is Doppler shifted into resonance with the line. This velocity is given by

$$v = c(\nu-\nu_0)/\nu_0 \; , \tag{4.13}$$

where ν_0 is the line central frequency. For a single line, we can equate the final mass momentum flux, $v_\infty \, dM_0/dt$, to the photon momentum that is transferred by scattering all the radiation between ν_0 and ν_0 plus $\nu_0 v_\infty/c$. This gives us

$$v_\infty \, dM_0/dt = L\nu_0 v_\infty/c^2 \; . \tag{4.14}$$

If the entire spectrum is covered by non-overlapping lines such that

each adjacent line is seperated by a displacement corresponding to the Doppler shift at v_∞, the maximum mass loss rate can be related to the total momentum flux of the luminosity giving

$$(dM_0/dt)_{max} = L/v_\infty c . \qquad (4.15)$$

Note that the kinetic energy of the mass loss is given by

$$\tfrac{1}{2} dM_0/dt \ v_\infty^2 = \tfrac{1}{2} L \ v_\infty c^{-1} . \qquad (4.16)$$

Typical values of v_∞ are $1\text{-}2\text{x}10^3 \text{km sec}^{-1}$, so the mass loss carries away about 0.5% of the radiative luminosity of the star. Castor (see reference in Casinelli 1979) has shown that if multiple scattering of the photons occurs, the mass loss given by Eq. 4.15 will be raised by not more than a factor of two or three.

A model is generated by starting with the observed values for the parameters of the desired binary system. Using these values, we then calculate the required accretion rate using Eq. 4.2. Equation 4.11 is then used to calculate the required mass loss rate from the primary. This is checked against the maximum rate given by Eq. 4.15 to determine its acceptability. If the required value is not acceptable, one or more of the parameters are adjusted and the above process is repeated until we arrive at an acceptable value for the mass loss rate. At this point, the resulting set of parameter values gives us our desired self-consistent model.

V. MODEL ONE

The primary purpose of Model 1 is to provide a link between the two-dimensional hydrodynamic studies of the past and the hydrodynamics with radiation and wind ionization effects of Model 3. Thus, Model 1 does not account for X-ray ionization effects on the wind force. It does, however, include the X-ray heating and wind force models discussed in Chapter III. Modification of the wind force due to X-ray ionization will be left for Model 3.

A. Initializing Model 1

As a basis for Model 1, we select Vela X-1 (4U0900-40). This system is commonly assumed to be powered predominantly by wind accretion (Petterson 1978). It also has one of the largest X-ray binary separations known. The large separation serves both as a dominant factor in determining the mode of powering the system and as an aid in establishing our model. The zoning scheme for Model 1 does not provide sufficient spatial resolution to accurately represent the strong wind acceleration near the primary. Yet at the same time, we require a large area about the secondary in order to minimize boundary effects. The Vela X-1 system is best suited to the satisfaction of these conditions.

The model parameters for this system (and the 4U1700-37 system of Model 3) are adjusted to be in reasonable agreement with the observations reported by Avni and Bahcall 1975; Becker, et al 1978; Greenstein and McClintock 1976; McClintock, et al 1976; Petterson 1978; Pravdo, et al 1976; Rappaport, Joss and McClintock 1976;

46

Bahcall 1978; Hutchings 1974; and Ulmer, et al 1972 (re. Table 2.1). At the same time, we also seek to achieve the desired self-consistency between the accretion rate and the luminosity.

In Chapter IV, we presented the tools required to generate the model parameters. For Model 1, we begin with the observed luminosity of 10^{37} erg sec^{-1}. Since we have the luminosity given in terms of the accretion rate by Eq. 4.2, it is a simple matter to rewrite it in a form giving the accretion rate in terms of the desired luminosity:

$$dM_x/dt = 10 \, L_x/c^2 \, . \qquad (5.1)$$

For the observed luminosity, Eq. 5.1 yields a required accretion rate of 1.1×10^{17} g sec^{-1}.

In order to estimate the accretion efficiency, we note that far from the X-ray source the gas can be expected to be highly supersonic, while closer in it may become subsonic. For the purposes of Model 1, we fix α at 0.75, which corresponds to a flow of Mach 2 and is the median value of α between subsonic and highly supersonic flow. Later analysis of the flow will show that this is a reasonable value.

Referring back to Table 2.1, we see that the wind velocity at infinity is 1430 km sec^{-1}, the luminosity of the primary is 1.5×10^{39} ergs sec^{-1}, the binary separation is 52 R_θ, and the radius of the primary is 33 R_θ. Now, the required primary mass loss rate is given by Eq. 4.11 as

$$dM_0/dt = \frac{dM_x/dt \, v_\infty^4 \, (a-R_0)^2}{\alpha \, (GM_x)^2} \, . \qquad (5.2)$$

With the values cited this yields

$$dM_0/dt = 2.49 \times 10^{-5} \ M_\Theta \ yr^{-1} \ . \qquad (5.3)$$

To check the feasibility of this value, we recall that Eq. 4.16 and the discussion of Chapter IV set an upper limit on the mass loss rate of

$$(dM_0/dt)_{max} \simeq 3 \ L/v_\infty c \ . \qquad (5.4)$$

Based on the parameters for the Vela X-1 primary, Eq. 5.4 gives an upper limit of

$$(dM_0/dt)_{max} = 1.66 \times 10^{-5} \ M_\Theta \ yr^{-1} \ . \qquad (5.5)$$

Hence, our required mass loss rate based initially on the observed parameters is larger than the theoretical maximum by a factor of 1.48. We elected to use this value and not pursue parameter modifications further. The model parameters are summarized in Table 5.1. Note that the mass loss rate is a factor of 1.78 higher than the upper limits set by the observations of Hutchings (1976).

We use these values for several reasons. First, a 48% increase in the luminosity of the primary could account for the additional mass loss required. The primary mass loss rate was also designated as one of the primary candidates for modification if changes were necessary. Second, due to the close initial match, we feel it more advisable to leave the majority of the parameters at their accepted values rather than modify them further. Third, we are artificially forcing the luminosity to be sustained at its observed maximum. Model 1 is not expected to show any fluctuation in its accretion rates or X-ray luminosity. Sustaining the maximum luminosity

TABLE 5.1. Parameters for Model 1

Base System: 4U0900-40 (Vela X-1)

	Observed	Model
a (R_Θ)	52	52
R_o(R_Θ)	33	33
v_∞ (km sec^{-1})	1430	1430
M_x (M_Θ)	2	2
L_x (ergs sec^{-1})	1×10^{37}	1×10^{37}
L_o (ergs sec^{-1})	1.5×10^{39}	2.2×10^{39}
dM_o/dt (M_Θ yr^{-1})	$3.5-14.0\times10^{-6}$	2.4886×10^{-5}
α	---	0.75

Table 5.1. The parameters used for Model 1 are summarized here. The observed values are taken from Table 2.1. Note that the only difference in the model parameters is the value selected for the primary's luminosity. The selection of this value is discussed in the text.

therefore provides for the largest possible X-ray heating impact, and avoids the selection of some other arbitrary value.

We initialize the model by first establishing within the problem mesh an unperturbed wind flow with velocities given by Eq. 4.1 as

$$v = v_\infty (1 - R_0/r_0)^{\frac{1}{2}} , \qquad (5.6)$$

and densities given from Eq. 4.7 as

$$\rho = \frac{dM_0/dt}{4 \pi r_0^2 v_x} . \qquad (5.7)$$

The X-ray luminosity is fixed at the observed value. Equations 3.10, 17, and 18 are then used to set the material in each cell to its steady state state temperature.

We can now examine the conditions within the initialized flow. Equation 2.4 for the accretion radius was

$$R_a = 2 G M v_x^{-2} . \qquad (5.8)$$

Using the parameters for Model 1, Eq. 5.8 yields

$$R_a = 7.09 \times 10^{10} cm. \qquad (5.9)$$

At any given point in the wind, we can calculate the local sound speed and compare it with the local wind velocity. We find that at one R_a the flow is subsonic with a Mach number of about 0.87. At the maximum distance (8 R_a) from the secondary perpendicular to the line-of-centers, we find the flow to be highly supersonic with a Mach number of 24. The flow first changes from subsonic to supersonic at a distance of about 1.4 R_a. This is in agreement with our initial arguments on the selection of 0.75 as the accretion efficiency, although it is still apparent that this value is somewhat arbitrary.

The model is then followed in time until material has flowed completely through the spatial mesh several times. We note that no major changes occur in the characteristics of the flow after this time. The flow settles into a quasi-steady state such that only very slight fluctuations, on the order of 0.1%, are evident in the accretion rate and luminosity. At this point the calculation is terminated.

B. Calculation Results

Upon re-examining the conditions within the gas, we find that the supersonic region of the flow has moved inwards toward the secondary. The flow remains highly supersonic, nearly Mach 4.6, along the line-of-centers up to a point 5×10^9 cm from the secondary. To the sides of the secondary, the flow stays supersonic within R_a. However, to the rear of the secondary, in the region of the wake, the flow is highly subsonic. This behavior is related to the temperature structure of the gas as presented later in this chapter. The flow becomes more supersonic than the initial state indicated. This should have resulted in a higher accretion ratio since the efficiency increases with the Mach number. However, we find that the accretion ratio actually decreases.

In Chapter IV, we noted that Eq. 4.3 can be used to define an accretion ratio. This ratio, represented by β, is given by

$$\beta = \frac{dM_x/dt}{\pi R_a^2 \, \rho_x \, v_x \, \alpha} \, . \qquad (5.10)$$

The final values for the luminosity and the accretion ratio reached

51

by Model 1 are

$$L_x = 5.21 \times 10^{36} \text{ erg sec}^{-1} \, ,$$

and

$$\beta = 0.523 \, .$$

These results are a factor of 2 lower than those expected for gravitational accretion from a planar flow as predicted by the line accretion model.

We attribute the lower efficiency to the fact that the wind force is allowed to operate unaffected by the X-rays. It is therefore providing an additional force acting to blow the wind away from the secondary. This force is not included in the line accretion model. To see this, let us consider the force acting on the wind along the line-of-centers at some distance r, which is greater than a. The expression for the force is then

$$F = \tfrac{1}{2} v_\infty^2 R_0/r^2 - GM_x/r_x^2 \, . \tag{5.11}$$

Equation 5.11 goes to zero at a distance of 3.8×10^{11} cm from the secondary. This is about 5.4 R_a. The wind force is greater than the secondary's gravitational force farther out. Off the line of centers, the wind force accelerates the flow outwards, providing an acceleration component not present in the planar flow of the line accretion model. Thus, it appears that the wind force significantly affects the accretion flow in this model.

We have produced a series of figures which show contours of constant material density, energy density, temperature and ξ. There are several features in common among these figures. The scales show

distance from the secondary, with the location of the secondary marked by a small x. In all cases, the wind material is flowing in from the right and exiting to the left, corresponding to the primary lying off the right side of the figure. The phenomena occurring near the upper and lower edges of the figures are boundary effects. These are the result of the spatial mesh being too small. The side boundaries are not able to supply material fast enough as the flow is drawn in by the secondary's gravity. Hence, these regions become artificially rarified. This has no effect on the model since the regions are still well outside the main accretion flows.

Figure 5.1 shows contours of constant material density. The phenomenon occuring immediately to the right of the secondary is the result of a thermal instability in the wind flow. To get at the nature of this instability, we first note that the energy contours (Fig. 5.2) are very smooth except near the wake region to the left of the secondary. Since the energy density is directly proportional to the pressure, the smooth contours indicate that the temperature and density are varying in a manner which maintains a constant pressure. The fluctuations are wildly evident in Fig. 5.1, but are not as clear in the temperature contours of Fig. 5.3. This is due to the small variation in density over the mesh, as compared with a large variation in temperature.

McCray and Hatchett (1975) demonstrated that a gas exposed to X-ray heating would exhibit multiple density-temperature states. A gas under these conditions can change states discontinuously
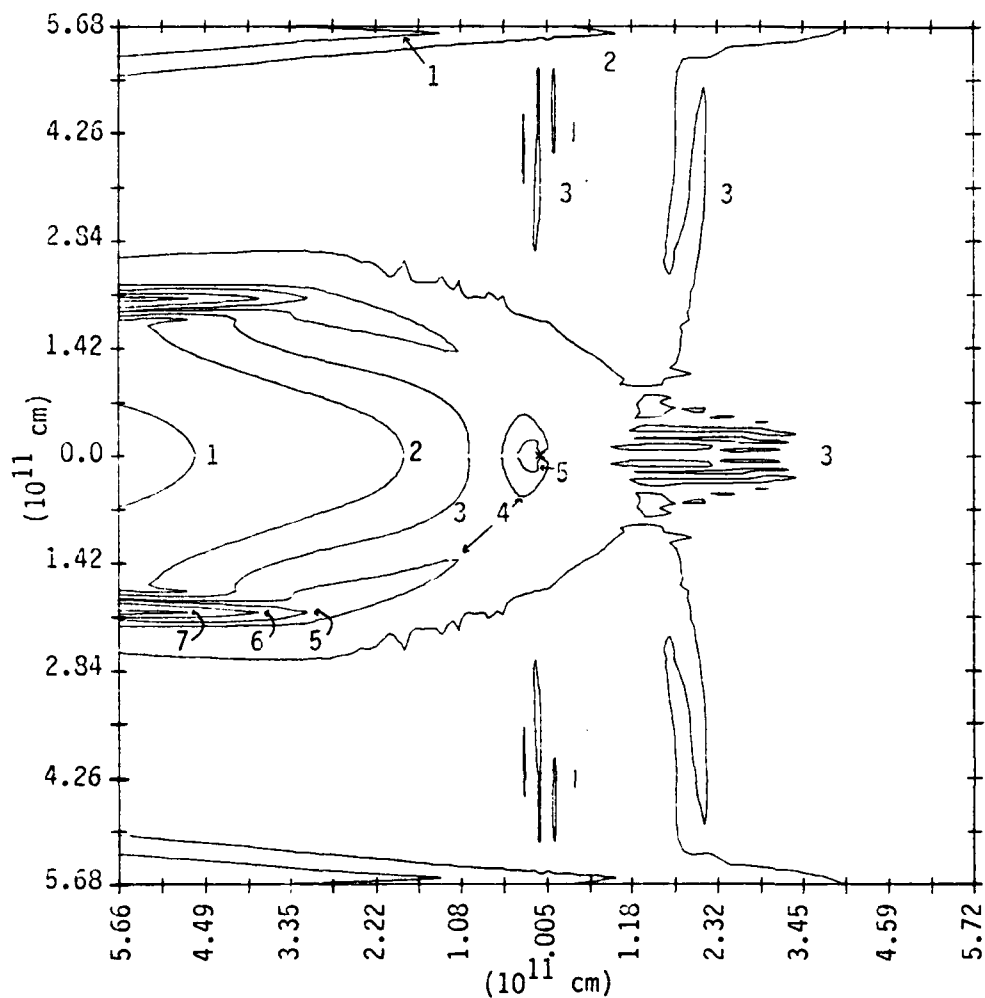
Figure 5.1. Material Density Contours for Model 1. In this and all other contour plots, we have the secondary located at the small x near the center of the figure. The primary lies off the right side of the plot, which is taken as the "front" of the secondary. The material flow is thus from right to left through the plot. In front of the secondary lies a region of thermal instability as described in the text. The densely packed contours are at level 3. The contours near the top and bottom of the frame are the result of boundary effects in the simulation. The contour values in 10^{-13} g cm^{-3} are: (1) 0.5; (2) 1.0; (3) 1.6; (4) 2.6; (5) 4.1; (6) 6.6; (7) 10.0.
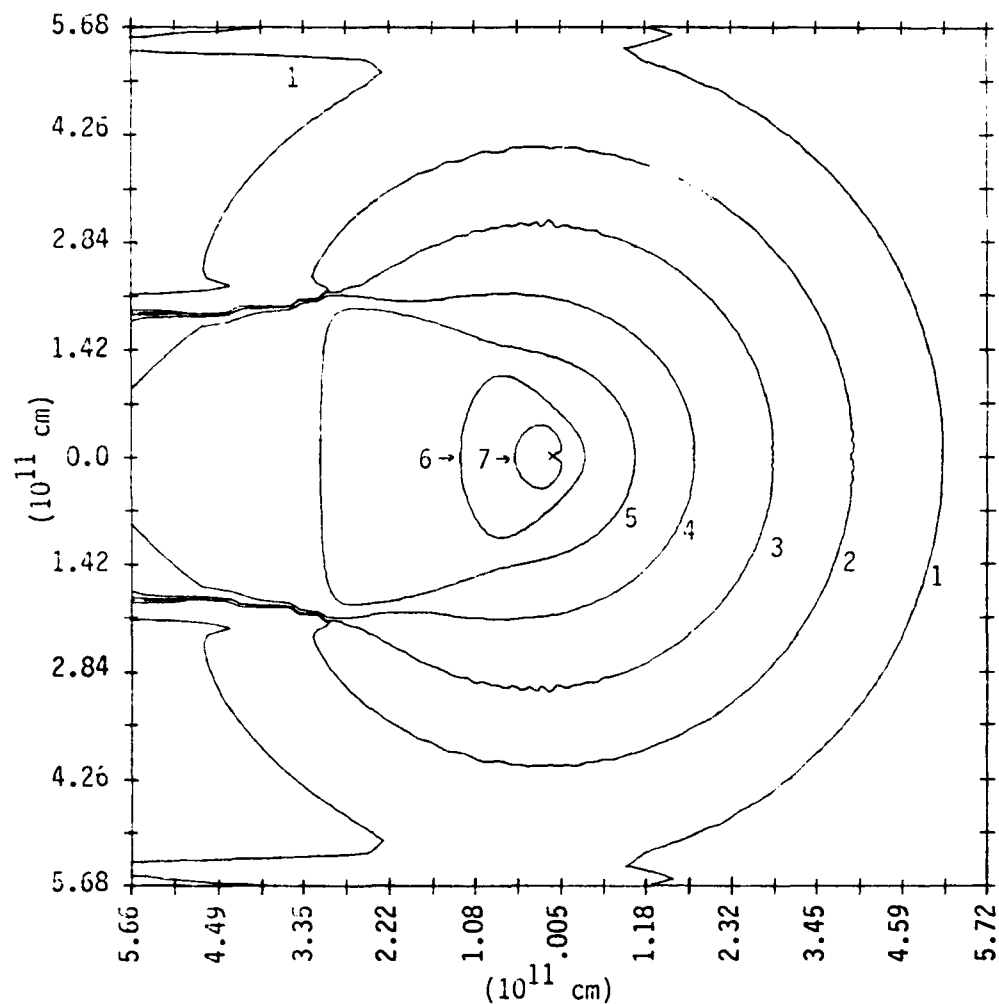
Figure 5.2. Energy Density Contours for Model 1. This figure can also be used to give the pressure of the gas through the use of Eq. 5.12. The opening of Contour 1 near the top and bottom is the result of boundary effects in the simulation. The contour values in ergs cm^{-3} are: (1) 3.; (2) 9.; (3) 27.; (4) 81.; (5) 243.; (6) 729.; (7) 2187.
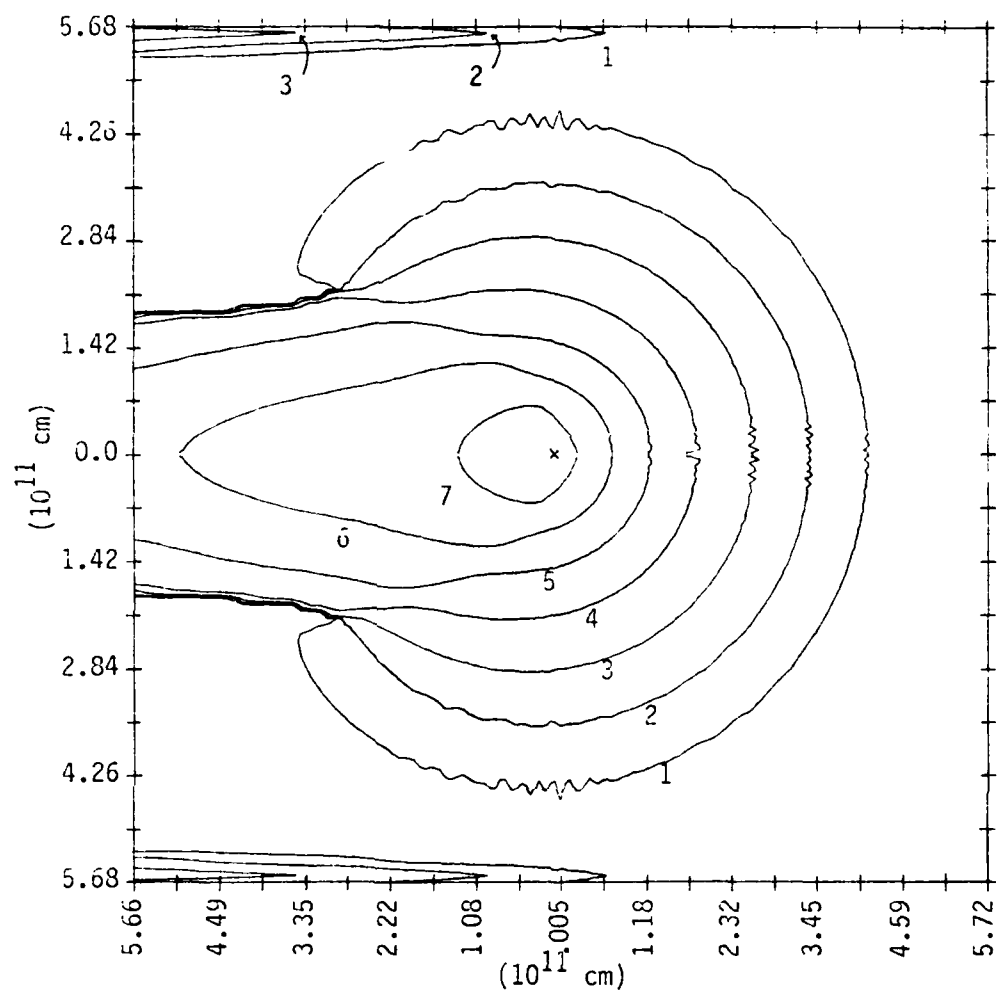
Figure 5.3. Temperature Contours for Model 1. This plot clearly shows the formation of a hot wake behind the secondary. Its regions of instability are not as evident in this figure as in Fig. 5.1 because of the much larger variation in temperatures. Contours along the upper and lower edges are the result of boundary effects in the simulation. The contour values in keV are: (1) 0.020; (2) 0.045; (3) 0.100; (4) 0.224; (5) 0.500; (6) 1.110; (7) 2.500.

depending on its current state and previous history. In particular, hot gases undergoing cooling may jump from a thin, high temperature state to a dense, low temperature state, while staying at constant pressure. Conversely, a cool gas heating may undergo an opposite transition.

Following their work, we have produced a plot of P/F versus ρ/F for each cell of the problem, where F, the X-ray flux, is given by

$$F = \frac{L_x}{4 \pi r_x^2} , \qquad (5.12)$$

and P, the gas pressure, is given in terms of the energy density of the gas by

$$P = E(\gamma-1) . \qquad (5.13)$$

Figure 5.4 clearly demonstrates the behavior predicted by McCray and Hatchett. Two different populations of gas are evident. The upper portion of the curve corresponds to hot gas which is moving away from the secondary and beginning to cool. The lower portion shows cool gas which is being heated as it approaches the secondary. The sharp corner in the lower right area of the curve is an artifact of the match between Eqs. 3.20 and 3.21 that were used to fit the steady state temperature curve. The gas attempts to change states erratically in the central region of the plot. Lines of constant temperature drawn through the plot serve as references for the multi-valued region between ρ/F = 10^{-25} and 10^{-26}. The broken contours in front (to the right) of the secondary in Fig. 5.3 represent gas which falls into this region of the curve. As a final
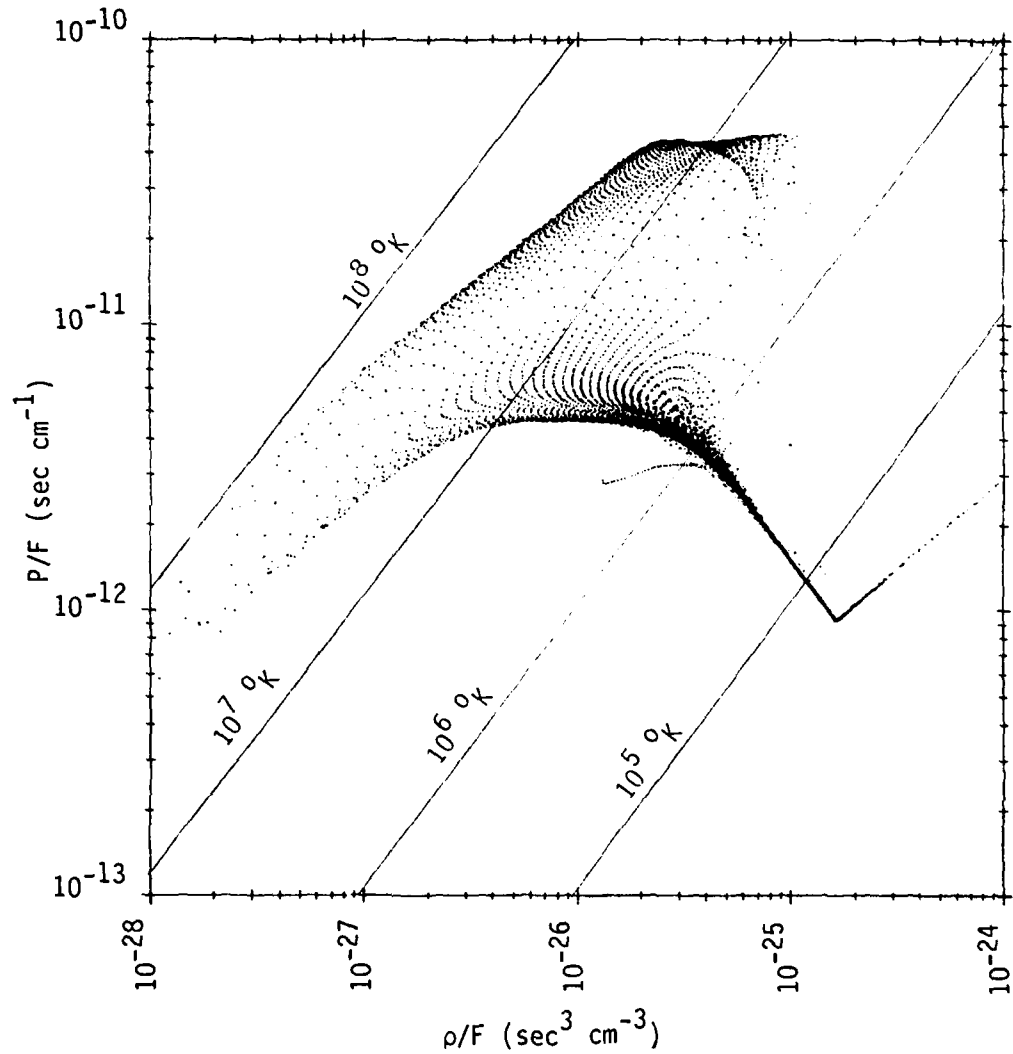
Figure 5.4. P/F vs ρ/F for Model 1. This figure demonstrates the multivaluedness of the pressure-temperature states of the gas as it is heated or cooled. Lines of constant temperature are displayed for reference. Gas progressing from left to right along the upper curve is undergoing cooling, while gas moving from right to left along the bottom is undergoing heating. This corresponds to hot gas cooling as it moves away from the secondary and cold gas heating as it approaches the secondary, respectively.

58

note, the small line dropping out of the lower portion of the curve is from the boundary region of the problem and is not physically real.

We do not believe that this instability is an artifact of our model alone. Prior to producing Model 1, we used the hydrodynamic portions of our code to repeat Hunt's (1971) problems for the Mach 1.4 and Mach 2.4 cases. Our results were in very good agreement with his, and the code did not show any of the instability behavior found in Model 1.

We have followed the values of material density, energy density and temperature in time within the instability region and find them to be very dynamic. Figure 5.5 displays these values at two different instances. Note that they are plotted as a function of zone rather than distance to help determine the source of the instability. We see that the density varies inversely with the temperature, and that the energy density remains relatively smooth. The onset of the instability occurs at about zone 96 and dies out at about zone 70. The variations propagate in a wave like motion from right to left. Since the secondary is located at zone 60, these variations have long since died out and fluctuations in accretion rate or luminosity never appear. We also see that the variations are spread out over several zones, so that the instability is not inherently numerical.

In 1977, Hatchett and McCray preformed detailed calculations on the transfer of X-rays through a stellar wind by assuming either a
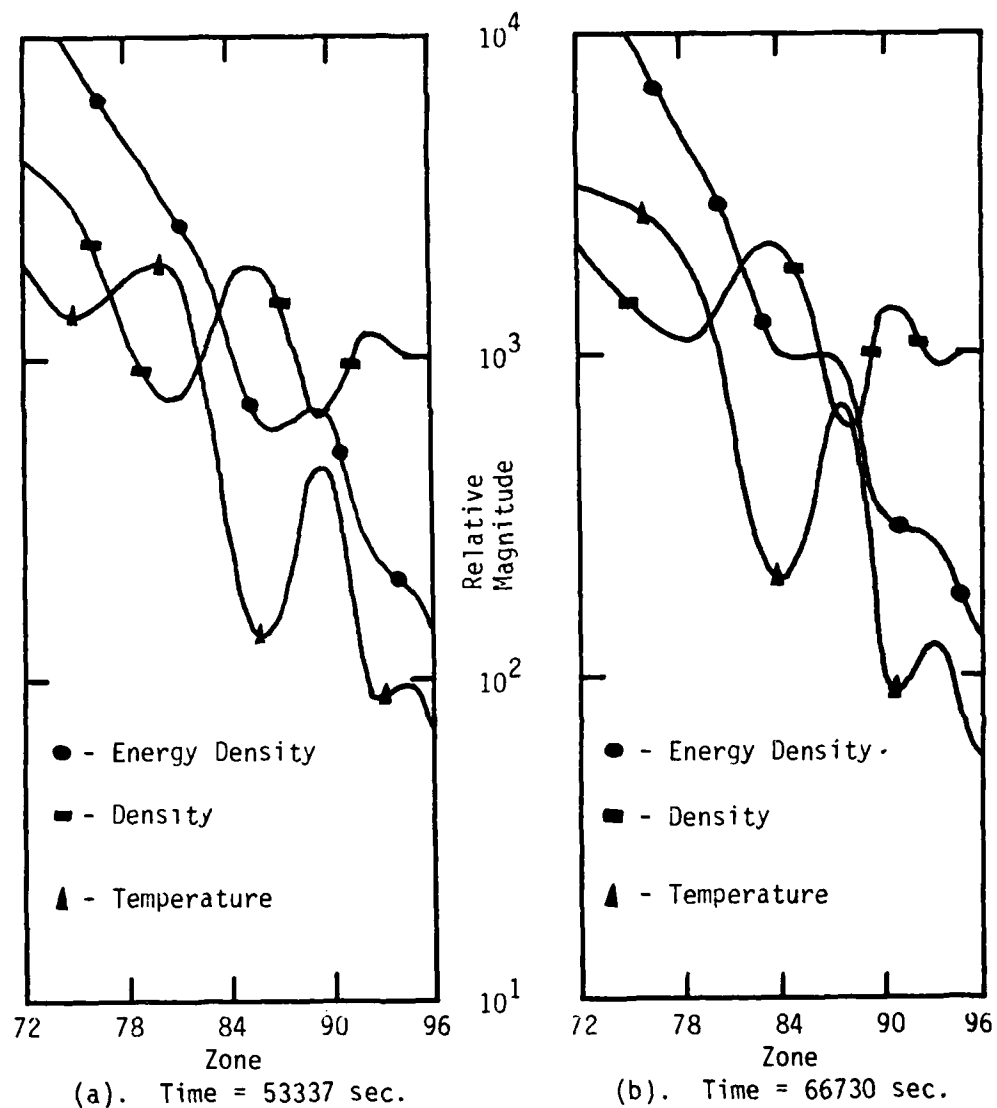
Figure 5.5. Material Density, Temperature, and Energy Density Values in the Instability Region. The density, temperature, and energy density are plotted as a function of zone along the line of centers through the region of instability. Plotted at two different times, the wave like progression from right to left can be seen. The minima and maxima propagate with the flow velocity.

constant wind velocity or a wind obeying Eq. 5.6, and determined contours of constant ionization plotted in terms of the parameter ξ. They found these contours to be roughly spherical, with their centers displaced from the source of the X-rays. For comparison, we have produced ξ contours as shown in Fig. 5.6. The shock severely distorts the trailing sections of these contours, showing the effects of including hydrodynamics. The right hand sections are very nearly spherical, with the inner contours more closely centered about the secondary than the outer ones. The scale of our model does not allow direct comparison with their results beyond the general agreement in the shape of the contours.

However, we can use Fig. 5.6 to measure the impact of the X-ray heating on the flow. The ξ contours were selected such that the steady-state temperatures they give correspond to the values on the temperature contours of Fig. 5.3. By comparing the two plots, we find that as we approach the secondary, the actual temperatures are not reached until much closer in than their steady-state counterparts. This is an indication that the X-ray heating effects are dominated by the hydrodynamic flow.

We can examine the impact of the X-ray heating in another way. Let us compare the gravitational potential energy with the thermal energy of the gas. If the thermal energy rapidly approaches the gravitational energy, capture of the material becomes less possible. To compare the two energies, we require that
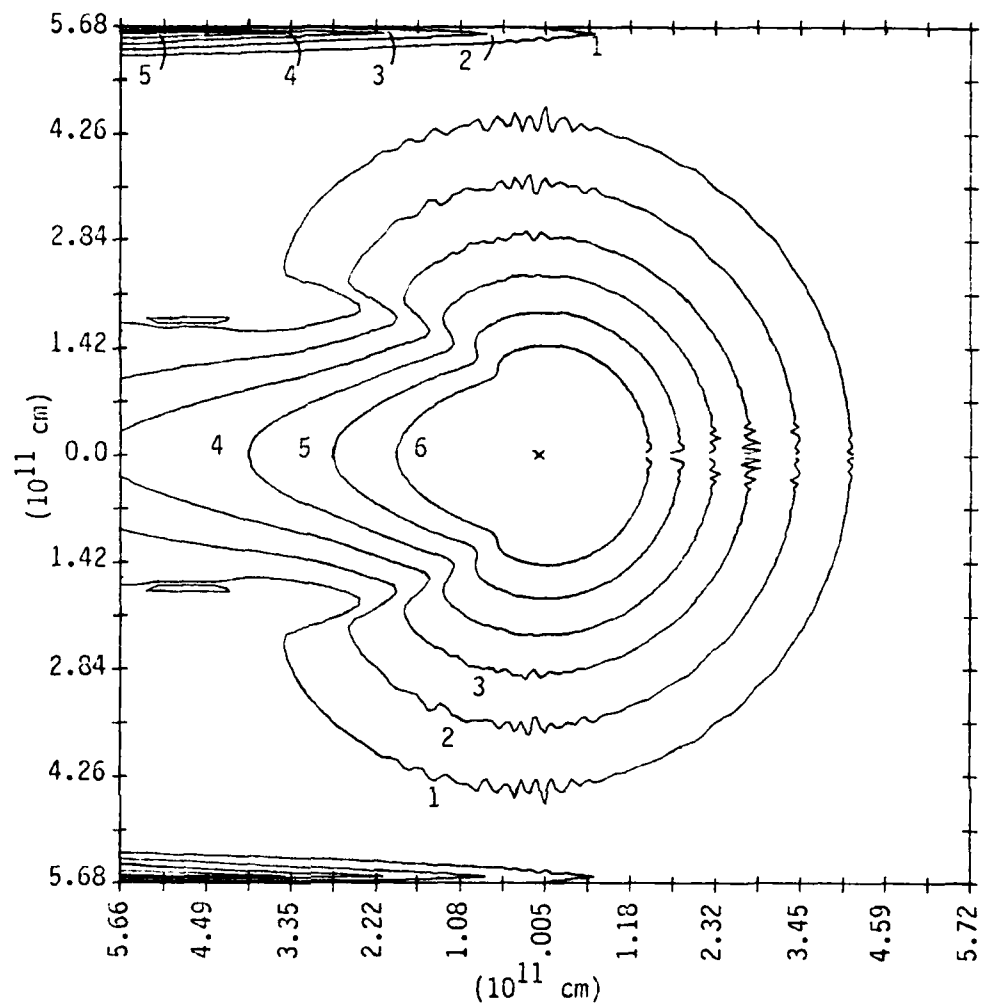
$$GM_x \rho / r = \rho C_v T .$$ (5.14)

Figure 5.6. ξ Contours for Model 1. The circular shapes of these contours outside of the wake region are similar to those found by Hatchett and McCray (1977). The location of the shock is best seen here where it lies along the dips in the contours just to the left of the secondary. The contours along the upper and lower edges of the plot are again the result of boundary effects. The contour values in units of 10^{-27} sec³ cm⁻³ are: (1) 5.7; (2) 3.6; (3) 2.5; (4) 1.7; (5) 1.1; (6) 0.67.

Thus, R_G for a given temperature is given by

$$R_G = GM_x/C_v T . \qquad (5.15)$$

At a temperature of 5 keV, $R_G = 2.41 \times 10^{10}$ cm, while at 1 keV, R_G is five times greater. Re-examining Fig. 5.3 shows that for the spherical regions to the right of the secondary, the 1.1 keV contour lies inside the 1 keV R_G, while the 2.5 keV contour lies inside the 5 kev R_G. The drawn out tails in the wake pass outside these radii. This behavior indicates that the flow is dominated by the hydrodynamics rather than the X-ray heating in the region between the primary and the secondary. However, the X-ray heating begins to dominate in the trailing regions of the wake.

Let us consider the time it takes material to flow from R_G of 1 keV to 5 keV, and compare this to the time it would take to heat the gas from 1 keV to 5 keV over the same distances. We developed Eqs. 3.19 and 3.20 to give us the X-ray heating time. At 1 keV, we are in the Compton dominated heating region, so we can use Eq. 3.19 to estimate the heating time directly from the Compton time as:

$$t_x = \frac{4 \pi r^2 C_v T m_e}{L_x \kappa_e n} . \qquad (5.16)$$

Let us approximate the heating time by taking the average of the heating times found between R_G of 1 keV and 5 keV. Since at 5 keV, R_G is 2.41×10^{10} cm, we find from Eq. 5.16 that the average heating time is 1790 seconds.

The flow velocity along the line of centers is about 950 km sec^{-1}. The distance between R_G of 1 keV and 5 keV is 9.64×10^{10} cm.

63

Thus the flow crosses this distance in 1014 seconds. Along the line of centers at least, the hydrodynamics time scale is shorter than the heating time by a factor of 1.8. If the distance the flow must cover increases, by say, curving in around behind the secondary, the flow time will increase and quickly become comparable with the heating time. When this occurs, the gas will be able to heat at the same rate it is losing gravitational potential energy and capture will become exceedingly difficult. From the temperature structure in the wake, we see that this is in fact what is happening.

The line accretion model pictures the bulk of the material being accreted along the line of centers from downwind of the secondary. The combination of the wind force and the X-ray heating are acting to reduce accretion from this region. To better appreciate the flow near the secondary, plots of the velocity field and mass-flux field are shown in Figs. 5.7 and 5.8. Both figures show a pronounced reduction in the flow to the left of the secondary, which corresponds to the downwind wake region. Figure 5.8 was created by plotting the momentum vectors multiplied by their distance from the axis. Since we are using cylindrical coordinates, this gives us the contribution to the flux integral at that particular distance. Vectors of constant length signify constant mass flux contributions to the accretion rate. In effect, we are looking at the amount of material entering each cylindrical shell about the secondary. Equal vectors imply that the same amount of material has entered a given shell. Thus low flux over a large area contributes as much material as a
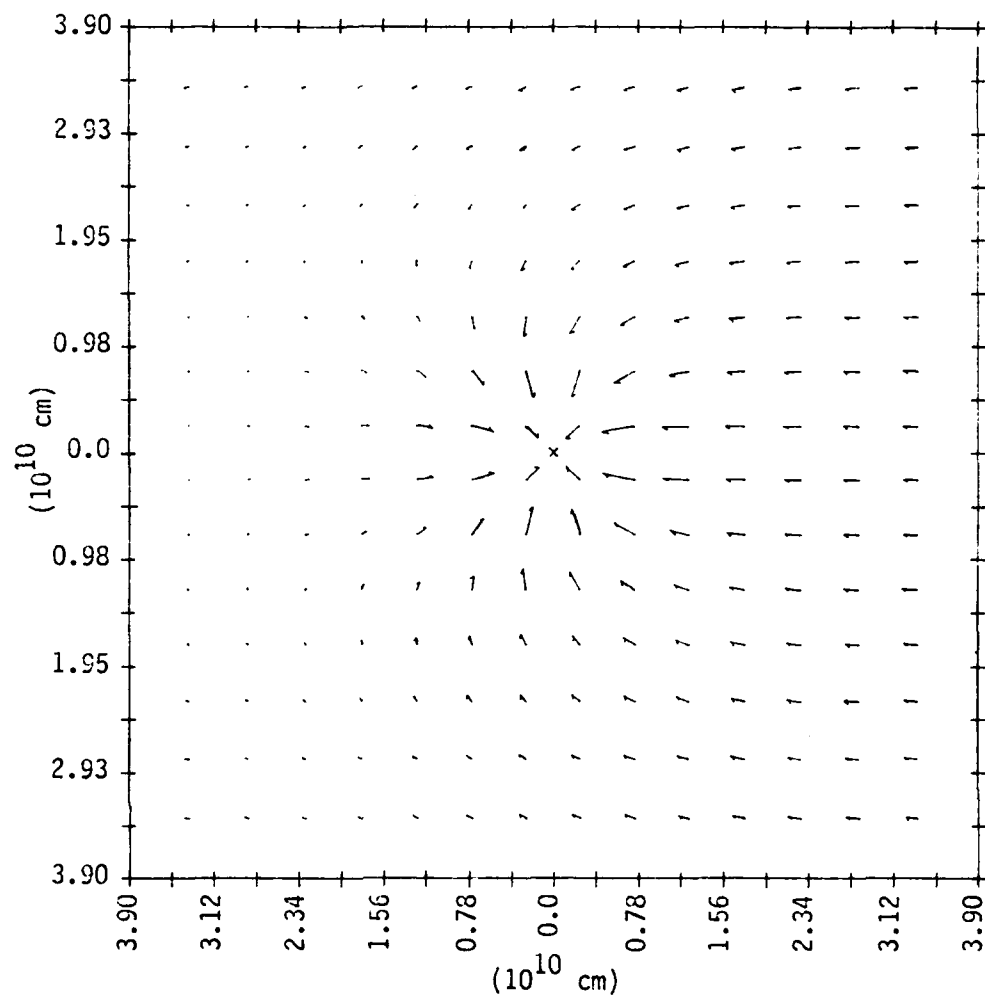
Figure 5.7. Velocity Field for Model 1. This is a plot of the material velocity near the central accreting region of the problem. The lengths are proportional to a maximum velocity of 2.894×10^8 cm sec^{-1}. The tail of each vector marks the point at which the velocity was taken. Note the formation of a stagnation region near the rear of the secondary.

3.90

2.93

1.95

0.98

$(10^{10}$ cm$)$

0.0

0.98

1.95

2.93

3.90

3.90 3.12 2.34 1.56 0.78 0.0 0.78 1.56 2.34 3.12 3.90
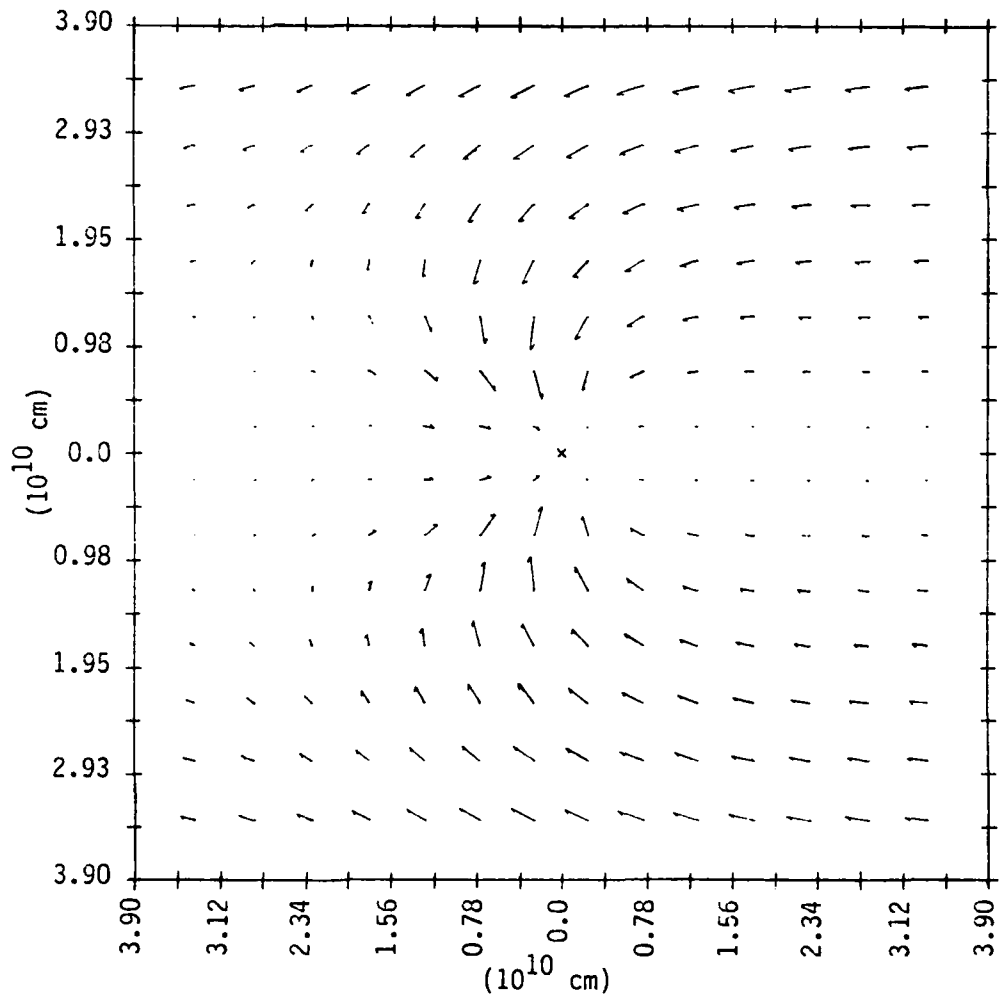
$(10^{10}$ cm$)$

Figure 5.8. Weighted Momentum Vectors for Model 1. This is a plot of weighted momentum vectors near the central accretion region of Model 1. The momentum density vectors are weighted by their distance off axis to highlight the accretion mass flow. Vectors of constant length imply constant mass flux. Note that the maximum amount of material captured is from the sides, rather than from the left. All vectors are scaled to a maximum vector of 8.68×10^5 g cm^{-1} sec^{-1}.

large flux over a small area. We note that most of the material is captured from the side, in contradiction with the line accretion model, but in agreement with the suspected behavior discussed above.

VI. MODEL TWO

In Chapter 5, we presented a model for which the stellar wind force and the X-ray heating combined to have a major effect on the accretion flow, but a relatively minor impact on the total accretion rate and resultant luminosity. We found that the X-ray heating effects were not strong enough to significantly modify the hydrodynamics of the flow. We showed that the temperatures reached by the gas were, for the most part, well below the corresponding steady state temperatures of the gas. We also found that the internal energy of the gas was below the gravitational energy of the gas.

A. X-ray Pre-heating Analysis

Alme and Wilson (1975) had previously found that material flow could be significantly affected if the X-ray heating was able to dominate the hydrodynamics of the flow. The same results were reached analytically by Carlberg (1978), and in one dimensional models of spherical accretion by Cowie, Ostriker and Stark (1978). In particular, if the X-ray heating raised the energy of the gas above its gravitational potential energy, the accretion flow was disrupted and the material was blown away from the secondary. We therefore decided to create a second model which would show the effects of X-ray heating much more strongly. The model would also correct the boundary problems which appeared in Model 1.

To get an idea of the parameters we need, we first reconsider the unperturbed initial state of Model 1 in terms of the steady state

temperatures and gravitational energies. The radius, R_G, at which the gravitational potential energy equals the thermal energy of a gas at some temperature, T, is given by Eq. 5.18 as

$$R_G = GM_x/C_vT \ .$$ (6.1)

Equation 4.9 can be rearranged to give the distance from the secondary, R_T, for which a ξ corresponding to a desired steady state temperature is reached:

$$R_T = (\xi L_x/ \ \rho)^{\frac{1}{2}} \ .$$ (6.2)

Using these two equations, we then plot the locations of the steady state temperatures and their corresponding gravitational potentials for temperatures of 1 keV and 5 keV. The results are shown in Fig. 6.1. We see that at 5 keV, R_T lies just outside the corresponding R_G, with R_T averaging 1.32 R_G. For the 1 keV case, we have R_T occuring much farther out then R_G, averaging 2.17 R_G.

Following the analysis presented in Chapter 5, we calculate the flow time and X-ray heating time for the initial conditions. We find that the flow time is 1125 seconds, while the X-ray heating time is 932 seconds. Since the final conditions of Model 1 have flow times less than the X-ray heating time, we desire to construct Model 2 such that the heating times dominate the flow times even after the problem has relaxed to a steady-state. There appears to be no forthright way of predicting the values, so we must create a rather extreme set of initial conditions.

To determine which way we need to vary the system parameters to reach the desired results, let us begin by considering again Eq. 3.19
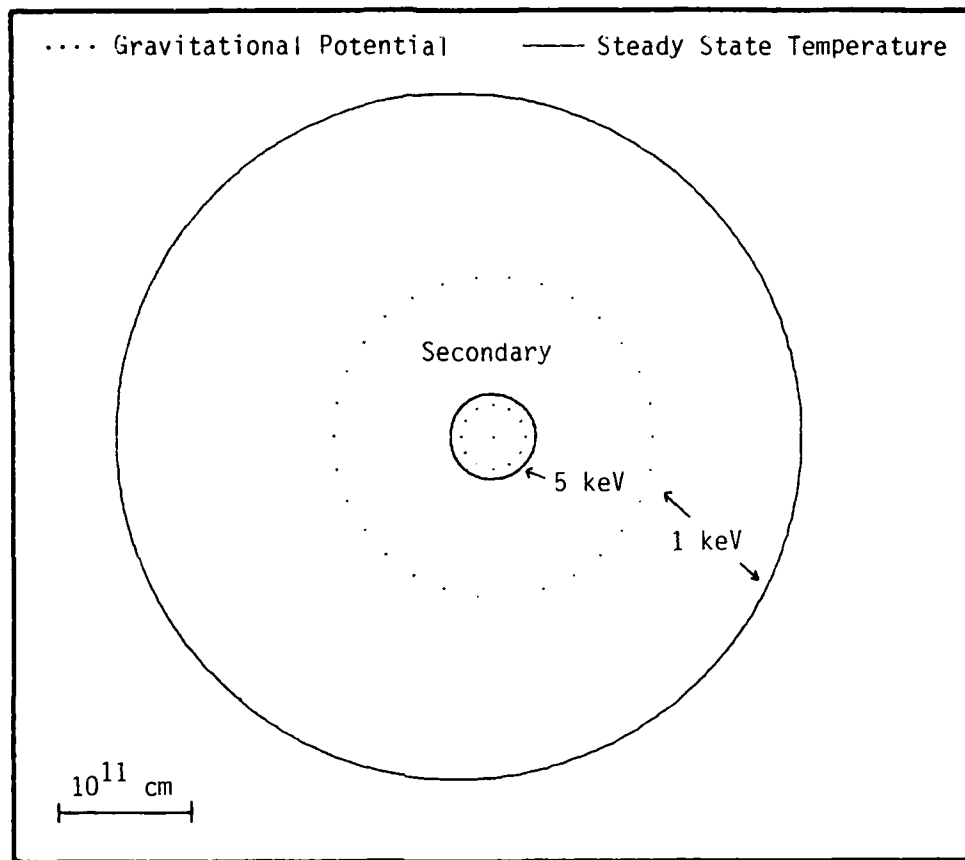
Figure 6.1. Initial Gravitational Potential and Steady State Temperature Contours for Model 1. Plotted here are the steady state temperature and gravitational potential contours for the unperturbed initialized state of Model 1. The contours were plotted at 1 and 5 keV. At 5 keV, R_T is 1.32 times R_G, while at 1 keV, R_T is 2.17 times R_G.

ng the X-ray heating time when in the Compton dominated regime:

$$t_x = \frac{4 \pi r^2 m_e C_v T}{L_x \kappa_e n} \, . \qquad (6.3)$$

most rapid way of decreasing the heating time is clearly to
ease the distance to the secondary. Since these distances are
g calculated for various values of the gravitational potential,
easing the mass of the secondary will have the desired effect.
naintain self-consistency, the wind velocity near the secondary
 have to decrease, the wind density will have to increase, or a
ination of both. At this point, the method developed in Chapter
 brought into full use.

Initializing Model 2

We can use the results of Model 1 to help establish the
neters. First, since the accretion ratio was 0.523, we use 0.392
the accretion efficiency rather than 0.75. We also use the X-ray
nosity from Model 1, 5.212×10^{36} ergs sec^{-1}, as the base
nosity. Recalling that the required accretion rate for a given
nosity is given by Eq. 5.1 as

$$dM_x/dt = 10 \, L_x/c^2, \qquad (6.4)$$

find that the desired luminosity requires an accretion rate of
1×10^{16} g sec^{-1}. We now need to compute the primary mass loss
with the aid of Eq. 4.11:

$$dM_0/dt = \frac{dM_x/dt \, v_\infty^4 \, (a-R_0)^2}{\alpha \, (GM_x)^2} \, . \qquad (6.5)$$

start with the parameters used in Model 1, and vary them until we

71

have a self-consistent system. The values as finally selected differ significantly from the observed values of the Vela X-1 system. They are summarized in Table 6.1.

Comparing dM_O/dt with the limit set by Eq. 5.5, we find that this mass loss rate is a factor of 4 below the maximum available to the primary, based on its luminosity from Table 1 of 1.5×10^{39} ergs sec^{-1}. We also note that the required primary mass loss rate lies in the middle of the range of probable values established by the observations of Hutchings (1976). In this case the match only demonstrates the reasonableness of the value since all of the other parameters differ from the observed. What we have established is an arbitrary, but self-consistent, set of parameters.

We now examine the characteristic time scales given by these parameters for a model initialized as in Chapter 5. That is, the wind is given a velocity structure according to Eq. 3.5 of

$$v = v_\infty (1 - R_0/r)^{\frac{1}{2}} . \qquad (6.6)$$

The secondary's gravity initially has no effect, and the gas temperatures are again set at the appropriate steady state temperatures. The wind velocity near the orbit of the secondary is 427 km sec^{-1}, and R_G at 5 keV (re. Eq. 6.1) is just one half that found for Model 1, or 1.2×10^{10} cm.

With the above values, we find that the time for the flow to cross from R_G at 1 keV to R_G at 5 keV is 1124 seconds. The average X-ray heating time computed from Eq. 6.3 is 44.35 seconds. The X-ray heating time is 25 times greater than the flow time, so in fact this

TABLE 6.1. Parameters for Model 2

Base System: 4U0900-40 (Vela X-1)

	Observed	Model
$a \ (R_\odot)$	52	60
$R_o(R_\odot)$	33	41.05
$v_\infty \ (km \ sec^{-1})$	1430	750
$M_x \ (M_\odot)$	2	1
$L_x \ (ergs \ sec^{-1})$	1×10^{37}	5.12×10^{37}
$L_o \ (ergs \ sec^{-1})$	1.5×10^{39}	3.8×10^{38}
$dM_o/dt \ (M_\odot \ yr^{-1})$	$3.5\text{-}14.0 \times 10^{-6}$	7.418×10^{-5}
α	---	0.4

Table 6.1. The parameters used for Model 2 are summarized here. The observed values are taken from Table 2.1. The values selected for the model differ greatly from the observed values. The reasons for this are discussed in the text.

model should be dominated by the X-ray heating rather than the hydrodynamics.

As one final preliminary analysis, we calculate the point at which the wind force dominates the secondary's gravity, along the line of centers, and in the region of the wake (re. Eq. 5.14). We find this point to be 6.13×10^{11} cm from the secondary, which is about 4.1 R_a. This distance is greater than that found in Model 1, but is closer in terms of R_a. Considering the increased scale of Model 2, the wind force will be active over a much larger region of the wake.

Figure 6.2 shows a plot of the steady state temperatures and the gravitational potentials at the 1 and 5 keV level. We find that at 5 keV, the steady state contour is pushed to 3 R_G, while at 1 keV, the contour is out to 4.6 R_G. Thus, the initial state configuration is significantly different from that seen in Model 1.

On examining the velocity structure of the intial state we find it to be supersonic inside the accretion radius, where the accretion radius for this model is 1.488×10^{11} cm or nearly a factor of two larger than Model 1. The flow reaches Mach 2 at 1.03 R_a, and is Mach 28.1 at the outer side boundary which is 53 R_a. The velocity structure is thus similar to that seen in Model 1.

C. Calculation Results

Model 2 is turned on and followed in time until it too reaches a quasi-steady state. The basic results confirm our suspicions that the X-rays have a much larger effect than they did in Model 1. For the luminosity and the accretion ratio we have
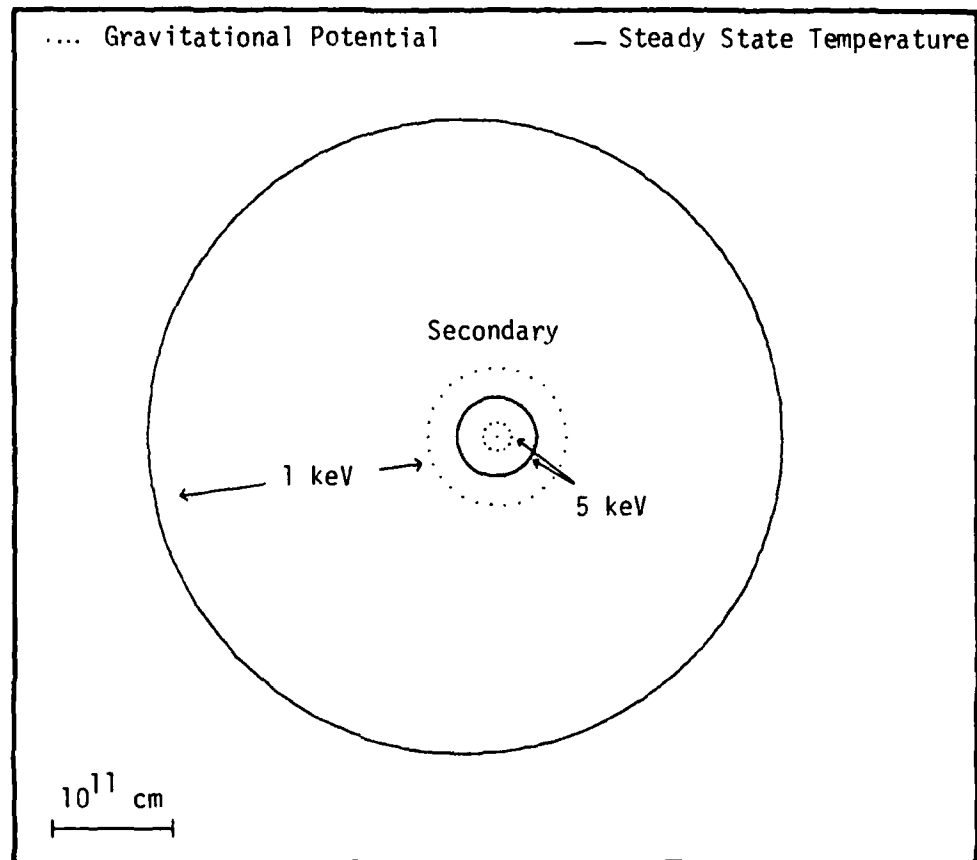
Figure 6.2. Initial Gravitational Potential and Steady State Temperature Contours for Model 2. Shown here are the steady state temperature and gravitational potential contours for the unperturbed initialized state of Model 2. For this model at 5 keV, R_T is 3 times R_G, while at 1 keV, R_T is 4.6 times R_G.

$$L_x = 1.28 \times 10^{36} \text{ erg sec}^{-1} ,$$

$$\beta = 0.235 .$$

We note that these values are significantly lower than expected, this time dropping by a factor of 5.

With the interest of this model placed on the X-ray heating effects, let us first examine the temperature contours shown in Fig. 6.3, and the ξ contours of Fig. 6.4. We have again selected the values of the ξ contours such that the steady state temperatures they corresponded to matched the temperature contour values. We first notice that the fall off from the steady state levels to the actual levels are not nearly as drastic as seen in Model 1. When we compare the gravitational potentials with the temperature contours, we find that they essentially match up at the 2.048 keV level. X-ray heating is apparently still much faster than the hydrodynamic flow times. We also see that the boundary flow is better behaved, and that there is now an extended wake behind the secondary.

We recalculate the flow and heating times for Model 2 in its final state. The flow velocity between R_G of 1 keV to 5 keV averages 700 km sec^{-1}, giving a flow time of 686 seconds. The corresponding X-ray heating time calculated from Eq. 6.3 is found to be 181.72 seconds. Thus while the magnitude of the difference has dropped from that of the initial state, the X-ray heating time is still greater than the flow time by a factor of 3.8.

One effect of this high heating rate can be seen immediately in the temperature contours of Fig. 6.3. Extremely high temperatures
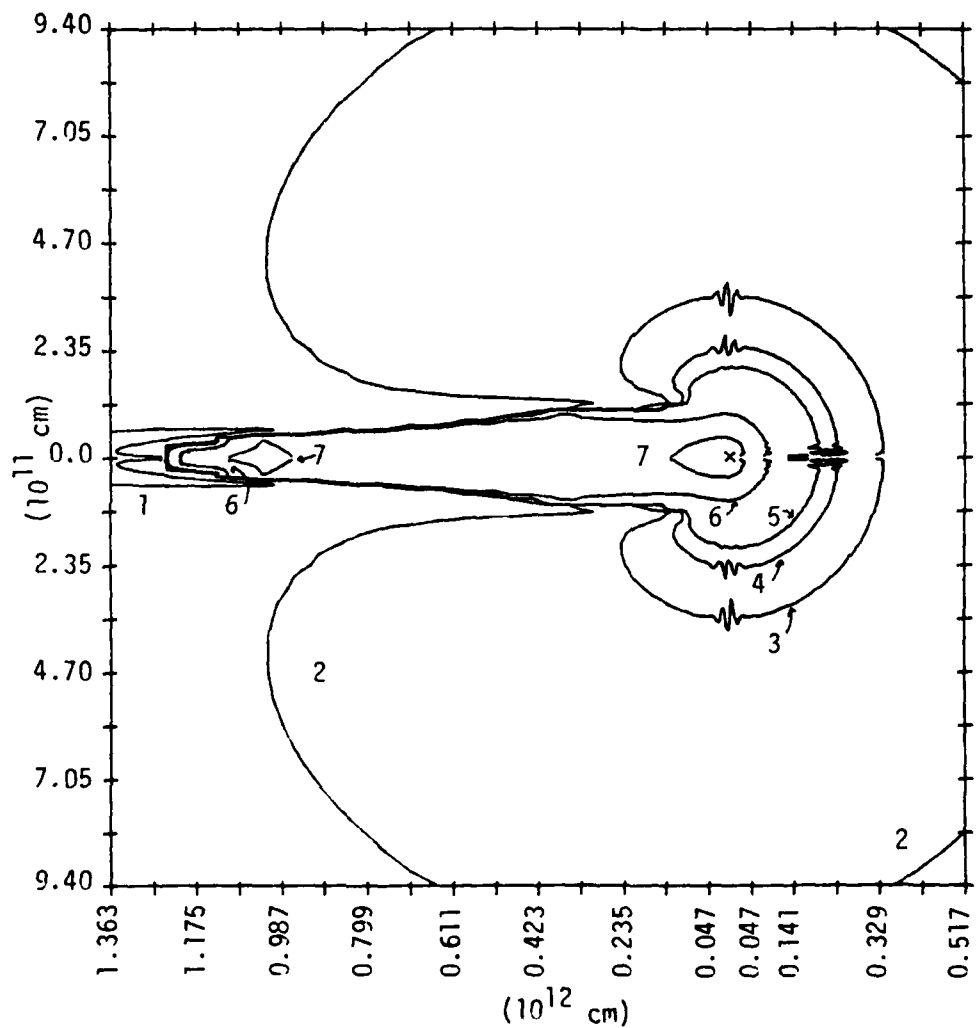
Figure 6.3. Temperature Contours for Model 2. As the Model 1 contour plots, material is flowing in from the right and exiting to the left. The secondary is marked by the small x. We note here the high temperatures reached at the tip of the wake where the thin gas finally mixes with the ambient material. The temperatures in keV are: (1) .0005; (2) 0.002; (3) 0.008; (4) 0.032; (5) 0.064; (6) 0.512; (7) 2.048.
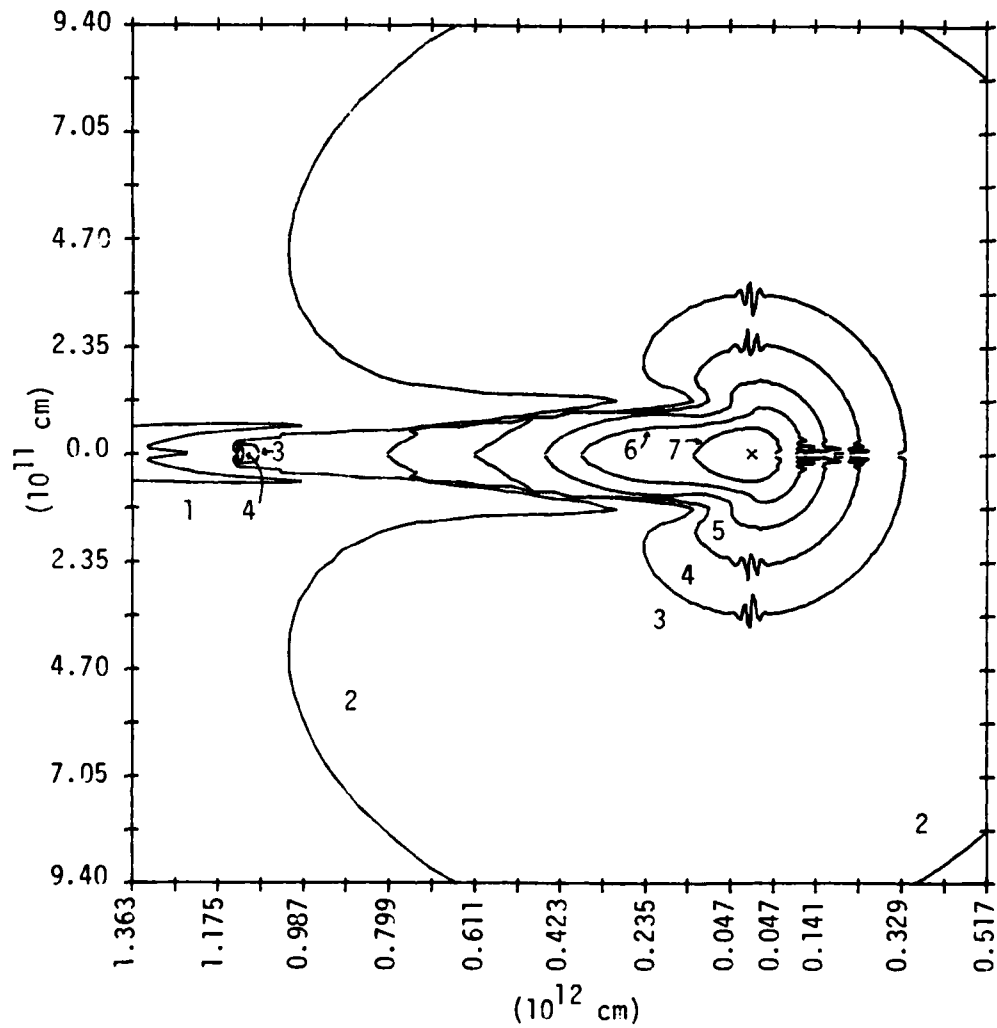
Figure 6.4. ξ Contours for Model 2. The ξ contour values were again selected to give steady state temperatures which correspond to the values of the temperature contours of Fig. 6.3. We find that the contours lie much closer to the temperature contours, and match up at the 2.048 keV level of contour 7. The contour values in 10^{-26} sec^3 cm^{-3} are: (1) 350.0; (2) 7.90; (3) 0.9; (4) 0.45; (5) 0.22; (6) 0.11; (7) 0.043.

are found in the wake, apparently the result of heated, uncaptured material flowing past the secondary and into the wake region. Examination of the velocity structure of the gas shows an interesting effect. The material in the high temperature core of the wake is moving supersonically away from the secondary at a distance of 1.6×10^{11} cm. This is approximately at the sharp tip of contour 7 in Fig. 6.3. The gas continues to heat in the wake, with the heating primarily due to compressional and viscous effects. The core of the wake reaches velocities of 1200 km sec^{-1} and is supersonic with a Mach number of about 2. The low density in the wake keeps it in the Compton dominated domain so that X-ray cooling is not effective at lowering its temperature. The tip of the wake apparently is a second shock region, where the flow changes from a high velocity, low density, high temperature region, to the lower velocity, high density, low temperature regions of the surrounding material.

The low density at the inner core of the wake is easily seen in the density contour plots of Fig. 6.5. Figure 6.6 again plots the energy density contours, which are equivalent to pressure contours. Again, regions of instability appear as in Model 1. The cause of the onset of the thermal instability is more questionable in Model 2 than it was in Model 1. The requirement to extend the problem mesh leads to the creation of cells with very high aspect ratios both on the axis and perpendicular to the secondary at distances far from the secondary. Such cells may have a ratio of side dimensions on the order of 100. This causes a more severe loss of resolution for one

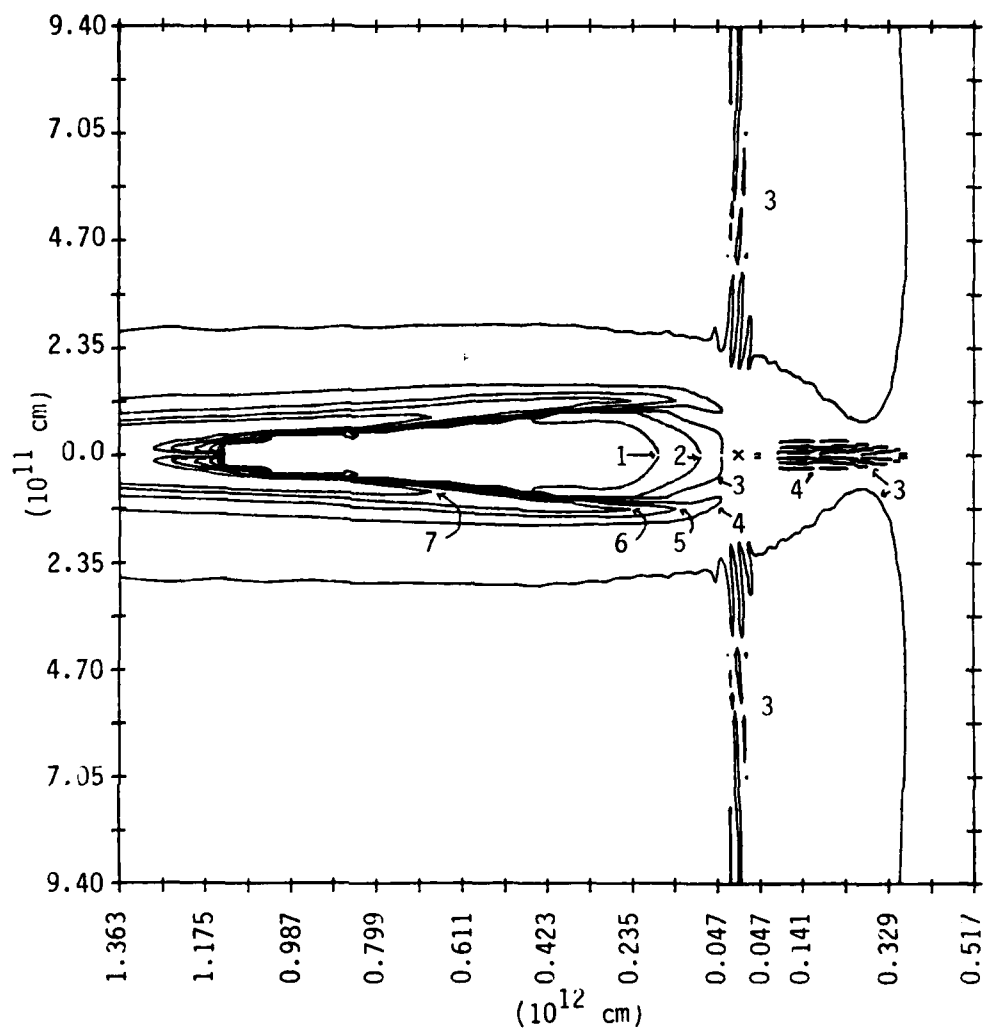Figure 6.5. Material Density Contours for Model 2. Regions of thermal instability are again noticable to the right, top and bottom of the secondary. Their origin are discussed in the text. Note the formation of an extended wake with a rarified core and high densities on it's boundaries. The contour values in 10^{-13} g cm^{-3} are: (1) 0.25; (2) 0.50; (3) 1.00; (4) 2.0; (5) 4.0; (6) 8.0; (7) 16.0.
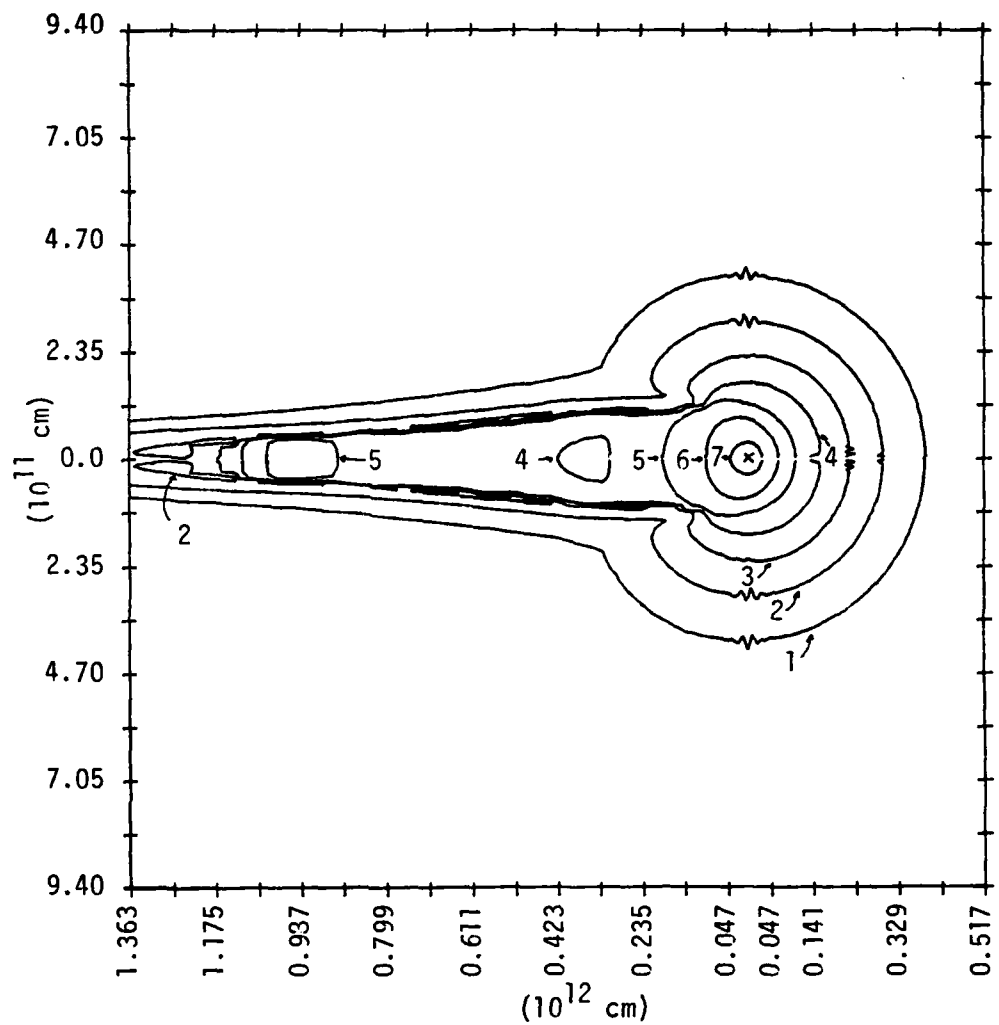
Figure 6.6. Energy Density Contours for Model 2. The energy density contours are equivalent to pressure contours. The contour values in ergs cm⁻³ are: (1) 1.0; (2) 3.0; (3) 9.0; (4) 27.0; (5) 81.0; (6) 243.0; (7) 729.0.

dimension in those cells as can be seen by the disturbances introduced into the energy contours. This may have provided the perturbations needed in the flow to start up the instabilities.

In Fig. 6.7, we plot P/F versus ρ/F for Model 2 as we did in Model 1. Again the essential correctness of the thermal instability assumption is verified. We note that there are two populations of gas, one the cool gas approaching the secondary along the lower portion of the curve, and the second the hot gas which is moving away from the secondary along the upper portion of it. The conspicuous wisp rising off the curve along the 10^7 °K line corresponds to the hot thin material in the wake behind the secondary. As noted above, this material is hot gas which the secondary could not capture, and is expanding away from the secondary while undergoing hydrodynamic heating. This is *supplying sufficient heating* to keep the gas hot and thin as it moves away. Remaining thin, X-ray cooling is not efficient, further supporting its high temperature. The high temperatures and pressures reached relative to the X-ray flux place the gas in the wisp seen in the figure.

This feature is not present in the results of Model 1. Its absence may be due to the smaller spatial scale which does not include as large a segment of the wake. Looking back at Fig. 5.1, we see that the wake does appear to be forming a low density, high temperature core, with a high density boundary. Expanding Model 1 may lead to the same effect that we see here.

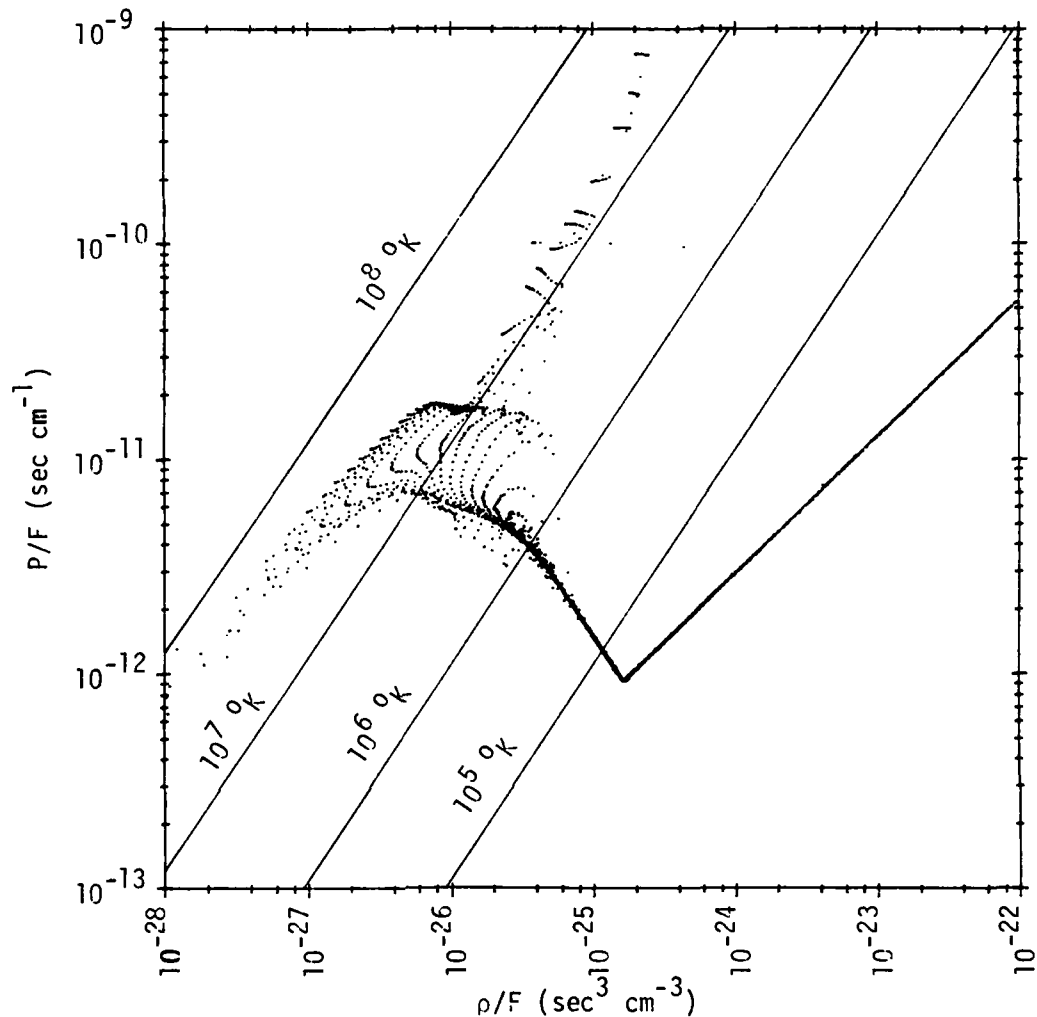We did repeat a time elapsed analysis of the temperature,

Figure 6.7. P/F vs ρ/F for Model 2. This is a plot of the gas pressure divided by the X-ray flux versus the gas density divided by the X-ray flux. It demonstrates the multi-valuedness of the pressure-temperature states of the gas. Lines of constant temperature are included for reference purposes. The sharpness of the corner in the lower right of the plot is a result of the equations used to fit the steady state temperature curves. Gas moving from left to right along the upper edge is undergoing cooling, while gas moving from right to left along the bottom is gas undergoing heating. The thin wisp rising above the curve along the 10^7 °K line represents the hot, low density material moving in the core of the wake. This feature is not seen in Model 1 since the problem did not include as much of the wake.

density, and energy density through the region of instability similar to that done in Model 1. The same type of wave-like behavior was found present. The instabilities again propagated with the velocity of the flow.

Figures 6.8 and 6.9 show the velocity and mass-flux fields for Model 2. On comparing Fig. 6.8 with Fig. 5.7, we note that the stagnation point behind the secondary is closer by a factor of two. In Fig. 6.9, we see that the accretion flow is again predominately from the sides of the secondary and there is essentially no accretion column formed.
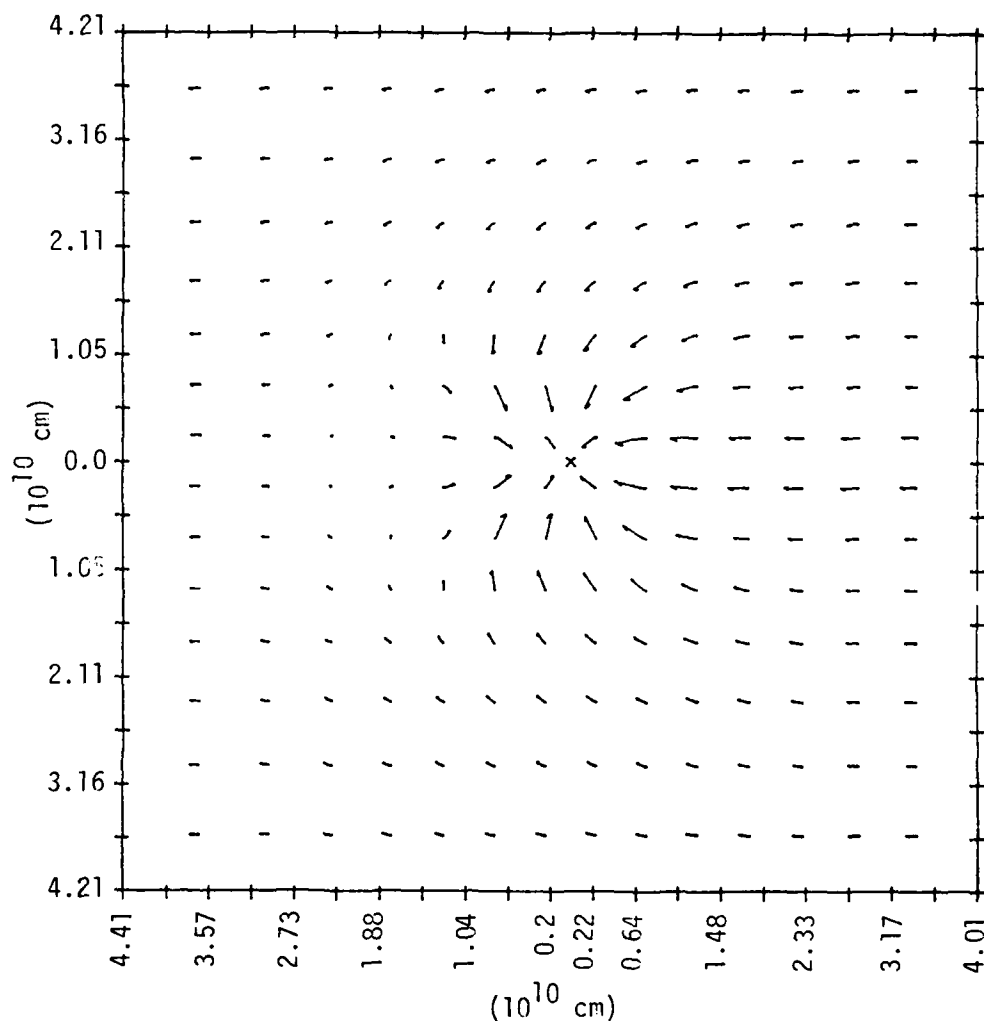
Figure 6.8.   Velocity Field for Model 2. This is a plot of the velocity field near the central accretion region of model 2. The vectors are scaled to a maximum vector of 1.371×10^8 cm sec^{-1}. The tail of each vector marks the point at which the velocity was taken. Note again the formation of a stagnation point near the left side of the secondary.

AD-A110 098   AIR FORCE INST OF TECH WRIGHT-PATTERSON AFB OH   F/G 3/1
              NUMERICAL STUDIES OF GRAVITATIONAL ACCRETION FROM X-RAY HEATED --ETC(U)
              DEC 81   J A LUPO
UNCLASSIFIED AFIT/CI-81-67D   NL

END
DATE
FILMED
3 82
DTIC

MICROCOPY RESOLUTION TEST CHART
NATIONAL BUREAU OF STANDARDS 1963 A
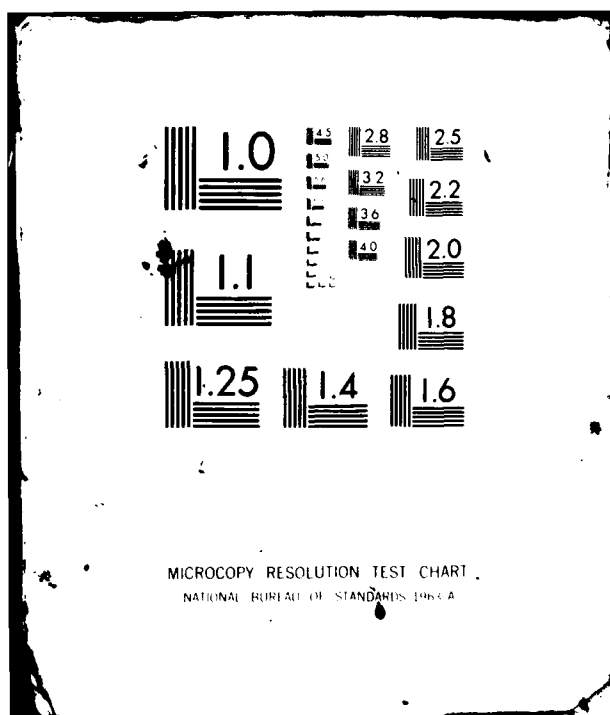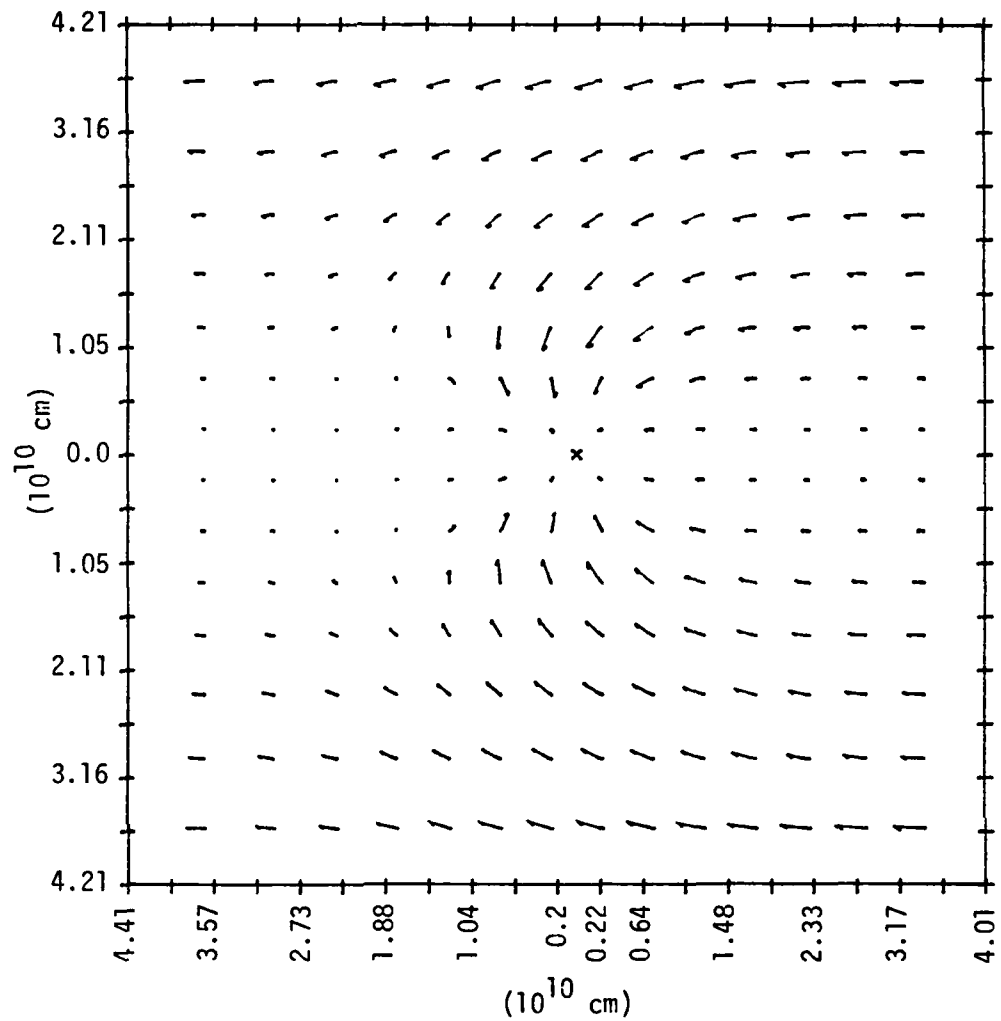
Figure 6.9. Weighted Momentum Vectors for Model 2. Plotted here are the momentum density vectors near the central accretion region of Model 2. Each momentum density vector was weighted by its distance off axis to highlight the mass flux into the central region. Vectors of constant length imply constant mass flux. Note again that the majority of the material accreted is captured from the sides. The vectors are scaled to a maximum vector of 2.51×10^5 g cm^{-1} sec^{-1}.

VII. PRELIMINARY ANALYSIS OF WIND SHUT DOWN EFFECTS

Models 1 and 2 were created to examine the effects of X-ray heating and the wind force on accretion from a stellar wind. Since they did not allow the X-ray radiation to impact on the forces driving the wind, the behavior of the gas in the wake is unrealistic. The densities and X-ray radiation are such that the atoms responsible for the wind force are heavily ionized near the secondary. Thus, we should not see the wind force dominating the secondary's gravity through the major portion of the wake.

Our basic goal in this study is to create a model in which the X-rays modify the forces driving the wind. With the behavior of Models 1 and 2 established, we can begin to formulate the necessary parameters for a system under which the X-rays ionize the L-shell electrons responsible for the wind force. To do this, we first need to get some idea of the impact that full wind ionization would have on system modeling requirements. This information will then provide restrictions on our model parameters.

A. Ballistic Particle Model

To handle this analysis without explicitly solving the differential equations for the system, we make the following assumptions to create a worst-case situation:

(a). Ionization and wind turn-off occur on a time scale much smaller than the time it takes the wind to cross from the surface of the primary to the orbit of the secondary. As a corollary, the wind force is assumed

to rapidly turn back on as it is shadowed from the X-rays.

(b). The X-ray luminosity is sufficient to strip the L-shell electrons responsible for the wind force everywhere outside of the X-ray shadow zone.

(c). The wind is approximated as ballistic particles free to move under the wind force and the force of gravity. Hydrodynamical effects are neglected.

(d). The effect of the secondary's gravity is ignored.

That these are worst-case assumptions can be seen by examining the effects of each assumption in more detail. For assumption (a), we first note that the wind crossing times (the time it takes for the wind to move from the primary's surface to the orbit of the secondary) are on the order of 10^4 seconds, and the orbital periods are on the order of 10^5 seconds. If the ionization times are on the order of the crossing time, then the wind will flow with little modification from its unionized state, and recovery upon entering the X-ray shadow will still occur before re-exposure. Rapid ionization thus has the most detrimental effect on the total wind flow.

There is an observational basis for assumption (a). Conti and Cowley (1975) performed optical spectroscopic observations of 4U1700-37. They found that absorption lines were strongly disturbed in the region trailing the secondary. This behavior was attributed to the wake produced by the secondary as it moved through the primary's wind. This disturbance was phase dependent and never

appeared ahead of the secondary. For this system, then, we have an actual case of the wind flow recovering before the secondary reappears.

The effects of relaxing assumption (b) are more difficult to visualize. If the wind is not ionized everywhere that it is exposed to the X-rays, then normal wind flow will occur progressively closer to the secondary as the X-ray luminosity is decreased. One of the purposes of Model 3 is to determine the location of the wind shut-down.

As for assumption (c), inclusion of hydrodynamical effects would add the supportive effects of gas pressure, resulting in a smoothing of the flow and reduction of any velocity changes. Finally, from assumption (d), if the effects of the secondary's gravity are included, the material would be attracted towards the secondary, increasing the likelihood of the material being accreted by the secondary.

The variables needed for our ballistic analysis are shown in Fig. 7.1. Region A is the X-ray shadow zone and Region B is the X-ray illuminated zone. The binary separation is given by a. R_0 is the primary's radius. R is the distance to the outer edge of the shadow zone. Φ is the angle between the line-of-sight tangent point and the line-of-centers for the system. Finally, Ψ is the angle between the line-of-centers and R.

When the wind is shut down, there are two possible conditions under which material will still be present in the orbit of the
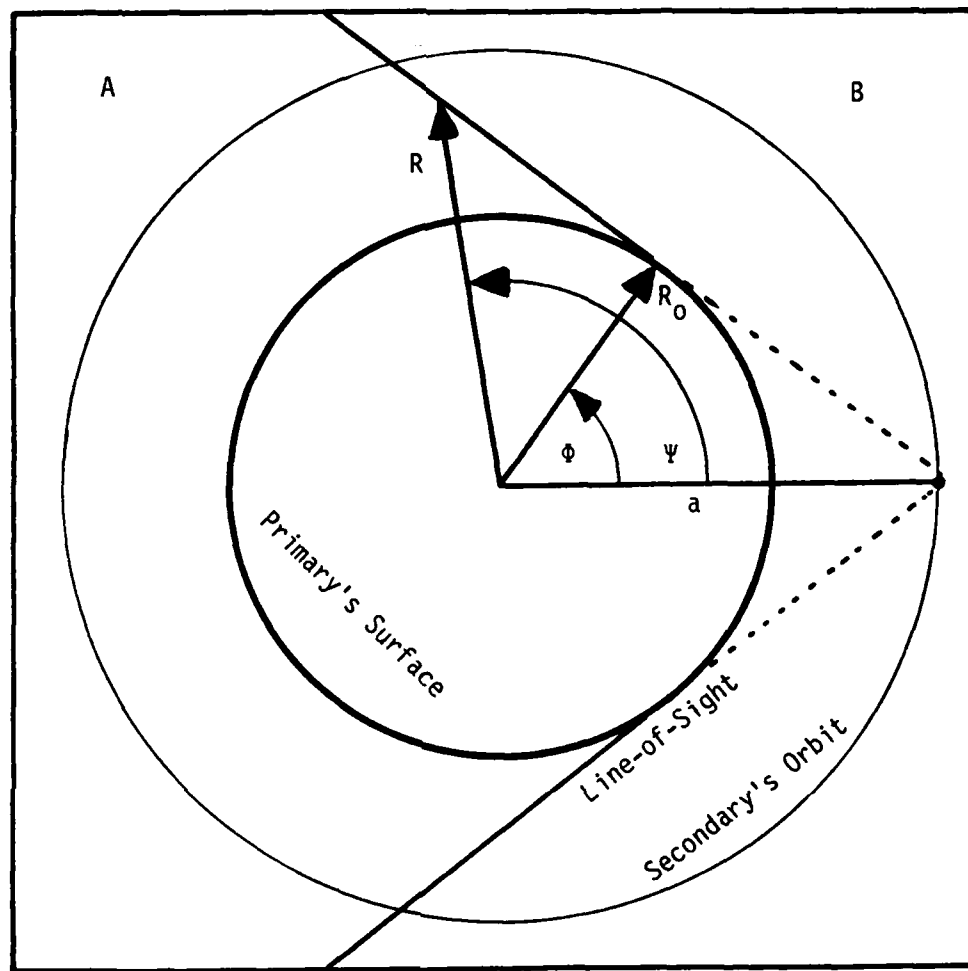
Figure 7.1. Variables for Ballistic Analysis. Assuming the stellar wind is shut-off everywhere it is exposed to the secondary's X-rays, we have Region A as the shadow zone and Region B as the illuminated zone. a is the binary separation. Φ is the angle to the line-of-sight tangent point at the primary surface. Ψ is the angle at which the wind enters Region B at some radius R above from the primary. R_0 is the primary radius.

secondary for the secondary to accrete. Let us define the crossing time t_c as the time it takes the wind to cross from the surface of the primary at R_0 to the orbit of the secondary at a, and the intercept time t_i as the time it takes the secondary to move from $\Psi = 0$ to $\Psi = \Psi_i$. The first condition is then simply that $t_c = t_i$. In other words, the secondary directly intercepts material as it leaves the primary.

During the period t_c the wind spends some time being driven by the wind force through region A and then time free-falling as the wind force is shut down in Region B. Therefore, the second condition is to allow the material to continue free-falling past the secondary's orbit to some radius R_f and then free-fall back to the orbit. The material thus spends additional time in free-fall before crossing the orbit for the second time. For this case, we also require that $t_c = t_i$, but t_c may now be substantially longer.

It is clear that material reaching escape velocity before shutdown will never be captured unless condition 1 is met. Also, material with insufficient energy to reach the secondary's orbit will not be captured. This last situation is improved if assumption (d) is relaxed, resulting in a form of potential lobe overflow.

With the limits of escape velocity and minimum energy established, we can constrain ourselves to considering only material leaving between some Ψ_{min} and Ψ_{max}. The radius at which the wind attains the minimum energy required to reach the secondary's orbit can be found from

$$\tfrac{1}{2} v^2 - GM/R_{min} = -GM/a \ . \tag{7.1}$$

Now, the wind velocity at R_{min} is specified from Eq. 3.5 as

$$v = v_\infty (1 - R_0/R_{min})^{\tfrac{1}{2}} \ . \tag{7.2}$$

Equations 7.1 and 7.2 are now used to yield an expression for R_{min}:

$$R_{min} = \frac{\tfrac{1}{2} v_\infty^2 R_0 + GM}{\tfrac{1}{2} v_\infty^2 + GM/a} \ . \tag{7.3}$$

Consequently, for Ψ_{min}, we have

$$\Psi_{min} = Arccos(R_0/R_{min}) + \Phi \ . \tag{7.4}$$

Now, to find Ψ_{max}, we have the escape velocity given by

$$v_{esc} = (2GM/R_0)^{\tfrac{1}{2}}. \tag{7.5}$$

But again from the wind velocity relation of Eq. 7.1 we have

$$v_{esc} = v_\infty (1 - R_0/R_{esc})^{\tfrac{1}{2}} \ , \tag{7.6}$$

hence,

$$R_{esc} = R_0 (1 - v_{esc}/V_\infty)^{-2} \ . \tag{7.7}$$

Therefore, Ψ_{max} is given by

$$\Psi_{max} = Arccos(R_0/R_{esc}) + \Phi \ . \tag{7.8}$$

With Ψ_{min} and Ψ_{max} established to limit our search range, we can now proceed to calculate the required times. t_i is given simply by

$$t_i = T \Psi / 360 \ , \tag{7.9}$$

where T is the orbital period. Under the requirements of condition 1, we first have the wind moving under the wind force from R_0 to some radius R. The time to cross this distance is then

$$t_1 = \int_R^{R_0} (v_\infty (1 - R_0/r)^{\tfrac{1}{2}})^{-1} \ dr \ . \tag{7.10}$$

The test particles then free-fall from R to a, so this time is given by

92

$$t_2 = \int_a^R (2(E+GM/r))^{-\frac{1}{2}} \, dr \ , \qquad (7.11)$$

where

$$E = \tfrac{1}{2} v_\infty^2 (1 - R_0/R) - GM/R \ . \qquad (7.12)$$

Finally, the total crossing time is given by

$$t_c = t_1 + t_2 \ . \qquad (7.13)$$

An iterative search is made for all values of R allowed between Ψ_{min} and Ψ_{max} attempting to enforce $t_c = t_i$. If no match is possible, we then invoke condition 2. Here, we again have t_1 given by Eq. 7.10 but now t_2 is the time to move from R to R_f under free fall:

$$t_2 = \int_{Rf}^R (2(E + GM/r))^{-\frac{1}{2}} \, dr \ , \qquad (7.14)$$

with E given again by Eq. 7.12. We now need to include the free-fall time from R_f back to a. Calling this t_3, we have

$$t_3 = \int_{Rf}^a (2(GM/r - GM/R_f)^{-\frac{1}{2}} \, dr \ . \qquad (7.15)$$

Hence, the total crossing time is now

$$t_c = t_1 + t_2 + t_3 \ . \qquad (7.16)$$

Since we are able to compute the wind velocity from the above, it is possible to estimate the wind's density in the vicinity of the secondary. Assuming the primary's mass loss rate is constant, we have

$$dM_0/dt = 4 \pi r_0^2 \rho v \ . \qquad (7.17)$$

Thus, at the point the wind is shut down, we will have a density of:

$$\rho_1 = \frac{dM_0/dt}{4 \pi r^2 v} \ , \qquad (7.18)$$

or, after including Eq. 7.1,

$$\rho_1 = \frac{dM_0/dt}{4\pi R^2 v_\infty (1-R_0/r)^{\frac{1}{2}}} . \qquad (7.19)$$

As this material expands on its way to the secondary's orbit, the density times the area remains constant, requiring

$$4\pi r^2 \rho_1 = 4\pi r^2 \rho_2 . \qquad (7.20)$$

Equation 7.20 reduces to

$$\rho_2 = \rho_1 r^2 / a^2 . \qquad (7.21)$$

Therefore, the density at the position of the secondary can be roughly approximated by

$$\rho_2 = \frac{dM_0/dt}{4\pi a^2 v_\infty (1-R_0/a)^{\frac{1}{2}}} . \qquad (7.22)$$

This analysis is applied to five of the better studied massive X-ray binary systems and to Model 2. The results are summarized in Table 7.1. In every case, intercept condition 2 must be invoked. It is found that material is always present in the orbit of the secondary and at slower velocities and higher densities than unimpeded wind flow. This would allow much higher accretion rates so that the observed luminosities could be supported with much lower mass loss rates from the primary. However, since the stellar wind model of Castor, Abbott and Klein (1975) assumes that the wind is spherically symmetric, the effects of the strong asymmetry introduced by shutting off part of the wind and of material falling back into the primary's atmosphere are presently unknown.

Strongly shutting down the wind near the shadow zone clearly introduces major three-dimensional effects. Within the limits of our

94

TABLE 7.1.
Ballistic Analysis Results

	Vela X-1 (4U0900-40)	Model 2	4U1700-37	Cyg X-1 (4U1956+35)	Cen X-3 (4U1118-60)	SMC X-1 (4U0115-73)
Period (days)	8.96	11.3	3.41	5.6	2.09	3.90
v_∞ (km sec^{-1})	1430	750	2090	1910	2260	2110
dM_0/dt (M_θ yr^{-1})	2.46×10^{-5}	7.42×10^{-6}	7.00×10^{-6}	2.50×10^{-6}	1.75×10^{-6}	1.75×10^{-6}
T_c - On (days)	0.26	0.55	0.10	0.18	0.06	0.10
T_i (days)	1.69	2.27	0.58	1.25	0.37	0.73
ρ - On (g cm^{-3})	1.10×10^{-14}	5.05×10^{-14}	7.01×10^{-14}	1.02×10^{-14}	3.87×10^{-14}	1.65×10^{-14}
ρ - Off (g cm^{-3})	9.41×10^{-14}	1.98×10^{-13}	5.55×10^{-13}	1.24×10^{-13}	3.31×10^{-13}	1.72×10^{-13}
v_x - On (km sec^{-1})	864	421	1140	1370	1290	1300
v_x - Off (km sec^{-1})	101	107	145	113	151	125

Table 7.1. Worst-case ballistic results for several well studied X-ray binary star systems. In every case, test particles passed the orbit of the secondary and then free fell back to it. On and Off parameters refer to unimpeded wind flow and flow turned off by X-ray ionization respectively. Note the significant change in the wind velocity and density after shutdown. This tends to indicate that significant improvements in accretion efficiency can be experienced, allowing one to relax system parameters, such a primary mass loss rates, appreciably. Mass loss rates and wind velocities at infinity are based on values from Petterson (1978).

two-dimensional model, we have to limit the distance of the shutdown region from the secondary. If the wind is shut down too far away, we will not be able to adequately account for the wind flow prior to the intercept of the secondary. This is because the two-dimensional model does not allow the wind to diverge as it moves radially from the primary, so the lateral extent of the problem mesh must remain small enough to keep the flow reasonably planar. For Models 1 and 2 we were not overly concerned with the wind behavior far outside the accretion radius for there were no processes included in the models to affect the wind flow along the side boundaries other than the secondary's gravity. We made the decision to find system parameters which would cause the wind shut-down point to fall between 1/4 and 3/4 of the distance between the secondary and the primary's surface for the initialized state of the model.

B. X-ray Ionization

We now need some way of determining the ionizing effects of the X-ray radiation. With that determined, we can estimate the impact of the ionization on the wind force. The work of Hatchett, Buff and McCray (1976) (cf. Tarter, Tucker and Salpeter 1969) is well suited for this purpose. They examined the ion population levels in a gas exposed to X-rays. They found that the ionization populations could be specified as a function of the parameter ξ, given a source spectrum of X-rays. Figure 7.2 is adapted from their results for oxygen under the assumptions of an optically thin gas and a blackbody spectrum with a temperature of 2.5 keV. The behavior shown for
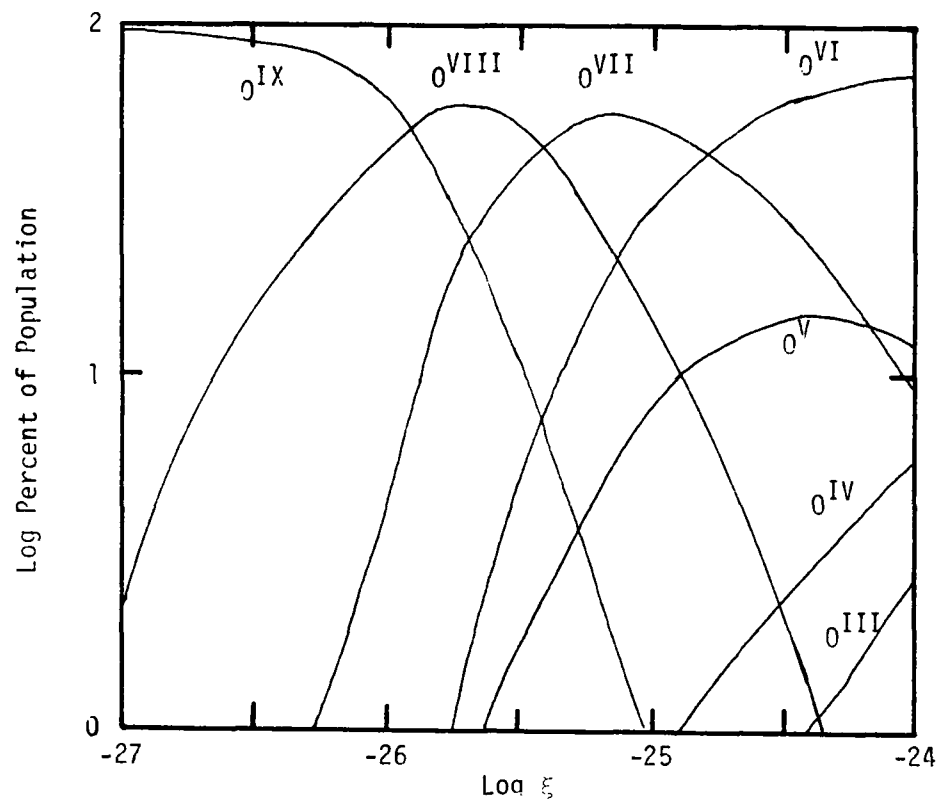
Figure 7.2. Ionization Equilibria for Oxygen. A sample ion population distribution is shown here for oxygen in an optically thin gas exposed to a blackbody X-ray spectrum with a color temperature of 2.5 keV. This figure was adapted from the results of Hatchett, Buff and McCray (1976).

oxygen is typical of the other elements as well, although the exact features vary. There is also a considerable change in the behavior of the ionization states if the gas is optically thick. Oxygen, for instance, goes from neutral to fully ionized between ξ's of 10^{-24} to 10^{-27} if optically thick.

Recall from Chapter III that carbon, nitrogen, and oxygen are the main contributers of lines responsible for the wind force (Castor, Abbott and Klein 1975). Our model code does not have the capability to explicitly determine the ionization equilibria of the elements, so we made the approximation that the wind is turned off at the point at which 50% of the oxygen L-shell electrons are stripped. Oxygen is used primarily because it is the only element for which data is given for optically thin conditions. Using this as an overall indicator of the wind ionization state is not too unreasonable, for carbon and nitrogen ionize at slightly larger values of ξ. A larger source of error here is the fact that our code assumes a 22 keV exponential X-ray spectrum. Such a spectrum is richer in low energy photons than a blackbody spectrum. The point is that the model will show the main features of wind shutdown under X-ray illumination, even though the exact details vary.

Let ξ_{off} be the value of ξ for which 50% of the oxygen L-shell electrons are stripped. The value of ξ_{off} is estimated from Fig. 7.2 as 1.212×10^{-25} sec^3 cm^{-3}. With this value of ξ_{off} and the desired location of the shutdown point relative to the secondary established, we are ready to construct our final model.

VIII. MODEL 3

We are now in a position to establish the parameters for Model
3. The self-consistency constraints of the first two models are
still to hold in Model 3. In Chapter VII, we discussed the selection
of the value of ξ_{off} at which the wind would be shut off. This value
was choosen to be 1.212×10^{-25} sec^3 cm^{-3}. The wind shut-down point
must also fall between 1/4 and 3/4 of the distance between the
primary's surface and the secondary.

A. Initializing Model 3

There is an additional requirement on the size of the binary
system that must be considered. The wind undergoes very stong
acceleration close to the surface of the primary. This is evident
from the acceleration found in the derivation of the wind potential
(Eq. 3.7):

$$\partial v / \partial t = \tfrac{1}{2} \, v_{\infty}^2 \, R_0 \, / \, r^2 \,. \qquad (8.1)$$

The wind velocity will change rapidly. Consequently, to achieve
reasonable resolution of the velocity, we have to have fine spatial
resolution near the primary's surface. Numerical accuracy in our
model makes it desirable to change cell dimensions no more than 10%
from one cell to its neighbor. With a maximum of 120 cells available
in the z direction (re. Fig. 3.3), there is a maximum dimension which
can be simulated accurately. It turns out that Vela X-1 is not a
suitable choice because of this limitation.

A second reason exists for not using the Vela X-1 system. The
ξ_{off} contour occurs extremely close to the surface of the primary

causing it to approximate the worst case conditions explored in Chapter VII. It is clearly apparent that a new system is required as a basis for our model.

The most obvious candidate to examine first is the 4U1700-37 system. The parameters for this system are given in Table 2.1. It has a massive, high luminosity primary combined with a small separation distance and modest X-ray luminosity. We therefore begin the process of enforcing self-consistency using this system as a basis for model parameter selection.

We anticipate that the system will be initially similiar to Model 1 due to the higher densities in the wind. Higher densities have the effect of moving the contours of steady state temperatures closer to the secondary. From Model 1, we again assume an accretion efficiency of 0.4. With the required accretion rate given by Eq. 5.1 as

$$dM_x/dt = 10\ L_x/c^2\ ,\qquad\qquad (8.2)$$

the accretion rate needed to support the luminosity of 8×10^{36} ergs $\sec^{-1}$ (re. Table 2.1) is 8.89×10^{16} g $\sec^{-1}$. Recall that Eq. 4.11 giving the primary mass loss rate as a function of the accretion rate had the form

$$dM_o/dt = \frac{dM_x/dt\ v_\infty^4\ (a-R_o)^2}{\alpha\ (GM_x)^2}\ .\qquad (8.3)$$

Using the observed parameters from Table 2.1, Eq. 8.3 yields a mass loss rate of 6.7951×10^{-5} M_Θ yr^{-1}.

We can now find the location of the wind cut-off point. In

Chapter VII we selected a value of $1.212 \times 10^{-25} \sec^3 cm^{-3}$ for ξ_{off}. Since r_x along the line of centers is simply $a-r_0$, we can determine r with the aid of Eq. 4.10 in the form

$$\xi = \frac{dM_0/dt \ (a-r_0)^2}{4 \pi r_0^2 L_x v_\infty (1-R_0/r_0)^{\frac{1}{2}}} \qquad (8.4)$$

Doing a fast iterative search for r between R_0 and a locates the shutdown point at about 22.05 R_θ, or just 1 R_θ above the surface of the primary. This is entirely too close for our model. The spatial mesh is not able to adequately resolve velocities so near the primary's surface.

Our next step is to modify the system parameters in an attempt to move the shutdown point farther above the surface. To do this, we elect to reduce R_0 from 21 R_θ to 19 R_θ without changing the other system parameters. With this value for R_0, Eq. 8.3 yields a required mass loss rate of 1.0151×10^{-4} M_θ yr^{-1}. This mass loss rate is 3.3 times the maximum mass loss rate established by Eq. 5.4, implying that the primary for this model must be 3.3 times more luminous than that of the observed system. The required primary mass loss rate is also a factor of 3.4 above the maximum probable value from the observations of Hutchings (1976). Recall that we are artifically enforcing self-consistency using the maximum X-ray luminosity. We again use Eq. 8.4 to determine that the wind shutdown point occurs at about 21.8 R_θ, or 2.8 R_θ above the surface of the primary. This location is adequately far above the surface of the primary. Increasing the distance would require more severe modifications of

101

the system parameters.

The *minimum* spatial resolution obtainable at the surface of the primary is 5.0×10^9 cm. This yields a velocity resolution of 40.6 km sec^{-1}. We can compare this to the escape velocity from the primary's surface of 775 km sec^{-1} and to the wind velocity at the orbit of the secondary of 1266 km sec^{-1}. Our resolution is about 5% of the escape velocity, giving us good division between gravitationally bound and unbound material.

The parameters finally established for this model are given in Table 8.1. Using them, we again initialize Model 3 as we have done with Models 1 and 2. The accretion radius for this model is found to be 2.48×10^{10} cm. Figure 8.1 can be used to estimate the initial effects of X-ray heating. As one can see, at 5 keV R_T (re. Eqs. 6.1-2) actually lies inside R_G, while at 1 keV R_T lies at an average distance of 1.36 R_G. In this case, R_T and R_G show an even closer match than was found in Model 1 (re. Fig. 6.1). At 5 keV, the value of R_G is 1.81×10^{10} cm, and, of course, at 1 keV, R_G is 5 times larger.

As we did with Models 1 and 2, we examine the velocity structures in the initialized gas. We find that the gas is supersonic inside the accretion radius, unlike Models 1 and 2 which were subsonic inside the accretion radius. We can also calculate the point at which the wind force exceeds the secondary's gravity along the line-of-centers on the downwind side of the secondary (re. Eq. 5.13). This point turns out to be 1.88×10^{11} cm from the secondary,

TABLE 8.1. Parameters for Model 3

Base System: 4U1700-37

	Observed	Model
a (R_θ)	30	30
$R_o(R_\theta)$	21	19
v_∞ (km sec^{-1})	2090	2090
M_x (M_θ)	1.5	1.5
L_x (ergs sec^{-1})	8×10^{36}	8×10^{36}
L_o (ergs sec^{-1})	4×10^{39}	1.33×10^{40}
dM_o/dt (M_θ yr^{-1})	$7.3\text{-}30.0\times10^{-6}$	1.012×10^{-4}
α	---	0.4

Table 8.1. The parameters used for Model 3 are summarized here. The observed values are taken from Table 2.1. The values selected for this model differ from the observed values only in the radius and luminosity of the primary.
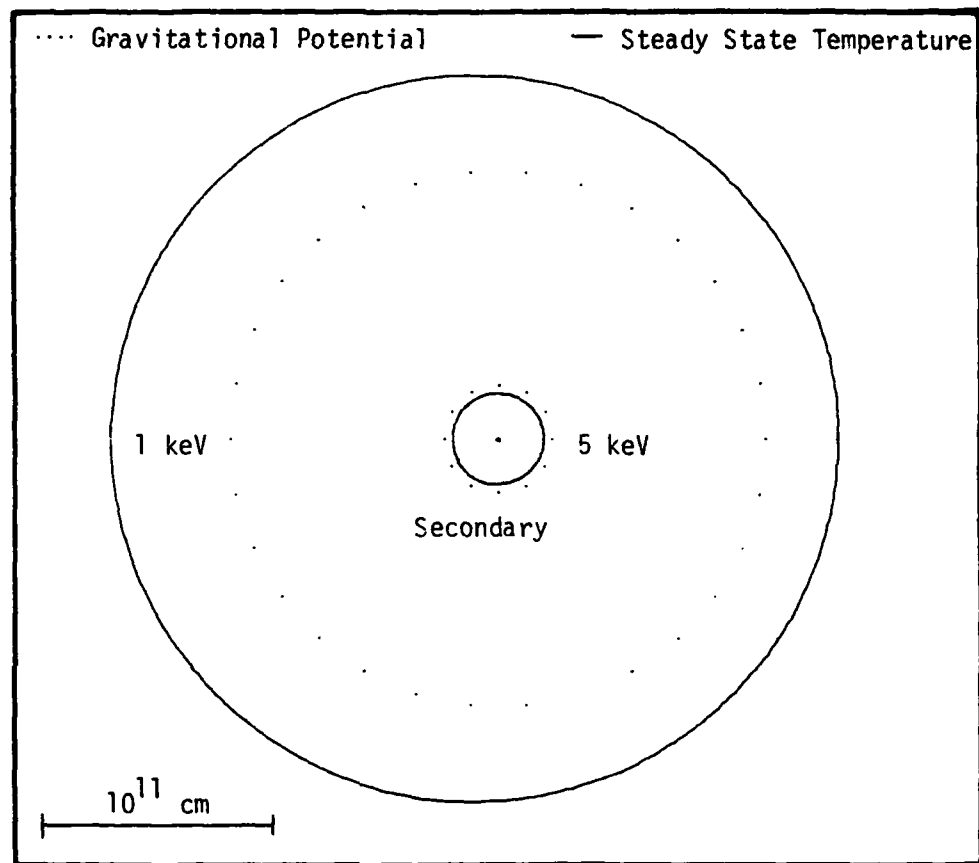
Figure 8.1. Initial Gravitational Potential and Steady State Temperature Contours for Model 3. The steady state temperature and gravitational potential contours for the 1 and 5 keV levels are plotted here for the initialized state of Model 3. The 5 keV temperature contour lies inside its gravitational counterpart, while the 1 keV temperature contour lies an average of 1.36 times the distance of its counterpart.

or about 7.62 R_a. This is nearly twice as far in terms of R_a's as was found in Models 1 and 2.

B. Calculation Results

We start the calculation and again trace the model's behavior in time. Only in this case, the model never approachs the quasi-steady state of the previous two models. Instead, the accretion ratio and luminosity fluctuate on a time scale of about 2 hours. The behavior of the luminosity is shown in Fig. 8.2.

Features related to the model startup period cover the interval from 0 hours to about 13 hours. This is the time needed for the initial material to clear the central portion of the spatial mesh. After the startup period, we note that sharp peaks occur in the luminosity. The maximum luminosities are 4 to 5×10^{38} ergs sec^{-1}, while the minimum luminosity is 8×10^{36} ergs sec^{-1}.

Referring back to Eq. 2.7, we find that L_{edd} for this model is 2×10^{38} ergs sec^{-1}. Examining the duration of the peaks, we note that they exceed L_{edd} for periods of about 22 minutes. We will address this problem of exceeding the Eddington luminosity in Chapter IX. However, we note here that the model did not incorporate a treatment of radiation pressure, hence it could not be expected to properly account for the limiting effects of the Eddington luminosity.

Because of the variations occuring in the luminosity, the contour and vector plots for this model represent only one instant in time. All of these plots are made at 24.29 hours into the model run. This time represents a period of decreasing luminosity immediately
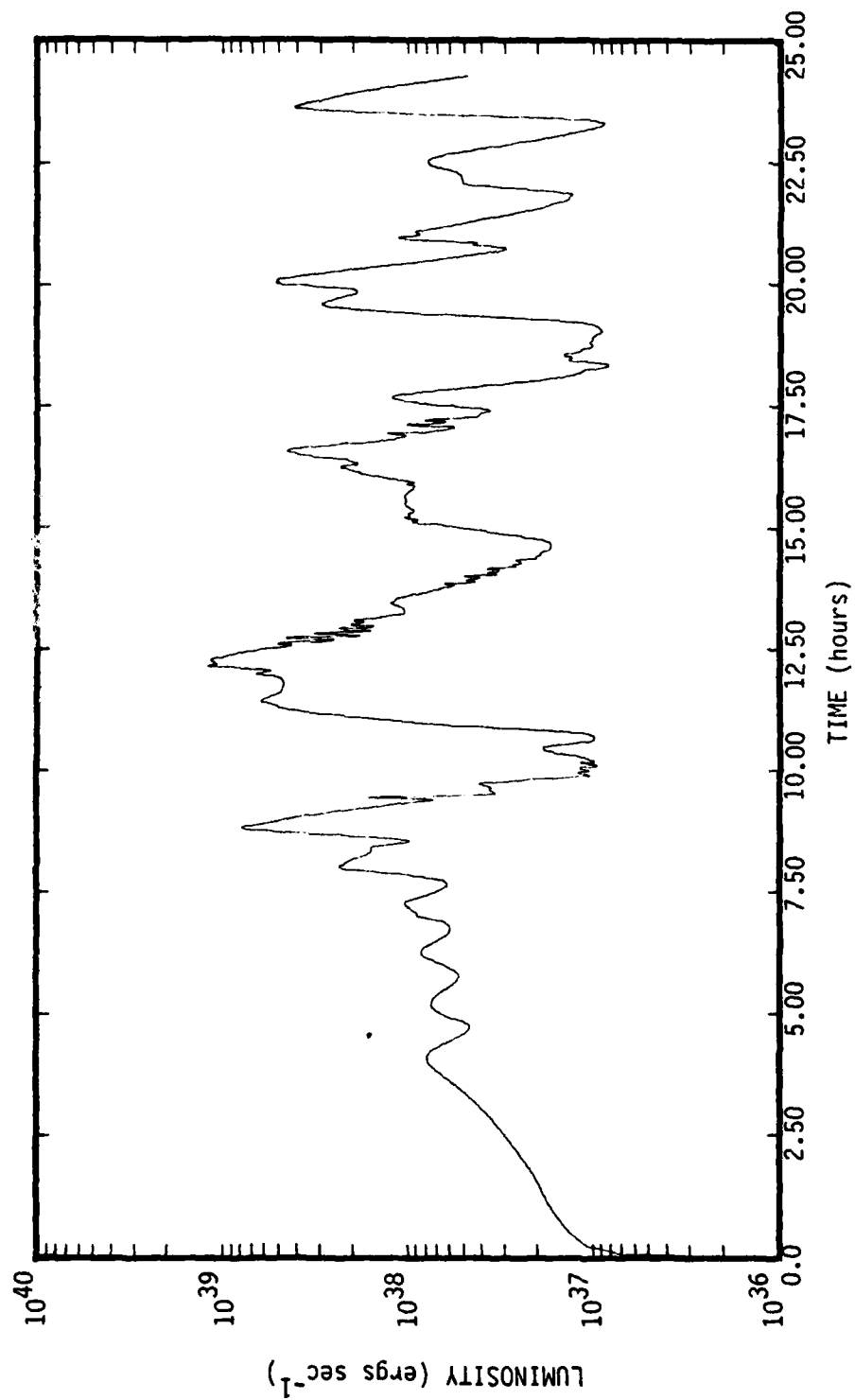
Figure 8.2 X-ray Luminosity VS Time For Model 3

106

following the last peak in Fig. 8.2. It also corresponds to the time at which we terminated our calculation. To examine the time variations, we produced several movies of the density contours evolving in time. Analysis of these movies is used in the interpretation of the plots presented here.

The density contour plot, shown in Fig. 8.3, exhibits very complicated structure. The closing of the contours to the right of the secondary is a direct result of the action of the varying X-ray luminosity on the wind force. A feedback mechanism is evidently in action. The varying density in the wind as it passes the secondary causes a variation in the luminosity. Increasing luminosity causes the wind shutdown point to move closer to the primary's surface, and vice versa. This in turn introduces new fluctuations in the wind density.

To better visualize the enhancement process, let us follow a packet of wind material as it travels from the surface of the primary to the secondary. As this packet leaves the surface of the primary, it reaches a state at which ξ is less than ξ_{off}. At this point it begins to decelerate under the influence of the primary's gravity. Other packets are able to catch up to it from behind, causing the density of the packet to increase. As a consequence ξ now increases above ξ_{off} and the packet can move again under the wind force until the force is shut off again.

This effect causes waves of enhanced density to be created. As these sweep by the secondary, they provide additional material for
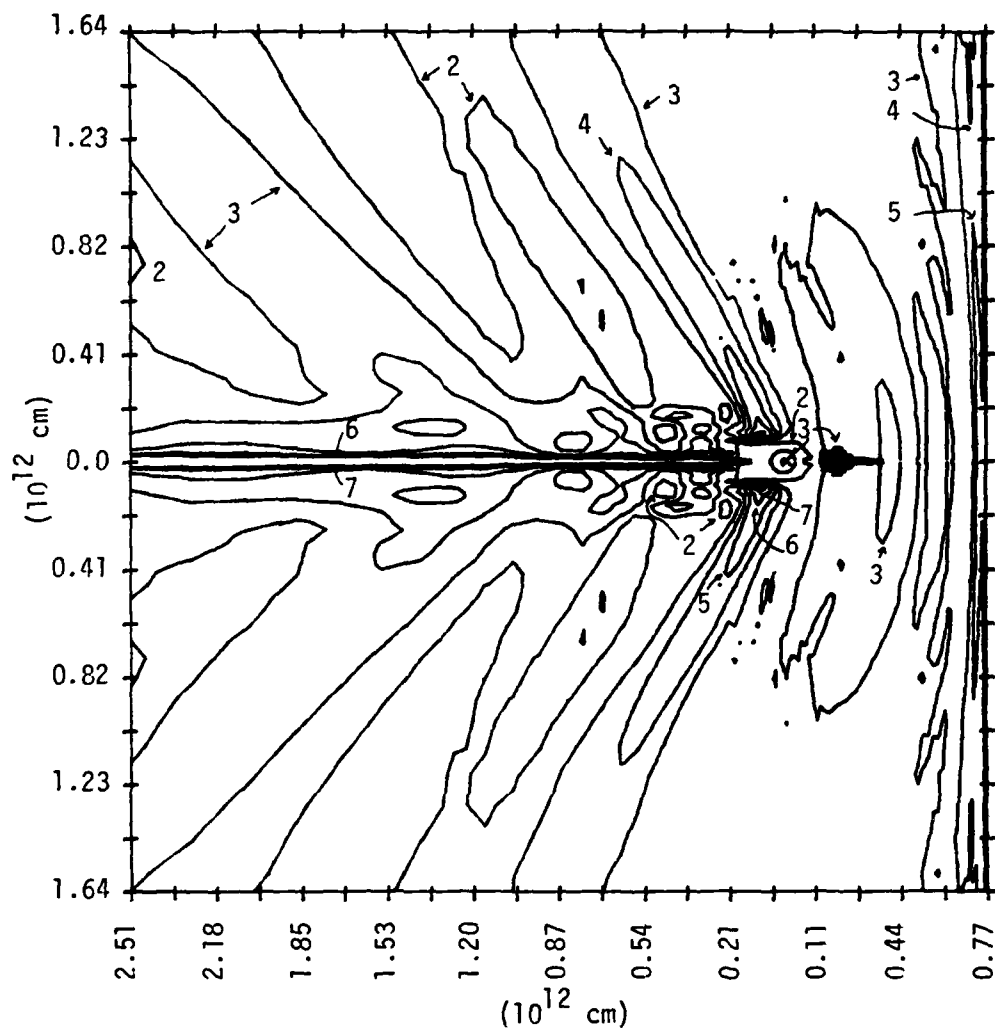
Figure 8.3. Density Contours for Model 3. As in the previous models, the secondary is marked by the small x. The surface of the primary now lies essentially on the right hand border. The material flows from right to left. Model 3 exhibited strong oscillations, and thus the contours changed with time. Those presented for Model 3 were taken at 24.29 hours of simulation time into the problem. We note in particular the build up of enhanced density regions between the secondary and the right hand side, and the strong turbulence introduced in the wake. These enhanced density regions are both caused by, and result from, the fluctuating luminosity. The contour values in units of 10^{-11} g cm^{-3} are: (1) 0.1; (2) 0.22; (3) 0.46; (4) 1.0; (5) 2.2; (6) 4.6; (7) 10.0

accretion, causing an increase in the luminosity. The increased luminosity in turn affects the location where the wind is shut off. This feed-back mechanism causes the luminosity to fluctuate on the same time scale as the wind-crossing time. The effects seen in an actual system will be modified by the effects of orbital motion and any material storage time introduced by formation of an accretion disk around the secondary. Since these enhanced density waves are propelled by the wind potential, it is not suprising that the major flaring is occurring on the same time scale as the wind crossing time.

The energy density contours are displayed in Fig. 8.4. When followed in time, the energy density contours display the behavior expected in light of the fluctuations observed. As the luminosity increases, the energy density, hence the pressure, is seen to increase. This inhibits the flow of incoming material, causing a drop in the accretion rate. As the accretion flow is shut off, the luminosity drops, the gas cools, and the accretion rate picks up again.

Figures 8.5 and 8.6 display the temperature and ξ contours. As in the previous two models, the values of the ξ contours were selected such that the steady state temperatures they represent correspond to the values of the temperature contours. For the time shown, we find that the two sets of contours essentially match up, except near the inner contours which represent the maximum temperatures. On examining plots made during a period of increasing
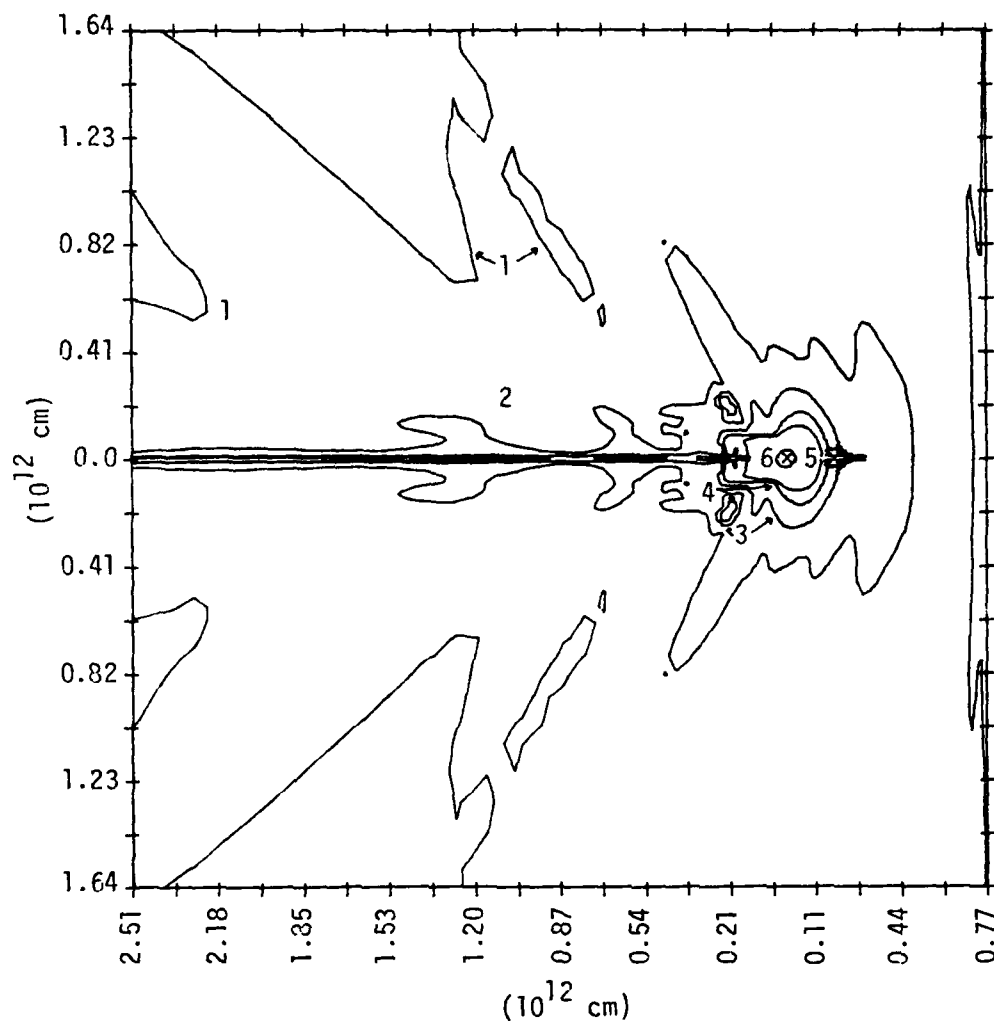
Figure 8.4. Energy Density Contours for Model 3. The contour values
in units of ergs cm^{-3} are: (1) 7.68; (2) 38.4; (3) 192.0; (4) 960.0;
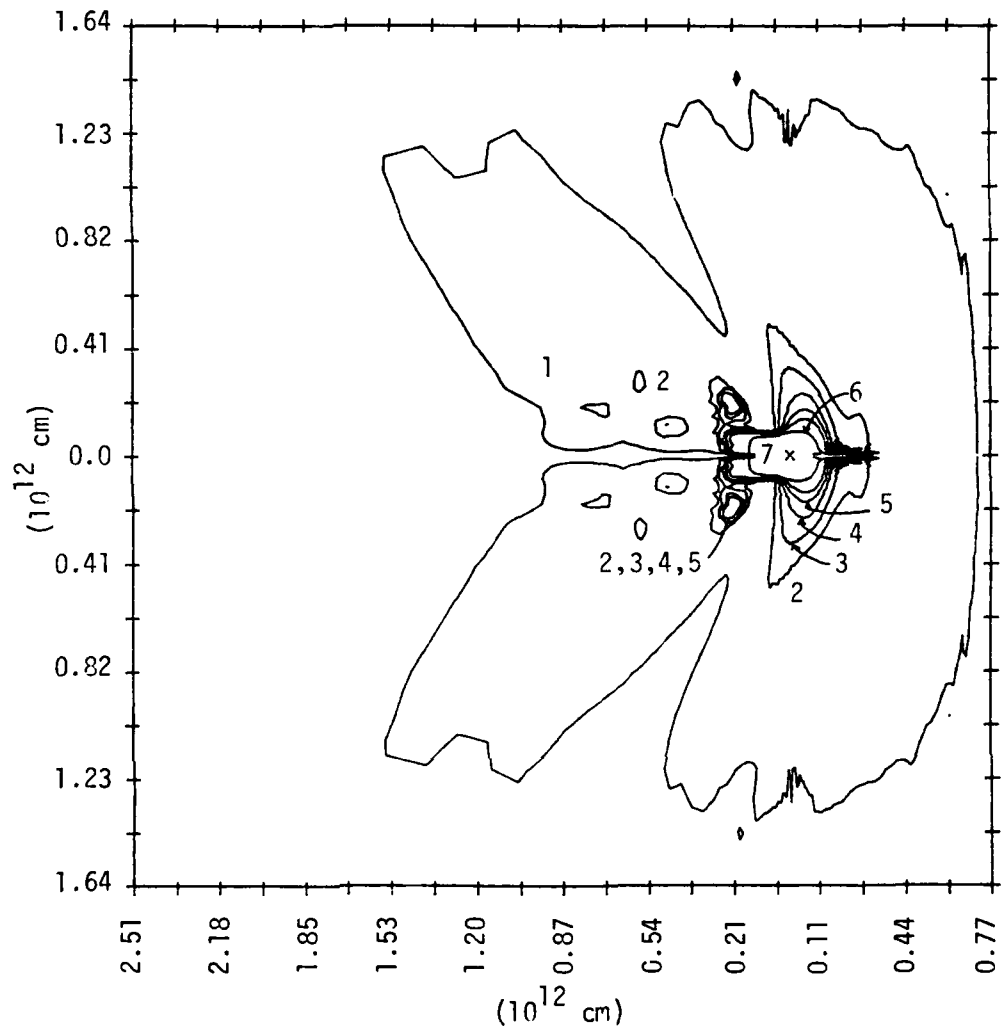(5) 4800.0; (6) 24000.0

Figure 8.5. Temperature Contours for Model 3. Strong turbulence is clearly seen in the wake behind the secondary. Note the radical departure from the smooth spherical shapes of the previous models. The contour values in eV are: (1) 1.7; (2) 5.1; (3) 15.0; (4) 46.0; (5) 140.0; (6) 410.0; (7) 1200.0
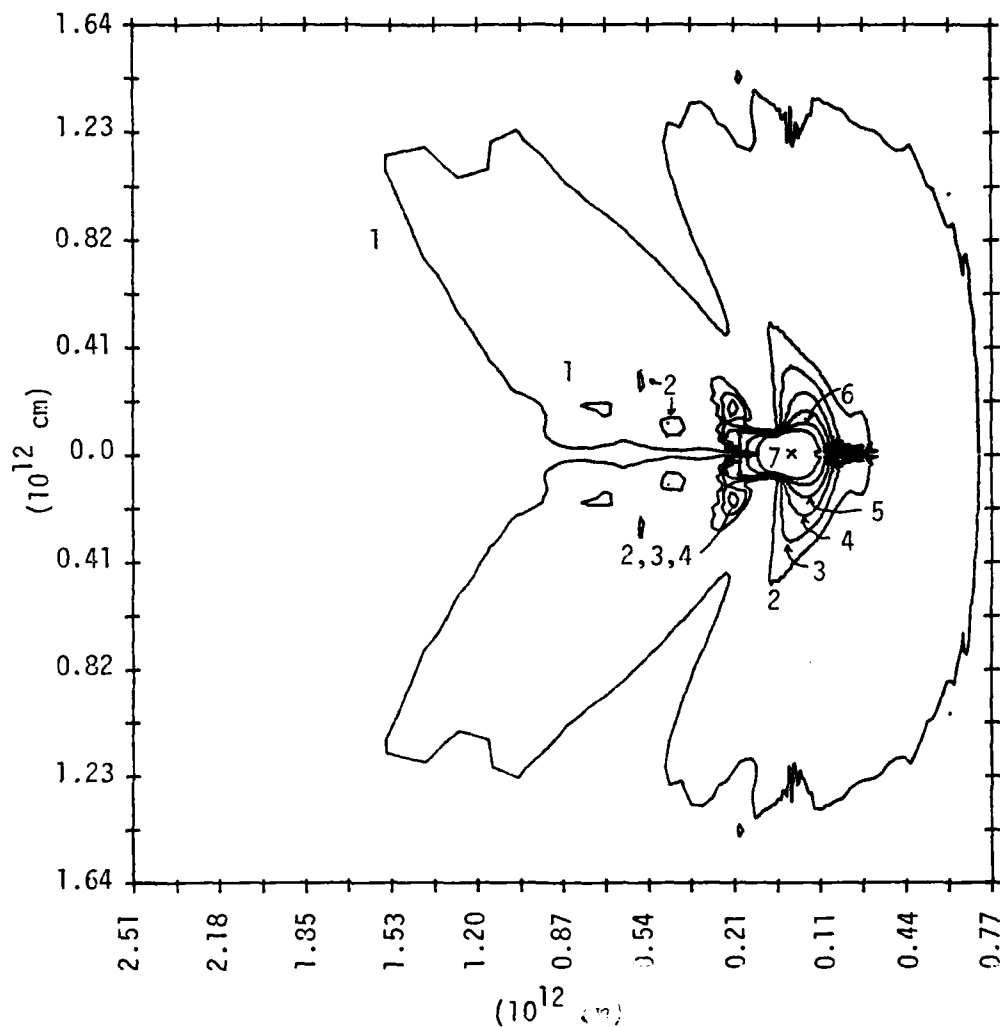
Figure 8.6. ξ Contours for Model 3. These contours are no longer the spherical shapes found by Hatchett and McCray (1977). The flow has been strongly perturbed and no longer resembles the steady flow they assumed in their work. The contour values in units of 10^{-27} sec^3 cm^{-3} are: (1) 123.0; (2) 11.3; (3) 6.56; (4) 3.74; (5) 2.12; (6) 1.2; (7) 0.641

luminosity, we find that the steady state temperatures fall well within the actual temperatures of the gas. This indicates that X-ray heating dominates the flow as the luminosity approaches its peak values.

Figure 8.7 is a P/F versus ρ/F plot. We again find two gas populations present. The extent of the problem mesh provides a larger range of ρ/F values than was found in the earlier models. We note that the gas is well behaved in its very hot and cool states, but that the two gas populations are again limited to the region between $\rho/F = 10^{-27}$ and $\rho/F = 10^{-25}$. Tracing this plot in time shows an interesting behavior. As the luminosity begins to rise after a minimum, the distinction between the two populations becomes blurred. However, as the luminosity approaches its peak, material begins to jump sharply upwards until the two gas populations are re-established. This creation of two populations within the gas is again the cause of the instability regions seen in Figs. 8.4-6 lying to the right of the secondary.

Finally, in Figs. 8.8 and 8.9, we display the velocity field and weighted momentum vectors near the secondary. Taking into account the fact that the luminosity has just passed a peak, we are not surprised to see the extended stagnation regions behind the secondary. The scale of these plots is essentially the same as that used for Models 1 and 2 (re. Figs. 5.7, 5.8, 6.8, and 6.9). While difficult to see on the velocity plots, the momentum plot (Fig. 8.9), shows a pronounced outward flow of material. This was not observed
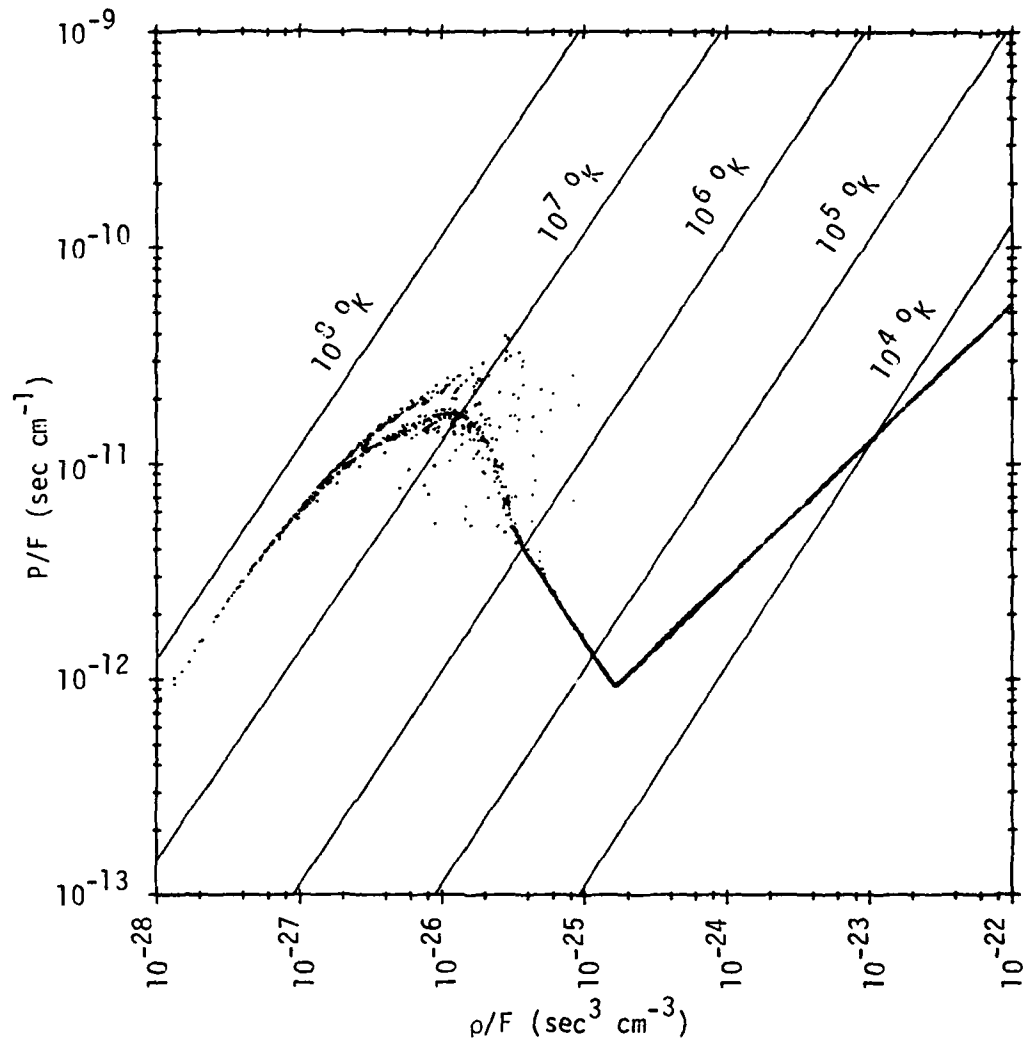
Figure 8.7. P/F vs ρ/F for Model 3. As with Models 1 and 2, the presence of two gas populations is evident by the separation of the curve near it's hump. The sharp corner in the lower right is an artifact of the fit to the steady temperature curve (Fig. 3.1).

114
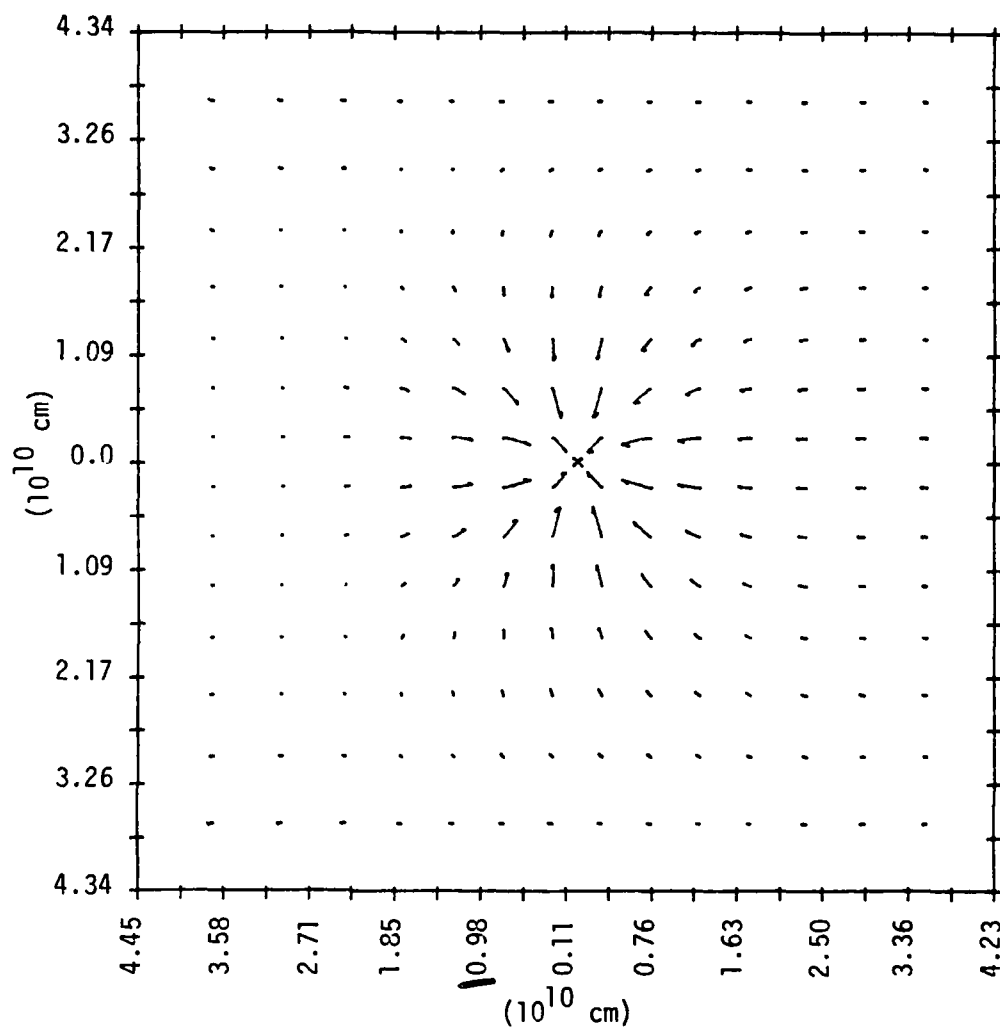
Figure 8.8. Velocity Field for Model 3. The vectors are drawn proportional to the maximum vector of 2.058×10^8 cm sec^{-1}. The velocities are those computed at the location of the tail of the vectors.
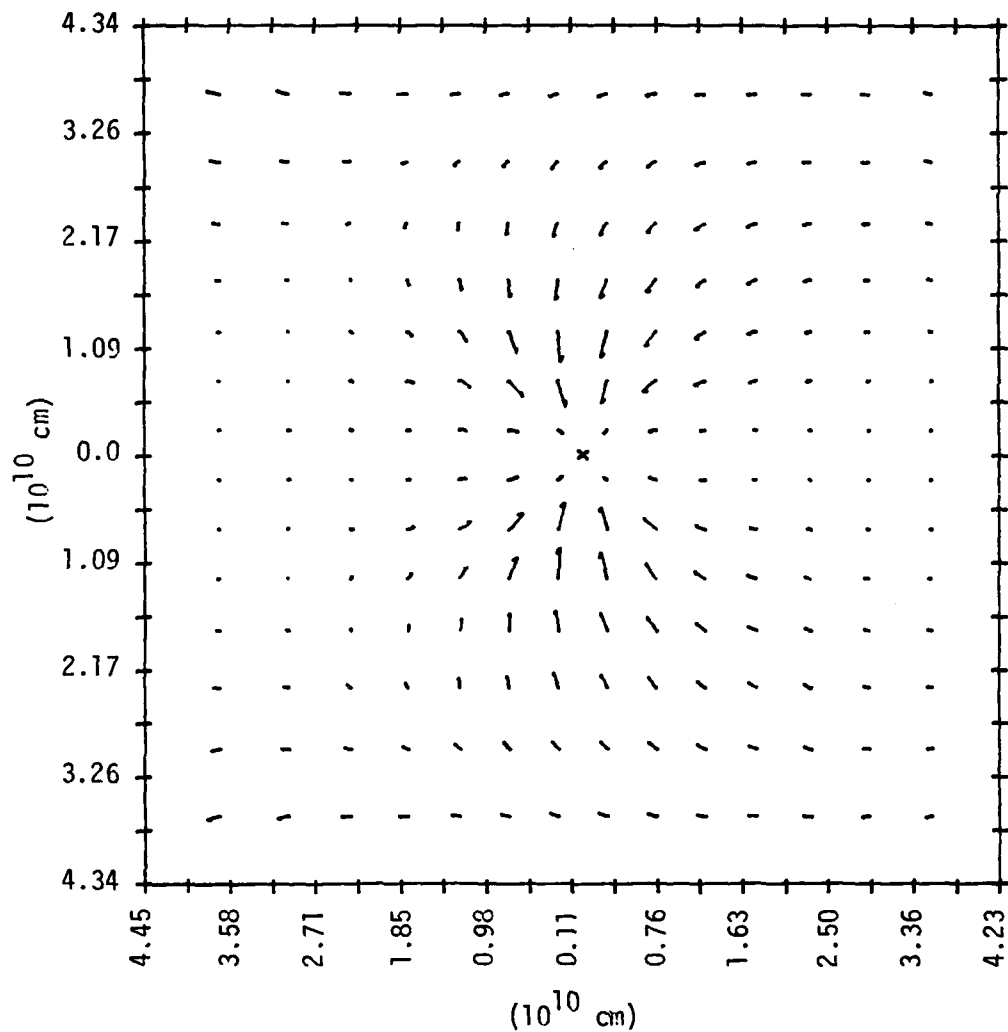
Figure 8.9. Weighted Momentum Vectors for Model 3. The momentum vectors indicate the momentum at the location of the tails multiplied by the distance off axis. This serves to emphasize the mass flux into the accretion region. Vectors of equal length signify equal mass flow. Note that most of the accreted material is captured from the sides in agreement with the line accretion model. The vectors are scaled to a maximum vector of 6.942×10^5 g cm^{-1} sec^{-1}.

in Models 1 and 2. The outward flow material to the left of the secondary could be responsible for the clumping of material off the line of centers to the left of the secondary as see in Fig. 8.3.

The most recent series of observations on the 4U1700-37 system were presented by Pietsch (1980), and Dolan (1980). Pietsch found that the 4U1700-37 system exhibits flares in its luminosity of magnitude on the order of 25, with time scales varying from minutes to hours. The *maximum luminosity* observed was 5.0×10^{36} erg sec^{-1}. We compare this to the flares exhibited by Model 3 which vary in luminosity by factors of 30 to 100, and on similar time scales. Although the peak luminosity after the start-up period is 5.0×10^{38} ergs sec^{-1}, this is related to the fact that the maximum luminosity was used to establish the model parameter set. In the discussion which follows in Chapter IX, we will address how Model 3 can be adjusted to bring it closer in line with observations.

IX. DISCUSSION

The purpose of this study was to combine recent results in three areas pertaining to X-ray binary star systems: first, hydrodynamic studies of mass exchange mechanisms; second, X-ray radiation transport through optically thin gases; and third, new models for radiation driven stellar winds in early type supergiant stars. In Chapter III, we presented methods for incorporating X-ray heating effects and the stellar wind force into the hydrodynamic equations.

Models 1 and 2 were presented in Chapters V and VI. Both models included X-ray heating and the stellar wind force. However, in neither model was ionization of the wind by the X-rays allowed to modify the strength of the wind force. From these models we have learned that X-ray heating and the wind force can cause reductions in the accretion rates and resulting luminosities as compared to predictions of previous numerical hydrodynamic models and Hoyle and Lyttleton's (1939) analytic line accretion model. The anticipated impact of significant X-ray pre-heating of the gas was specifically verified in Model 2.

In Chapter VII we developed a simplified model which demonstrated some of the characteristics of a stellar wind flowing under the influence of intense X-ray radiation. This led to Model 3 which was discussed in Chapter VIII. Model 3 represents a step beyond previous calculations in that the strength of the wind force was allowed to be modified by X-ray ionization. The work of Hatchett, Buff and McCray (1976) allowed us to estimate the

ionization state of the wind. They determined the ionization state of a gas of cosmic abundance as a function of the same variable, ξ, which we used for our heating parameter. This enabled us to estimate the point at which the wind force was shut off. The substantial effects on the flow led to periodic flaring of the X-ray luminosity. The shapes of the ionization regions were also strongly modified as a result of the varying wind densities. The peak luminosities resulting from Model 3 are artifically high. The model was formulated to be self-consistent using the peak luminosity. The unexpected strong variations in the wind density led to the large luminosity fluctuations.

A. Model Scaling Analysis

At this point we can consider how the results of Model 3 would scale with changes in system parameters under steady state conditions. We first note that the wind density is directly proportional to the mass loss rate from Eq. 4.7:

$$\rho = \frac{dM_0/dt}{4 \pi r^2 v} . \qquad (9.1)$$

Since the accretion rate is proportional to the wind density from Eq. 4.3:

$$dM_x/dt = \pi R_a^2 \rho_x v_x \alpha , \qquad (9.2)$$

the X-ray luminosity can be expected to be proportional to the mass loss rate. Additionally, the heating parameter, ξ, is directly proportional to the density, and inversely proportional to the X-ray luminosity from Eq. 3.10:

119

$$\xi = \rho \, r_x^2 / L_x \, . \tag{9.3}$$

Thus, ξ would remain constant at any given point as the mass loss rate was varied. Since ξ is constant, we expect no differences in the wind ionization structure as the mass loss varies. The steady state temperatures in the wind will also remain unchanged. However, since the X-ray luminosity enters into the calculation of the X-ray heating time, we need to examine the impact of a varying mass loss rate on the X-ray heating rate in more detail.

To estimate the changes in the X-ray heating rate, recall that the X-ray heating time was given by Eq. 3.20 as

$$t_x = \frac{t_c}{1 + (E_t/E)^2} \, , \tag{9.4}$$

where the Compton heating time is given by Eq. 3.19 as

$$t_c = \frac{4 \pi r^2 m_e C_v T}{L_x \kappa_e n} \, . \tag{9.5}$$

The rate of change in energy due to X-ray heating is given by Eq. 3.21 as

$$(\partial E/\partial t)_r = (E_{ss} - E)/t_x \, . \tag{9.6}$$

We see from Eqs. 9.4 and 9.5 that the X-ray heating time is inversely proportional to the X-ray luminosity, and, therefore also inversely proportional to the primary's mass loss rate. If the X-ray heating time increases, Eq. 9.6 indicates a corresponding decrease in the rate of change in energy. Apparently, decreasing the mass loss rate while maintaining self-consistency in the luminosity, will have the effect of decreasing the impact of X-ray heating.

The above analysis has been applied to steady state conditions. To extend this analysis to dynamic conditions such as found in Model 3, we begin by noting that if ξ remains constant at any point, the same flare producing process will be present. The wind force shut-down will occur at the same locations in the flow, leading to similar regions of material density enhancements. This leads us to conclude that flaring of Model 3 should continue to be present with the same general features as the primary's mass loss is decreased.

Being able to scale the luminosity with the primary's mass loss rate allows us to consider the effects of such a reduction on Model 3. If we reduce the mass loss rate by a factor of 100, the peak luminosities come into agreement with the observations of the base system, 4U1700-37. The duration of the flares, and the behavior in the wake, which are dominated by X-ray heating, can not be determined. A reduction by a factor of 100 in the primary's mass loss rate results in a rate that is a factor of 30 below the maximum mass loss rate available to the primary.

The lowering of the maximum luminosity also alleviates the problem of exceeding the Eddington luminosity, L_{edd}. After the initial start up period, Model 3 exceeds L_{edd} by factors of about 3 on three occasions for periods of 22 minutes. Since radiation pressure is not accounted for in our hydrodynamic equations, Model 3 can not properly limit accretion as L_{edd} is reached. However, the durations of the X-ray luminosity peaks are short enough that they may be observed even if radiation pressure is included. This will

depend on how smooth the flow is by the time it reaches the neutron star's surface. If the flow is greatly disrupted from spherically symmetric flow, brief outbursts exceeding L_{edd} may occur as was discussed by Vitello (1978).

B. Observational Comparisons with Model 3

The most recent observational work on 4U1700-37 was done by Pietsch et al. (1980) and is summarized in Table 2.1. They found slowly varying X-ray flaring time scales of about 0.5 to 1.0 hour. This flaring did not appear to be periodic in time. They also found that the X-ray spectrum could be fit by a 28 keV thermal bremsstrahlung spectrum in the 20-180 keV energy range.

Model 3 predicted periodic X-ray flaring on a time scale of about 3.5 hours. Since this period is about equal to the wind crossing time, it may be related to the way the wind force is disrupted. The high luminosity peaks are able to turn the wind force off very close to the primary's surface. This requires the regions of enhanced density to travel the full distance from the primary to the secondary. A more accurate model of the wind ionization structure would allow the wind force to turn off gradually. The density enhancements would then form closer to the secondary and have higher velocities than our model predicts. The regions would also tend to have longer density scale lengths, making the actual impact on the flaring behavior difficult to predict.

The observed spectrum is harder than the 22 keV exponential spectrum which was assumed for our steady-state temperature curve

(Fig. 3.1). This would cause the wind to be ionized farther from the secondary than in our model. Again the character of the density enhancements would be changed.

C. Weaknesses of Model 3

There are three major weaknesses in Model 3. The first is the restriction of the model to two dimensions, as was discussed in Chapter III. The second is the lack of any orbital motion. The symmetry invoked for the two dimensional models made it impractical to include such motion. This latter omission impacts most heavily on the dynamics of the wake, while the features found near the accretion region are not likely to be seriously affected. The ballistic model of Chapter VII addressed the three dimensional nature of the actual wind flow. It is apparent that a three dimensional model capable of handling the extended wind structure, along with the orbital motion, would be required for a complete modeling of the processes in X-ray binary systems.

The final weakness lies in our method of selecting a representative value of our heating parameter, ξ_{off}, at which the wind force is assumed to be shut off. As noted in Chapter VIII, ξ covers a large range of ionizations states, going from neutral to fully ionized as ξ varies by about 1000. Hence, the wind force is gradually weakened rather than being switched off suddenly. In particular, estimates made from the results of Hatchett and McCray (1977) indicate that L-shell ionization would begin at the surface of the primary and be complete near the secondary.

The effect of suddenly switching off the wind force is to create a sharp density variation in the wind which passes the secondary at a velocity lower than the normal wind velocity. Gradually weakening the wind force would produce a smoother density variation in the wind, but it would be moving at a higher velocity. These two processes can produce the same flaring characteristics. The flaring behavior is dependent on the maximum density reached in the enhanced density region and on the time it takes this region to pass the secondary. In other words, the flaring is the same if the density pulse seen by the secondary is the same.

D. Validity of the Optically Thin Assumption

It is now appropriate to discuss the validity of our assumption that the wind flows are optically thin. We can check this assumption by calculating the optical depth for Compton scattering along 3 paths through the models. We can then compute an adjustment factor to give the total opacity as a function of frequency relative to the Compton optical depth. The Compton optical depth gives an indication as to the validity of the optically thin assumption and the accuracy of the heating model in various regions of the problem mesh. The adjusted depth determines the degree to which the X-ray spectrum is modified from the assumed 22 keV exponential shape. This will allow a judgement to be made concerning the accuracy of the ionization structure predicted for the wind.

We estimate the Compton optical depth using the relation

$$\tau = \kappa_e \int \rho \, dx , \qquad (9.7)$$

where κ_e is the Thompson electron scattering opacity. For cosmic abundances, κ_e is 0.33 cm^2 g^{-1}. To estimate the frequency dependence of the opacity, we use the analytical fits given by Basko and Sunyaev (1973). These fits smooth over the absorption edges of the L and K shells, but are satisfactory for our purposes. Basko and Sunyaev found that for photon energies below 0.87 keV, the opacity was given by

$$\kappa(\nu) = 7.3 \times 10^{23} \, (\nu_0/\nu)^3 \, N_0 \, A^{-1} \, , \qquad (9.8)$$

where N_0 is Advogadro's number, A is the atomic weight of the material, and ν_0 is equal to 1 keV. For cosmic abundances, A is equal to 1.16198, so Eq. 9.7 can be expressed as

$$\kappa(\nu) = 114.65 \, (\nu_0/\nu)^3 \, \kappa_e \, . \qquad (9.9)$$

For photon energies above 0.87 keV, Basko and Sunyaev give

$$\kappa(\nu) = 2.5 \times 10^{-22} \, (\nu_0/\nu)^{2.4} \, N_0 \, A^{-1} \, , \qquad (9.10)$$

or,

$$\kappa(\nu) = 130 \, (\nu_0/\nu)^{2.4} \, \kappa_e \, . \qquad (9.11)$$

Equations 9.9 and 9.11 are plotted in Fig. 9.1.

The Compton optical depths are computed for each model along three different paths. Path 1 is from the secondary to the primary along the line-of-centers. Path 2 is from the secondary along a path perpendicular to the line-of-centers. Finally, path 3 is away from the primary along the line-of-centers, moving out through the wake region. The resulting optical depths are plotted in Figs. 9.2, 9.3, and 9.4 for Models 1, 2 and 3, respectively.

On examining Fig. 9.2, we see that Model 1 is very thin to
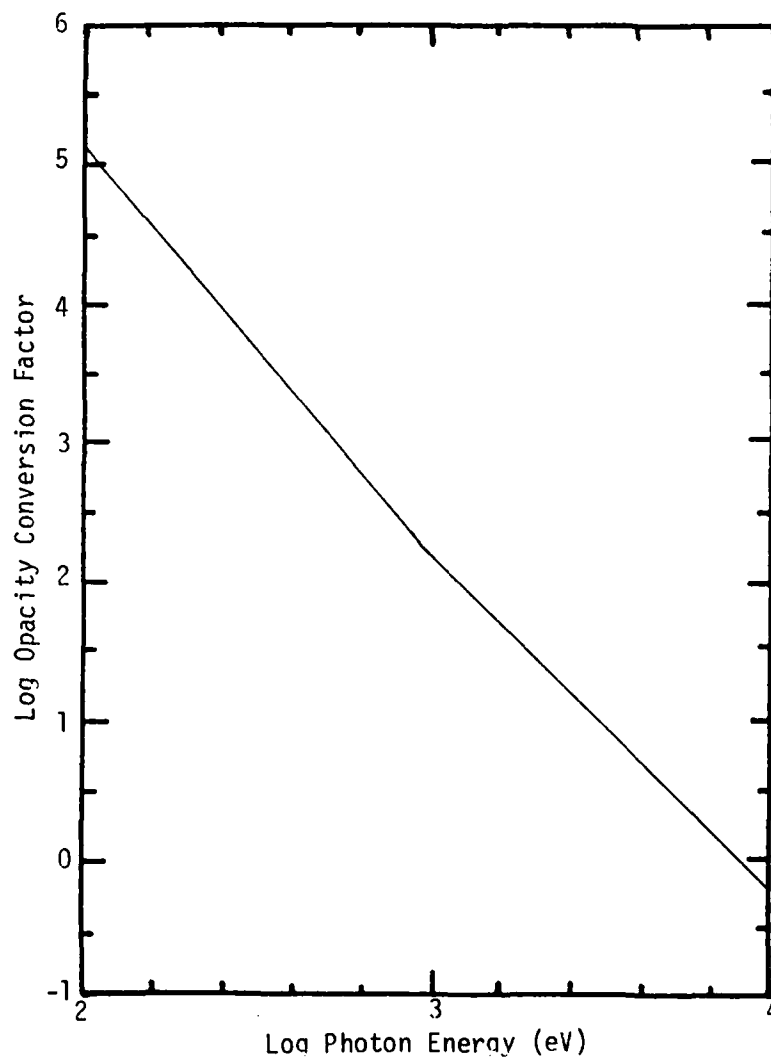
Figure 9.1. Optical Depth Factor vs. Photon Energy. This graph provides a means for estimating the frequency dependence of the optical depth. The Optical Depth Factor represents the increase in depth a photon of given energy experiences over the Compton Scattering Depth.

126

Figure 9.2. Compton Optical Depths for Model 1. Compton optical depths are plotted along three paths with the secondary as the starting point. Path 1 is along the line-of-centers towards the secondary. Path 2 is perpendicular to the line-of-centers. Path three is along the line-of-centers away from the primary. The arrow marks the distance at which the material temperature along each path drops below 0.1 keV.
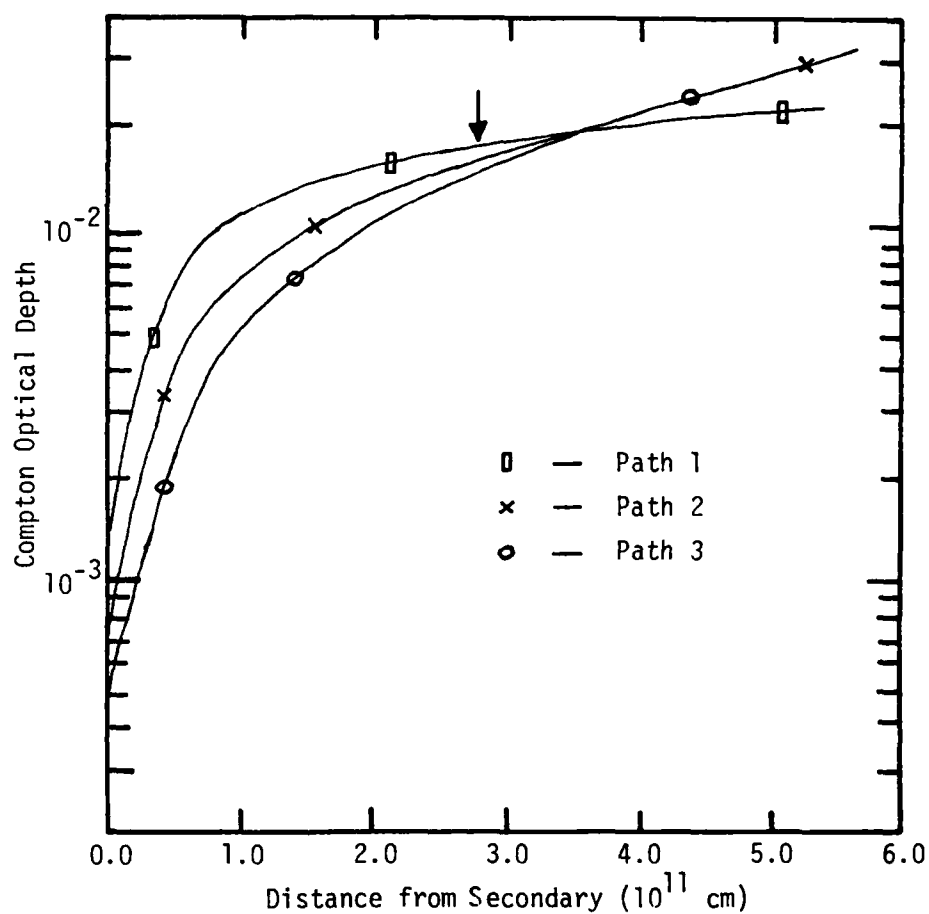
Figure 9.3. Compton Optical Depths for Model 2. Compton optical depths are plotted along three paths with the secondary as the starting point. Path 1 is along the line-of-centers towards the secondary. Path 2 is perpendicular to the line-of-centers. Path three is along the line-of-centers away from the primary. The arrows mark the points along the paths at which the material temperatures drops below 0.1 keV.
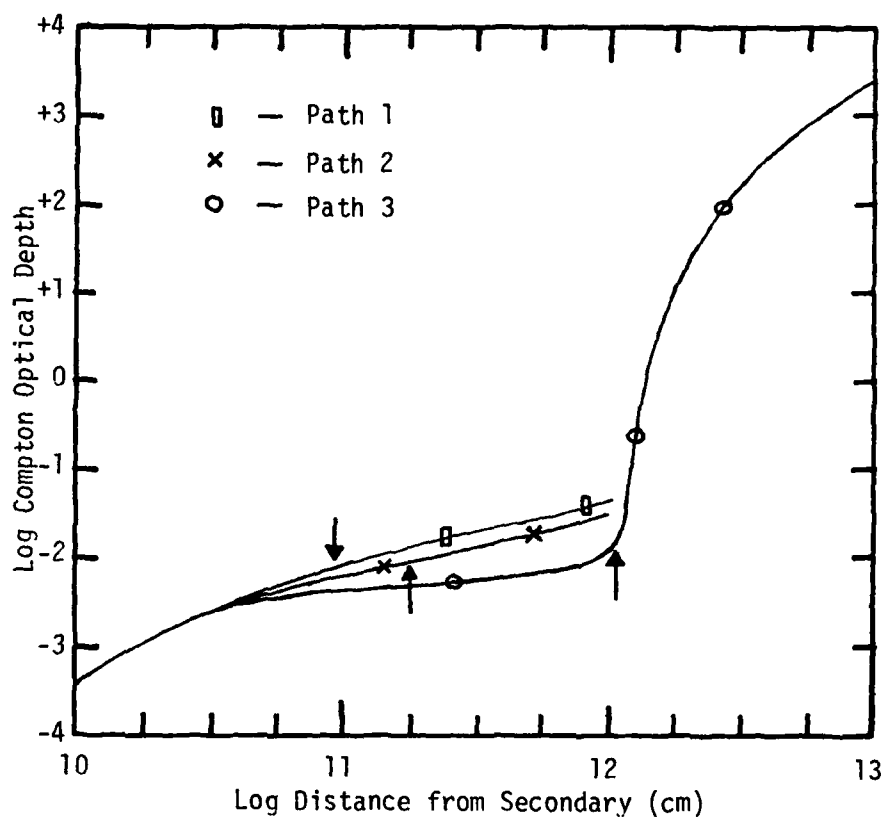
Figure 9.4. Compton Optical Depths for Model 3. Compton optical depths are plotted along three paths with the secondary as the starting point. Path 1 is along the line-of-centers towards the secondary. Path 2 is perpendicular to the line-of-centers. Path three is along the line-of-centers away from the primary. The arrow marks the point along each path at which the material temperature drops below 0.1 keV.
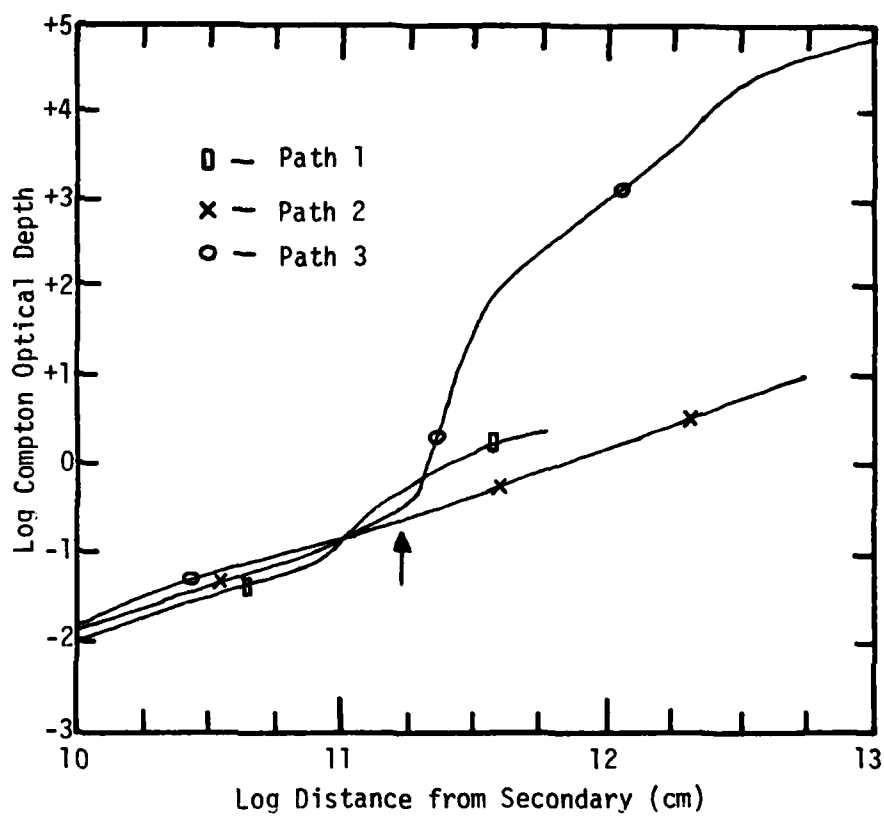
Compton scattering. The maximum depth is 0.033 Compton mean-free-paths. Referring back to Fig. 9.1, we see that the increase in optical depth by the factor of 100 needed to make the material optically thick is obtained for photons with energies of 1 keV or less. Thus our optically thin assumption holds reasonably well in all regions of Model 1.

The Model 2 results are shown in Fig. 9.3. We find that the model becomes optically thick along the paths 1 and 2 for distances greater than about 10^{11} cm. There is a drastic change in the optical depth of the wake, as indicated by the sudden jump occurring at 10^{12} cm along path 3. This corresponds to the very tip of the hot central wake. Beyond this point the cool, dense material has finally collapsed onto the axis, causing the very rapid increase in optical depth from that point outward. This behavior is limited to the dense material on the axis. Material outside the wake has densities similar to that found along the path 2.

The far wake is optically thick not only to Compton scattering, but also to photons with energy well above 10 keV. The material along path 3 shows a Compton depth of 0.32 mean-free-paths. From Fig. 9.1, we see that this material becomes optically thick to photons with energies of 4.5 keV or less. Since the densities in Model 2 are not that different from those of Model 1, Model 1 would have the same cut-off. Model 1 therefore predicts a spectral cut-off very similiar to the 2.2-4.4 keV cut-off actually observed in the Vela X-1 system (re. Table 2.1).

To judge the impact on the heating model caused by the high optical depths, we have indicated on Fig. 9.3 the distances along each path at which the temperatures drop below 0.1 keV. At the distances marked, the steady state temperatures are very low, so that very little X-ray heating occurs. Thus, X-ray heating does not significantly effect the flow beyond the region of the model where the optically thin assumption holds.

Finally, Fig. 9.4 shows the behavior of the optical depths in Model 3. The behavior is nearly identical to that seen in Model 2, except that the higher densities encountered in Model 3 have shifted the features upward by an order of magnitude. We again see a sharp jump in the optical depth along the wake (path 3), while the other two paths show a smooth increase. We have also marked with an arrow the distance at which the temperatures along the three paths drop below 0.1 keV. At this point, the flow has become optically thick to photons of about 3 keV. Thus, our optically thin assumption breaks down much more rapidly for Model 3 than for the first two models. The region of strong X-ray heating near the secondary is still reasonably optically thin. However, beyond a distance of 2×10^{11} cm the flow is decidedly optically thick. This implies that the ionization structures given by Model 3 are not entirely accurate in this region. In particular, the wind shut-down region is found to move into and out of the optically thin region as the X-ray luminosity varies.

Utilizing Fig. 9.1, we find a spectral cut-off of about 7.5 keV

for regions lying outside of the wake. A 2.2-5.5 keV cut-off was noted in Table 2.1 for the 4U1700-37 system. This is another indication that the densities in Model 3 are higher than the densities of the base system. This is not suprising, since the primary's mass loss rate was artificially high to enforce self-consistency at the maximum observed luminosity. Hence the artificially high wind densities are expected.

Some care must be exercised in comparing the optical depths of these models with the real systems. In the actual systems, the wind flow is spherically symmetric with respect to the primary. Our models used planar flows which do not exhibit radial divergence. Thus, the wind density in our models remains constant along paths perpendicular to the line of centers. Spherical flow would yield continually decreasing densities along similar paths. This causes our models to predict optical depths higher than those expected in the actual star systems.

While all three models show a tendency to become optically thick far from the secondary, we note that the temperature of the material, where it becomes optically thick, is on the order of a few eV. Thus, the regions near the secondary where the flow is most strongly heated by the X-rays are still optically thin, so that our X-ray heating model holds rather well. However, the description of the ionization structure of the gas beyond this region becomes progressively more inaccurate with increasing optical depth. This is due to absorption of the lower energy photons which changes the characteristics of the

X-ray spectrum until it no longer accurately matches the assumed 22 keV exponential spectrum. The ionization and heating effects become progressively more inaccurate as the material becomes optically thick.

This presents a problem when dealing with the wind force shut-down of Model 3. The modified spectrum will not ionize the oxygen L-shells under the same conditions assumed for our model. The 50% ionization state will occur closer to the secondary than in our model. There is a compensating factor which must also be taken into account. Hatchett, Buff and McCray (1976) computed the ion populations for oxygen in an optically thick gas. As noted previously, the oxygen goes from neutral to fully ionized over a much smaller range of ξ than in the optically thin case. This would cause the wind force to turn off faster and more closely approximate the sudden turn off of our Model 3.

Reconsidering the question of scaling, recall that ξ will remain constant as the mass loss rate and the X-ray luminosity are dropped. Decreasing the density will also have the effect of decreasing the optical depths in the model. This would place us firmly in the realm of our optically thin assumption. We conclude that Model 3 does a *fair job of representing the physical processes which occur in the* real system, but the details of these processes are limited by the assumptions necessary to produce the model.

E. Comparisons with Previous Works

As discussed in Chapter I, Livio, Shara, and Shaviv (1979)

(hereafter refered to a LSS) presented a model of Cen X-3 (4U1118-60) which attempted to handle the hydrodynamics and X-ray heating in a manner similar to ours. The differences between the two models involves the method in which the X-ray heating is accounted for. LSS assumed a constant wind velocity with $v = v_{\infty}$ everywhere, with no provision being made for a force driving the wind. Most importantly, they kept the X-ray luminosity fixed instead of basing it on the accretion rate.

LSS cast their X-ray heating term in the form $A(T-T_{eq})$, where A is a numerically adjusted parameter serving the same function as our t_x^{-1}, and the $T-T_{eq}$ is equivalent to our $E-E_{ss}$ (re. Eq. 9.6). The parameter A was adjusted numerically until thermal balance is reached in the gas and is then allowed to remain fixed. It seems that their *method of fixing the parameter A*, and not basing the X-ray luminosity on the accretion rate, would produce an artificially smooth problem with no means of supporting the thermal instabilities which we observed. For their heating method to work, they had to assume that the flow would go to a steady state. Their model could be compared with our Model 1 since their model parameters put it in a state in which little effect on the accretion rate due to X-ray heating would be expected. They in fact predicted no instabilities in the wind flows.

The velocity plot presented by LSS shows a large region around the primary. It seems to indicate that the wind has almost no velocity in the region perpendicular to the line-of-centers near the

secondary. The velocity of the wind should not be affected far from the secondary if radiation effects on the wind force are not considered. In fact, the velocity at the side boundaries should be the unperturbed velocity of the wind at the secondary's orbit. It appears that their boundary conditions are not properly supporting the wind velocities.

Ignoring the wind velocity structure also adversely impacts on the qualitive features of their results. The density contours produced by LSS do not show the pronounced wake which we found. Their temperature contours should be nearly spherical in front of the shock, but in fact are very irregular. This may be related as much to their method of X-ray heating as to their wind structure.

Another difference between the two models is the treatment used at the boundary of the secondary. We accreted material through the boundary while LSS replaced the secondary with a solid boundary. This caused the flow to build up to hydrostatic equilibrium about the secondary. LSS argued that this approximates the case where the mass flow through the magnetosphere of the secondary is slow enough so as not to perturb the flow in the immediate vicinity. It is not clear how this slow mass flux onto the secondary produces the observed luminosity and still does not perturb the incoming flow. To support the luminosity, the material must flow to the surface of the neutron star at essentially the same rate that it is accreted.

We can also compare our results to those found by Hoffman (1979). Hoffman's isothermal model developed variations in the mass

135

accretion rate. These variations were a result of modulating the mass flow down the accretion column in the wake of the secondary. Our Models 1 and 2 did not develop such flow. In fact, noticable accretion columns did not form in these models. Instead, we found the bulk of the accretion flow to enter from the sides of the wake. Hoffmah's models did not include the stellar wind driving force. This additional force appears to be the reason for the decrease in the accretion flow directly behind the secondary as discussed in Chapter V. His models also did not show the formation of a hot central region in the core of the wake.

Carlberg (1978) did an analytical study of accretion based on the line accretion model which included arguments concerning the effects of X-ray heating. On a graph of the wind velocity versus wind density, he showed regions where X-ray heating would and would not affect the accretion flow (re. his Fig. 3.). Since he assumed a constant wind velocity, we can assume the velocity and the density to be the wind velocity and density at the orbit of the secondary. On plotting the three points corresponding to our models, we found that all three models lay very close to the boundary between the two regions. Model 1 lay just marginally below the boundary in the region of low X-ray impact. Models 2 and 3 lay just above the boundary, predicting significant X-ray impact on the flows. Comparison of Model 3 is difficult in light of the variations set up in the wind. However, Models 1 and 2 appear to agree with his predictions. The drastic change in accretion rates between Models 1

and 2 does not appear to be justified by their very slight difference in position relative to the boundary. This may again be the result of adding the wind force term to the model.

F. Summary

This study of X-ray heating in models of accretion from a stellar wind in massive X-ray binary stars has led to several conclusions. From Models 1 and 2 we learned that the analytic line accretion model of Hoyle and Lyttleton (1939) comes within a factor of 10 of describing the accretion rates in these systems. The degree to which the line accretion model agrees with the X-ray heated models was shown to be dependent on the X-ray heating rates in the gas. If the X-ray heating is sufficient to dominate the hydrodynamics of the flow, then the accretion rate will be significantly lower than that predicted by the analytic model.

Our ballistic analysis in Chapter VII suggested that the wind accretion model could function even under extreme impairment of the wind force due to X-ray ionization. The wind is severely disrupted from the normal spherical outflow. A large range of material velocities was found. The wind flows normally outward within the X-ray shadow region. Once exposed to the X-rays, the wind will free-fall under the influence of the primary's gravity. Lower velocity regions will begin to flow back in towards the primary. The analysis suggests that sufficient material will be present in the secondary's vicinity and at low enough velocity to allow for efficient accretion, thus easily supporting the observed luminosity.

Material flowing inward, however, severely distorts the spherically symmetric outflow assumed by the radiation driven wind model. The impact on the wind model is not known at this time.

In Model 3 we found that a striking feedback mechanism was created in a flow whose wind force could be modified by the X-ray radiation. We found that as the wind was turned on and off, variations in density were created which caused fluctuations in the X-ray luminosity. The fluctuating luminosity led to variations in the wind density. The characteristics of the resultant X-ray flaring were very similiar to the slow X-ray flares observed in 4U1700-37.

These results pave the way for future work in this area. A method is needed to simulate three dimensional effects efficiently and accurately. A more detailed radiation treatment is also necessary. This would permit a more accurate determination of the X-ray impact on the wind, and would make it possible to more accurately predict light curves for the binary systems. Such light-curves would provide a closer observational check of the models.

X. LIST OF REFERENCES

Alme, M. L. 1974, "Numerical Studies of Mass Transfer and Accretion in X-ray Binary Systems" (Ph.D. thesis), Lawrence Livermore Laboratory (UCRL-51664), (National Technical Information Service TID-4500, UC-346)

Alme, M. L., and Wilson, 1973, Ap. J., 186, 1015.

———. 1974, Ap. J., 194, 147.

———. 1975, Ann. N.Y. Aca. Sci., 262, 379.

———. 1976, Ap. J., 210, 233.

Amnuel, P. R., Guseinov, O. H., and Rakhamimov, Sh. Yu. 1979, Ap. J. Suppl., 41, 327.

Avni, Y. and Bahcall, J. 1975, Ap. J. (Letters), 202, L131.

Bahcall, J. 1978, Ann. Rev. Astr. Ap., 16, 241. Basko, M. M., and Sunyaev, R. A. 1973, Ap. and Space Sci., 23, 117.

Becker, R. H., Rothschild, R. E., Boldt, E. A., Holt, S. S., Pravdo, S. H., Serlemitsos, P. J., and Swank, J. H. 1978, Ap. J., 221, 912.

Blumenthal, G. R., Tucker, W. H. 1974, Ann. Rev. Astr. Ap., 12, 23.

Bondi, H. 1952, MNRAS, 112, 195.

Bondi, H. and Hoyle, F. 1944, MNRAS, 104, 273.

Buff, J. and McCray, R. 1974a, Ap. J., 189, 147.

Cassinelli, J. P. 1979, Ann. Rev. Astr. Ap., 17, 275.

Castor, J., Abbott, D., and Klein, R. 1975, Ap. J., 195, 157.

Carlberg, R. G. 1978, Ap. J., 220, 1041.

Clayton, D. C. 1968, "Principles of Stellar Evolution and
Nucleosynthesis", (New York: McGraw-Hill)

Conti, P. S. 1978a, Ann. Rev. Astr. Ap., 16, 371.

———. 1978b, Astr. Ap., 63, 225.

Conti, P. S. and Cowley, A. P. 1975, Ap. J., 200, 133.

Conti, P. S. and Germany, C. D. 1980, Ap. J., 238, 190.

Cowie, L. L., Ostriker, J. P., and Stark, Anthony A. 1978, Ap. J.,
226, 1041.

Davidson, K. and Ostriker, J. P. 1973, Ap. J., 179, 585.

Dolan, J. F., Coe, M. J., Crannell, C. J., Dennis, B. R., Frost, K.
J., Maurer, G. S., Orwig, L. E. 1980, Ap. J., 238, 238.

Eddington, A. 1926, "The Internal Constitution of Stars", (reprinted
1959, New York: Dover)

Field, G. 1965, Ap. J., 142, 531.

Forman, W., Jones, C., Cominsky, L., Julien, P., Murray, S., Peters,
G., Tanabaum, H., and Giacconi, R. 1978, Ap. J. Suppl.,
38, 357.

Giacconi, R. 1976, Am. J. Phys., 44, 121.

Greenstein, G. and McClintock, J. E. 1976, Ap. J. (Letters), 208,
L41.

Gursky, H. 1976, in "Frontiers of Astrophysics", ed. E. H. Avrett,
(Cambridge: Harvard University Press)

Hatchett, S., Buff, J., and McCray, R. 1976, Ap. J., 206, 847.

Hatchett, S. and McCray, R. 1977, Ap. J., 211, 552.

Hoffman, N. M. 1979, private communication.

Holzer, T. E., and Axford, W. I. 1970, Ann. Rev. Astr. Ap., 8, 31.

Hoyle, F. and Lyttleton, R. A. 1939, Proc. Camb. Phil. Soc., 85, 405.

Hunt, R. 1971, MNRAS, 154, 141.

————. 1979, MNRAS, 188, 83.

Hutchings, J. 1974, Ap. J., 192, 685.

————. 1976, Ap. J., 203, 438.

————. 1980, Ap. J., 235, 413.

Kopal, Z. 1959, "Close Binary Systems", (New York: Wiley)

Lamb, F. K., Fabian, A. C., Pringle, J. E., and Lamb, D. Q. 1977, Ap. J., 217, 197.

Lamb, F. K., Pethick, C. J., and Pines, D. 1973, Ap. J., 184, p271.

Livio, M., Shara, M., and Shaviv, G. 1979, Ap. J., 233, 704.

Lucy, L. B. and Solomon, P. M. 1970, Ap. J., 159, 879.

McClintock, J., Rappaport, S., Joss, P., Bradt, H., Buff, J., Clark, G., Hearn, D., Lewin, W., Matilsky, T., Mayer, W., Primini, F. 1976, Ap. J. (Letters), 206, L99.

McCray, R. 1974, "Gas Flows in Binary X-ray Systems", International Conference on X-rays In Space.

McCray, R. and Hatchett, S. 1975, Ap. J., 199, 196.

Mestel, L. 1954, MNRAS, 114, 437.

Morton, D. C. 1967a, Ap. J., 147, 1017.

————. 1967b, Ap. J., 150, 535.

————. 1976, Ap. J., 203, 386.

Paczynski, B. 1971, Ann. Rev. Astr. Ap., 9, 183.

Parker, E. N. 1972, Ap. J., 174, 499.

Petterson, J. 1978, Ap. J., 224, 625.

Pietsch, W., Voges, W., Reppin, C., Trumper, J., Kendzierra, E.,
Staubert, R., 1980, Ap. J., 237, 964.

Potter, D. 1973, "Computational Physics", (New York: Wiley)

Pravdo, S., Becker, R., Boldt, E., Holt, S., Rothschild, R.,
Serlemitsos, P., and Swank, J. 1976, Ap. J. (Letters), 208, L67.

Prendergast, K. H. and Spiegel, E. A. 1973, Comments Ap. Space Phys.,
5, 43.

Rappaport, S., Joss, P., McClintock, J. 1976, Ap. J. (Letters), 206,
L103.

Richtmyer, R. and Morton, K. 1967, "Difference Methods for
Initial-Value Problems", (New York: Wiley - Interscience)

Savonije, G. J. 1979, Astr Ap., 71, 352.

Shakura, N. I. and Sunyaev, R. A. 1973, Astr. and Ap., 24, 337.

Shvartsman, V. F. 1971, Soviet Astr.-AJ, 14, 527.

Tarter, C.B, Tucker, W.H., and Salpeter, E.E. 1969, Ap. J., 156, 943.

Thomas, Hans-Christoph 1977, Ann. Rev. Astr. Ap., 15, 127.

Ulmer, M. P., Baity, W. A., Wheaton, W. A., Peterson, L. R. 1972, Ap.
J. (Letters), 178, L121.

van den Heuvel, E. P. J. 1975, Ap. J. (Letters), 198, L109.

Vitello, P. A. J. 1978, Ap. J., 225, 694.

Weymann, R. 1963, Ann. Rev. Astr. Ap., 1, 97.

Zel'dovich, Ya B., and Shakura, N. I. 1969, Soviet Astr.-AJ, 13, 175.

DA
FILM